Waveguide platform and methods for super-resolution fluorescence microscopy of sub-cellular structures

Thèse N° 9630

Présentée le 25 juin 2019
à la Faculté des sciences de base
Laboratoire de biophysique expérimentale
Programme doctoral en photonique

pour l'obtention du grade de Docteur ès Sciences

par

Anna ARCHETTI

Acceptée sur proposition du jury

Prof. C. S. Brès, présidente du jury
Prof. S. Manley, directrice de thèse
Prof. A. Diaspro, rapporteur
Prof. T. Huser, rapporteur
Prof. C. Galland, rapporteur

2019

ÉCOLE POLYTECHNIQUE
FÉDÉRALE DE LAUSANNE

Abstract

Super-resolution fluorescence microscopy is widespread, owing to its demonstrated ability to resolve dynamical processes within cells and to identify the structure and position of specific proteins in the interior of protein complexes. Nowadays, subcellular features can be routinely resolved at the nanoscopic scale thanks to the accessibility of straightforward sample-preparation protocols, simple hardware tools, and open source software. Building on its ability to investigate large-scale macromolecules networks in their natural environment with high resolution, fluorescence microscopy is further evolving by the development of quantitative and high-throughput methods to characterize such networks. Previous implementations of high-throughput microscopy made use of imaging sequentially smaller fields of view (FOV), which makes axial alignment a challenge and extends the imaging time. In our work, we circumvent these problems with our large FOV systems, which are based on flat-field sample illumination over large areas, combined with a CMOS-camera.

In this thesis, I present a waveguide platform designed to image a wide area with low background by mean of total internal reflection fluorescence (TIRF) excitation. The waveguide chips for this platform were fabricated at the center of micro-nano technology (CMi) at EPFL, in collaboration with the group of Aleksandra Radenovic (specifically with Evgenii Glushkov). The resulting waveguide-TIRF system is specifically optimized for applications where easy and repetitive buffer exchange is needed.

To achieve large and uniform TIRF excitation, I studied some fundamental parameters of the waveguide, developing specific code to simulate, at the first order, its behavior. I then extended light propagation solutions adopted in the field of integrated photonics to our waveguide chip fabrication process. To easily integrate the chip within the commercial stage of an upright microscope, I designed a novel chip holder that ensures aqueous solution sealing, mitigates the presence of scatter light in the imaging area, and facilitates the waveguide alignment during the input beam-coupling phase.

On the analysis side, the need for computational tools that are specific to fluorescence microscopy is continuously growing, due to the fact that this technique heavily relies on the treatment of large quantities of data. The automated analysis of images is a fundamental step of the measurement process, necessary for unbiased quantification and statistical validation, especially where repetitive visual inspection would be impractically long. This is particularly critical for single molecule localization microscopy (SMLM), where the quality of the reconstructed super-resolved image actually is a trade-off between the algorithm localization precision and its speed, a key element considering the need of processing tens of thousands of large images to generate the final, super-resolved one.

In this work, I present a series of computational tools for CMOS camera characterization developed for large flat-field STORM microscopy, a 3D SMLM reconstruction software specific for Double-Helix (DH) point spread function (PSF) and a set of cell shape analysis tools to study *C.Crescentus* shape dynamics.

KEYWORDS:

super-resolution fluoresce microscopy, TIRF, waveguide micro-nano fabrication, 3D single molecule analysis, bacteria cell shape, image processing

Sommario

La microscopia in fluorescenza a super-risoluzione si è largamente diffusa grazie alla sua dimostrata abilità nel riuscire a risolvere processi dinamici nelle cellule e a discernere la struttura e posizione di specifiche proteine all'interno di complessi proteici.

Tale tecnica si è affermata grazie ad uno sforzo interdisciplinare che ha portato, da un lato, allo sviluppo e validazione di protocolli efficaci per la preparazione dei campioni biologici e, dall'altro, allo sviluppo e diffusione di strumenti ottici innovativi e software open-source. Oggigiorno la microscopia in fluorescenza si sta ulteriormente sviluppando, con l'obbiettivo di permettere uno studio di campioni biologici sempre più estesi con alta risoluzione e alta efficienza.

Lo studio e l'analisi di grandi numeri di sub-campioni viene solitamente eseguito prendendo immagini consecutive di porzioni adiacenti dell'intero campione. Questo approccio, però, richiede un non banale riallineamento assiale per ogni movimento sul piano del capione, ed implica un allungamento del tempo di imaging. I due sistemi che abbiamo sviluppato nel nostro laboratorio permettono invece di analizzare contemporaneamente più sub-campioni, grazie all'estensione dell'illuminazione ad un'area più ampia, senza perdere i requisiti di unifomità e irradianza. La cattura di immagini più estese è stata possibile anche grazie all'utilizzo camere CMOS commercialmente disponibili con un più alto numero di pixels, a parità di frame rate, rispetto alle camere EMCCD precedentemente adottate in questo campo.

In questo lavoro, presento una piattaforma per microscopia in fluorescenza basata su guide-d'onda che permettono di illuminare il campione con un campo evanescente uniforme. La fabbricazione delle guide-d'onda è stata realizzara presso il centro di micro-nano fabbricazione (CMi) dell'EPFL in collaborazione con il gruppo di Aleksandra Radenovic (in particolare con Evgenii Glushkov).

Il campo generato dalla luce rifratta all'interfaccia tra la guida-d'onda e il campione genera una sezionamento (TIRF) ottico del campione che è ragionevolmente uniforme lungo tutta la superficie della guida-d'onda a contatto con il campione. Tale piattaforma è stata ottimizzata per permettere uno scambio veloce di soluzioni acquose. Per ottenere un campo evanescente uniforme e largo ho studiato alcuni parametri fondamentali della guide-d'onda, sviluppando il necessario codice per simularne il comportamento in prima

approssimazione. Inoltre ho esteso soluzioni tipicamente adottate nell’ambito della fotonica al processo di fabbricazione delle nostre guide-d’onda. Per integrare le guide-d’onda nel microscopio, ho inoltre progettato un supporto meccanico che potesse non solo allineare facilmente le guide-d’onda con il fascio laser, ma che potesse anche trattenere la soluzione aquosa e schermare la scattering generato nell’area di accoppiamento tra la guida-d’onda ed il laser.

Lo sviluppo di strumenti computazionali specifici per microscopia in fluorescenza é un bisogno in continua crescita, in quanto tale tecnica si basa sul trattamento di grandi quantità di dati, richiedendo una sempre più elevata capacità di analisi.

L’analsisi automatizzata di immagini è infatti fondamentale per una estrapolazione quantitativa e imparziale dei dati, attraverso un campionamento multiplo statisticamente rilevante che richiederebbe tempi irragionevolmente lunghi se effettuato per ispezione visuale diretta. Inoltre, nel campo della microscopia basata sulla localizzazione di singole molecole (SMLM), i software sono fondamentali per poter ricostruire un’immagine super-risolta a partire da decine di migliaia di immagini di milioni di pixels ciascuna, e possono influenzare notevolmente la qualità dell’immagine finale.

In questo lavoro, presento quindi una serie di metodi computazionali sviluppati a partire da una serie di funzioni MATLAB che ho scritto per caratterizzare una CMOS camera accoppiata ad un microscopio STORM basato su un sistema di illuminazione uniforme a vasto campo. Ho inoltre sviluppato una completa pipeline per processare i dati di singole molecole (SM) e ricostruirne un’immagine super-risolta in tre dimensioni. L’informazione assiale sulla posizione della molecola è codificata nella forma della sua point spread function (PSF): infatti la point spread function (PSF) delle molecole è caratterizzata da due lobi che disegnano una doppia elica (double helix - DH) muovendo le molecole nella direzione assiale. Infine, presento una serie di funzioni volte ad analizzare la dinamica della forma cellulare del *C.Crescentus*.

Index

ABSTRACT **3**
SOMMARIO **5**
INDEX .... **I**
LIST OF TABLES AND FIGURES .... **III**
PART I INTRODUCTION TO SUPERRESOLUTION FLUORESCENCE MICROSCOPY .... **1—1**

1 SUPER-RESOLUTION PRINCIPLES, METHODS AND LIMITATIONS .... 1—3
1.1 Single Molecule Localization Microscopy (SMLM) .... *1—5*
1.1.1 SMLM with photo-switching fluorophores .... 1—5
1.1.2 3D SMLM approaches .... 1—8
1.1.3 DNA Points Accumulation for Imaging in Nanoscale Topography (DNA-PAINT) .... 1—10
1.2 Structured illumination microscopy (SIM) .... *1—13*
2 IMAGE QUALITY LIMITATIONS IN SMLM .... 2—1
2.1 Illumination aspects critical for image quality .... *2—1*
2.1.1 Global field flattening with Köhler integrator or beam shaping elements .... 2—2
2.1.2 Local speckles and interference fringes homogenization .... 2—3
2.2 Optical sectioning techniques .... *2—6*
2.2.1 TIRF illumination .... 2—7
2.2.2 Light sheet illumination .... 2—9
2.3 Single molecule localization precision .... *2—14*
2.3.1 3D SMLM DH-PSF localization algorithms .... 2—18

PART II APPLICATIONS AND AIMS OF THIS WORK .... **2—23**

3 RESOLVING BACTERIAL CELL SHAPE DYNAMICS .... 3—25
3.1 Principles of C. crescentus constriction rate modulation in cell shape dynamics .... *3—25*
3.1.1 Cell size regulation .... 3—28
3.2 Aims of this work: cell shape parameters analysis .... *3—29*
3.2.1 Development of an automated image processing method and cell dynamic simulator .... 3—30
3.2.2 Development of 3D Double-Helix PSF software .... 3—32
4 HIGH-THROUGHPUT NANOSCOPY OF SUBCELLULAR STRUCTURE: LARGE FLAT FIELD STORM AND PAINT .... 4—35
4.1 Aim of this work: CMOS camera characterization for MLE sCMOS-specific algorithm .... *4—35*
4.2 Aim of this work: development of a waveguide-based platform for DNA-PAINT .... *4—39*

PART III METHODS DEVELOPMENT AND RESULTS .... **4—41**

5 RESOLVING BACTERIAL CELL SHAPE DYNAMICS .... 5—43
5.1 Bacteria cell image processing: sDaDa .... *5—44*
5.2 Bacteria pole shape dynamics simulator .... *5—46*
5.3 3D DH-PSF image reconstruction: StormChaser .... *5—49*
6 LARGE FLAT FIELD STORM .... 6—57
6.1 CMOS camera noise and characterization .... *6—58*
6.2 Maximum Likelihood Localization Estimation (MLE) .... *6—61*
7 LARGE FLAT FIELD WAVEGUIDE-PAINT .... 7—65
7.1 Waveguide Chip design .... *7—65*
7.2 Chip holder and Microscope design .... *7—71*
7.3 Waveguide DNA-PAINT imaging of cells and DNA origami .... *7—73*
7.3.1 Sample preparation .... 7—73
7.3.2 Imaging and data analysis .... 7—79

PART VI DISCUSSION AND CONCLUSIONS .... **7—81**

88—83
8.1 Cell shape image analysis automation .... 8—83
8.2 Flat-field illumination platform: prospective .... 8—84
8.3 Waveguide-TIRF: prospective .... 8—85

APPENDIX .... 8—87

A. WAVEGUIDE PARAMETERS STUDY .... 8—89
B. CHIP HOLDER CAD DESIGN .... 8—90
C. CHIP FABRICATION .... 8—91

BIBLIOGRAPHY II
CURRICULUM VITAE XIV

Personal information xiv
Work Experience xiv
Education xv
Skills xv
Interests xvi
Publications xvi
Prizes, selections and oral presentations xvi

List of tables and figures

Tables

TABLE 1-1 SUPER-RESOLUTION LIGHT MICROSCOPY METHODS. 1—4
TABLE 2-1 LIGHT-SHEET MICROSCOPY METHODS COMPATIBLE WITH SMLM. 2—13
TABLE 5-1 3D DH-PSF SOFTWARE COMPARISON AT THE SMLM CHALLENGE 2016. 5—53
TABLE 6-1 SCMOS ZYLA 4.3 ANDOR CHARACTERIZATION. 6—60
TABLE 7-1 WAVEGUIDE-PAINT EXPERIMENTAL CONDITIONS AND RESULTS. 7—79
TABLE D-1 WAVEGUIDE FABRICATION PROCESS FLOW. 8—91

Figures

FIGURE 1-1 – VISUALIZATION OF THE IMAGING PROCESS. 1—3
FIGURE 1-2 – SINGLE MOLECULE LOCALIZATION MICROSCOPY CONCEPT. 1—6
FIGURE 1-3 – 3D SMLM APPROACHES. 1—8
FIGURE 1-4 – 3D-PSF SIMULATED DATASET 1—9
FIGURE 1-5 – DNA-PAINT SAMPLE SCHEME. 1—10
FIGURE 1-6 – DNA-ORIGAMI CREATION PRINCIPLE. 1—11
FIGURE 1-7 – DNA-PAINT EXPERIMENTAL PARAMETERS AFFECTING THE IMAGING PERFORMANCES. 1—12
FIGURE 1-8 – OPTICAL SECTIONING CAN BE OBTAINED BY LIGHT SHEET OR TIRF APPROACHES. 1—13
FIGURE 1-9 – STRUCTURED-ILLUMINATION CONCEPT. 1—14
FIGURE 1-10 – NONLINEAR FLUORESCENCE EMISSION INTRODUCES HIGH FREQUENCY HARMONICS. 1—14
FIGURE 2-1 – A KOHLER INTEGRATOR. 2—2
FIGURE 2-2 – FLAT-FIELD ILLUMINATION EMPLOYING BEAM SHAPER DIFFRACTIVE ELEMENTS. 2—3
FIGURE 2-3 – SPECKLES AND INTERFERENCE FRINGES HOMOGENIZATION APPROACHES. . 2—4
FIGURE 2-4 – FLAT-FIELD TIRF ILLUMINATION USING AXICON LENS. 2—5
FIGURE 2-5 – OBJECTIVE TIRF LIMITATIONS. 2—6
FIGURE 2-6 – PRISM-TIRF AND OBJECTIVE-TIRF CONFIGURATIONS. 2—7
FIGURE 2-7 – CLASSICAL OBJECTIVE-TIRF AND WAVEGUIDE-TIRF APPROACHES. 2—8
FIGURE 2-8 – LIGHT SHEET APPROACH LIMITS. 2—9
FIGURE 2-9 – BEAM PROPAGATION FROM RECTANGULAR AND CIRCULAR APERTURE. 2—12
FIGURE 2-10 – DEPENDENCE OF THE LOCALIZATION ACCURACY ON THE PIXEL SIZE. 2—17
FIGURE 2-11 – DH-SMLM ALGORITHMS. 2—18
FIGURE 2-12 – DH-SMLM BEST-IN-CLASS ALGORITHM PERFORMANCE. 2—21
FIGURE 3-1 – C. CRESCENTUS CELL ENVELOPE. 3—25
FIGURE 3-2 – *C. CRESCENTUS* CELL CYCLE. 3—26
FIGURE 3-3 – TIME-LAPSE DUAL COLOR IMAGES OF *C. CRESCENTUS.* 3—26
FIGURE 3-4 – MODEL FOR CELL SIZE CONTROL AND HOMEOSTASIS IN *C. CRESCENTUS.* 3—27
FIGURE 3-5 – *C. CRESCENTUS* CELL SHAPE SCHEME. 3—29
FIGURE 3-6 – *C. CRESCENTUS* SHAPE IMAGES ANALYSIS. THE ANALYSIS OF 3—30
FIGURE 3-7 – *C. CRESCENTUS* SEPTUM SHAPE DYNAMICS. 3—32
FIGURE 3-8 – FROM 2D SMLM TO 3D DH-PSF DATA. 3—33
FIGURE 4-1 – LOCALIZATION PRECISION WITH SCMOS SPECIFIC MLE ALGORITHM. 4—36
FIGURE 5-1 – PARAMETER SPACE IN CELL SHAPE DYNAMIC STUDY. 5—43
FIGURE 5-2 – CELL SHAPE ANALYSIS PROGRAM SDADA PIPELINE. 5—45
FIGURE 5-3 – EDGE DETECTION OPTIMIZATION. 5—46
FIGURE 5-4 – POLE SIMULATOR MODEL. 5—47
FIGURE 5-5 – POLE SHAPE DYNAMICS AT THE CONSTRICTION SITE. A, AND C, 5—48
FIGURE 5-6 – DH-PSF TEMPLATE EXTRACTION. 5—49

FIGURE 5-7 – STORMCHASER PROGRAM PIPELINE. 5—50
FIGURE 5-8 – MOLECULE IDENTIFICATION STEP IS BASED ON CLUSTERING ALGORITHM. 5—51
FIGURE 5-9 – ARTIFICIAL DH-PSF DATASET. 5—51
FIGURE 5-10 – STORMCHASER RENDERING. 5—52
FIGURE 5-11 – 3D SMLM CHALLENGE RESULT COMPARISON. 5—54
FIGURE 5-12 – 3D SMLM CHALLENGE IMAGE RESULT. 5—55
FIGURE 6-1 – DEPENDENCE OF THE ILLUMINATION HOMOGENEITY ON THE DESIGN PARAMETERS. 6—57
FIGURE 6-2 – SCMOS ZYLA 4.3 ANDOR DARK IMAGE. 6—58
FIGURE 6-3 – SCMOS ZYLA 4.3 ANDOR READ NOISE AND GAIN DISTRIBUTION. 6—59
FIGURE 6-4 – HOT PIXELS IDENTIFICATION PROCESS. 6—60
FIGURE 6-5 – CMOS-SPECIFIC-MLE ALGORITHM AND RAPIDSTORM SOFTWARE COMPARISON. 6—62
FIGURE 6-6 – LARGE FOV STORM IMAGING OF MULTIPLE EUKARYOTIC CELLS. 6—63
FIGURE 7-1 – OPTIMIZED WAVEGUIDE DESIGN ENABLES A UNIFORM AND LARGE TIRF ILLUMINATION. 7—67
FIGURE 7-2 – LAYOUT OF THE WAVEGUIDE CHIPS FOR CLEANROOM FABRICATION. 7—68
FIGURE 7-3 – WAVEGUIDE PENETRATION DEPTH AND 1D TE0 WAVEGUIDE MODE SIMULATIONS. 7—69
FIGURE 7-4 – APPROXIMATED COUPLING EFFICIENCY ESTIMATION AND E11 WAVEGUIDE MODE PROFILE AT THE INPUT TAPER TIP. 7—70
FIGURE 7-5 – WAVEGUIDE-PAINT PLATFORM: WAVEGUIDE-CHIP INTEGRATION IN A CUSTOM UPRIGHT MICROSCOPE. 7—71
FIGURE 7-6 – WAVEGUIDE-PAINT IMAGING OF DNA-ORIGAMI MICROTUBULES. 7—74
FIGURE 7-7 – WAVEGUIDE-PAINT IMAGING OF COS-7 CELLS. 7—75
FIGURE 7-8 – WAVEGUIDE-PAINT IMAGING OF COS-7 CELLS. 7—76
FIGURE 7-9 – DEMONSTRATION OF WAVEGUIDE-PAINT. 7—77
FIGURE 7-10 – DIFFRACTION LIMITED AND DNA-PAINT. 7—78
FIGURE 8-1 – WORKSTATION NETWORK FOR BIG-DATA ACQUISITION AND ANALYSIS. 8—84
FIGURE 8-2 – MULTI-WELL WAVEGUIDE CHIP FABRICATION. 8—85
FIGURE C-3 – CHIP HOLDER – MECHANICAL DESIGN. 8—90

PART I

INTRODUCTION TO SUPERRESOLUTION FLUORESCENCE MICROSCOPY

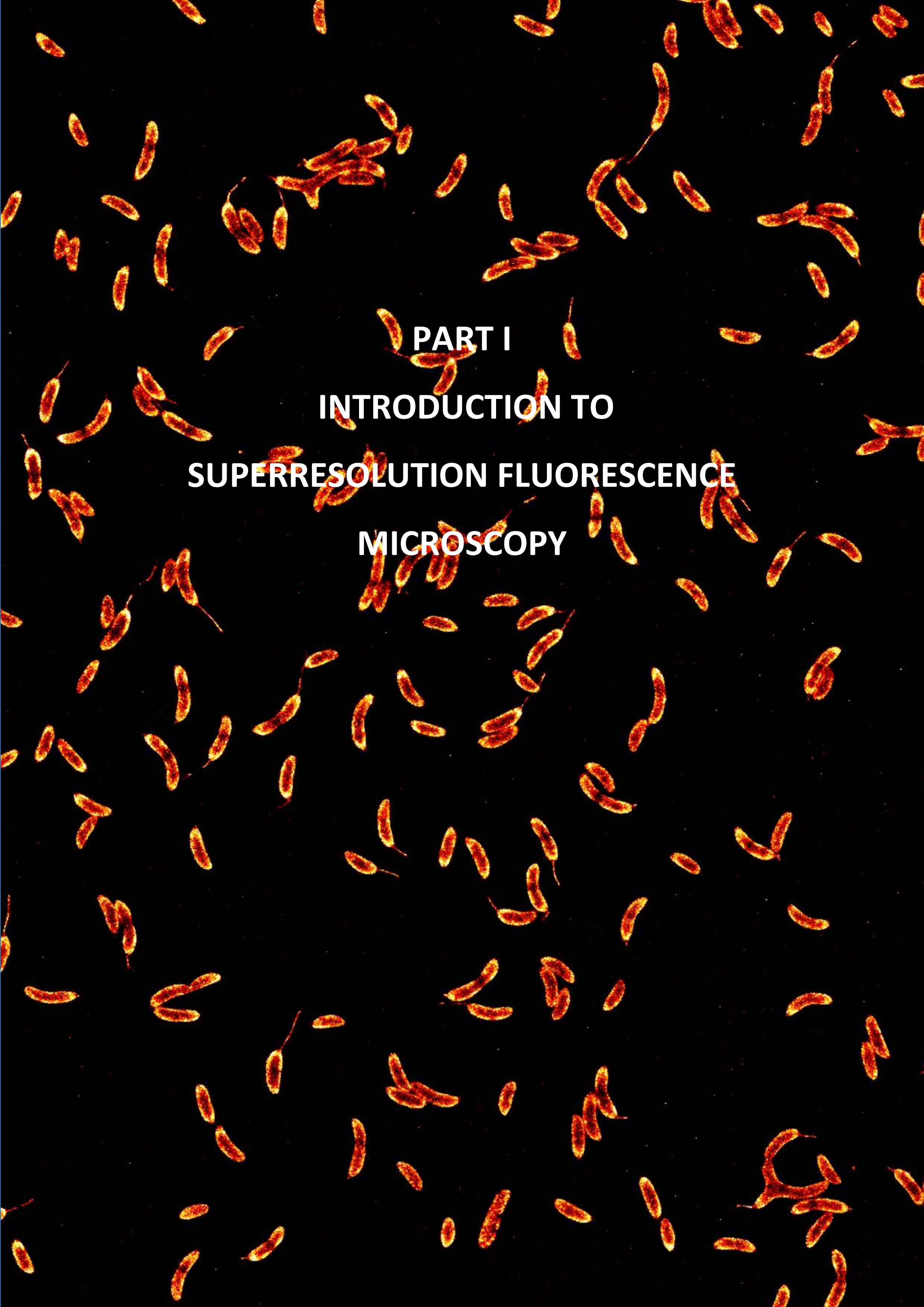

1 Super-resolution principles, methods and limitations

Fluorescence microscopy is a well-established imaging technique that allows non-invasive observation of dynamic processes within the cell, as well as probing specific proteins structure and location. During the last decades, continuous advancements were prompted by a broad, interdisciplinary effort, leading to key improvements like better labelling and increased spatial and temporal resolution. Nowadays, subcellular features can be specifically probed and resolved at a nanoscopic scale, thanks to superresolution microscopy, a set of fluorescence microscopy techniques so called for their capability to break the diffraction limit. This classical limit setting the maximum achievable spatial resolution can be described by the classical Abbe limit.

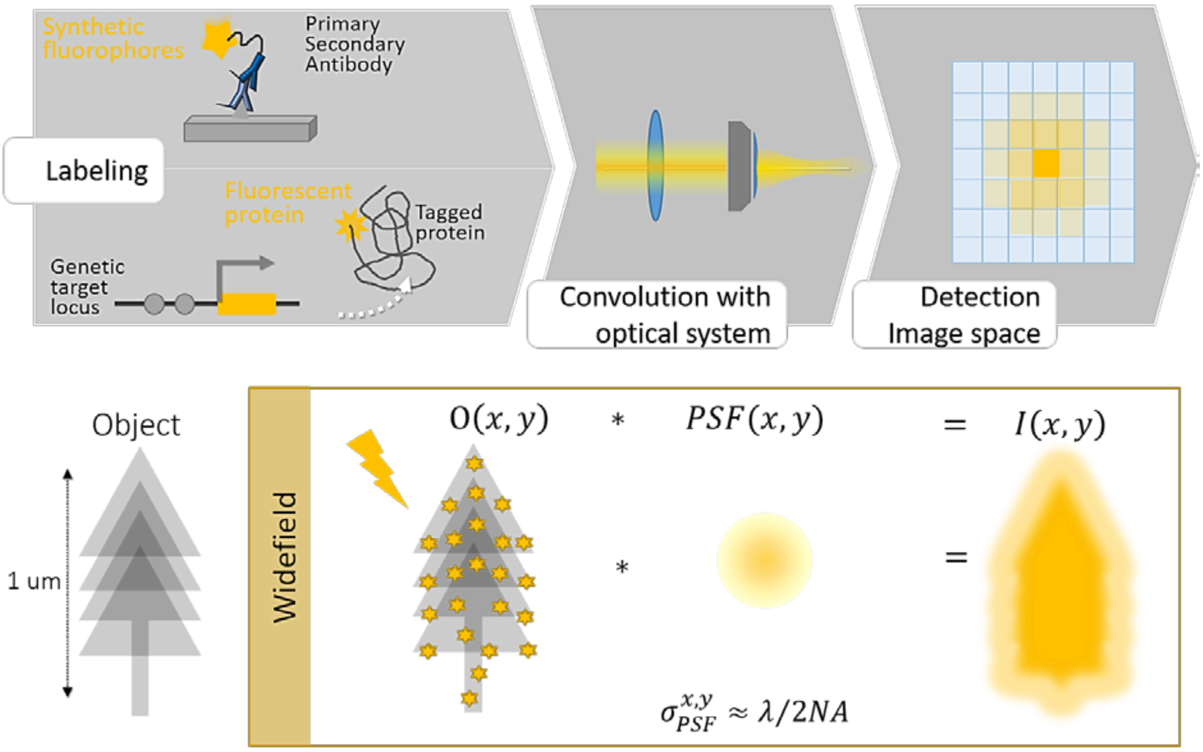
Synthetic fluorophores
Primary
Secondary
Antibody
Labeling
Fluorescent protein
Tagged protein
Genetic target locus
Convolution with optical system
Detection
Image space
Object
1 um
Widefield
$O(x,y)$
$*$
$PSF(x,y)$
$=$
$I(x,y)$
$*$
$=$
$\sigma_{PSF}^{x,y} \approx \lambda/2NA$

Figure 1-1 – Visualization of the imaging process. The imaging of square objects with an optical system with an impulse response described by the indicated PSF. The imaging operation, which is expressed by Equation 1, results in a blurred image of the object. The operator $*$ denotes the convolution operation.

When an ideal, dimensionless point-like object is imaged through a microscope, instead of appearing like an infinitesimal point it is actually rendered by the lens system as a blurred spot with an intensity profile defined by the response of the imaging system. Such an intensity profile is described by the point spread function (PSF) of the system. The image irradiance distribution $I(x,y)$ of an extended object $O(x,y)$ is thus the result of the object convolution with the system PSF:

$$I(x,y) = \iint O(u,v)PSF(x-u,y-v)dudv \tag{1.1}$$

where $PSF(x,y)$ is the impulse response of the optical system – i.e. the image of the impulse delta-function $\delta(x,y)$. The PSF hence defines the spatial resolution limit of an optical system: the Abbe diffraction limit.

The dimensions of the PSF, $\sigma_{PSF}^{x,y}$ and σ_{PSF}^{z} in the lateral (x - y) and axial (z) directions are in first approximation defined through the radial distance at which the value of the paraxial point spread function becomes zero:

$$\sigma_{PSF}^{x,y} \approx \lambda/2NA \tag{1.2}$$

$$\sigma_{PSF}^{z} \approx 2\lambda n/(NA)^2 \tag{1.3}$$

where λ is the wavelength of the emitted light, n is the index of refraction of the medium, and NA is the numerical aperture of the objective lens. Thus, the resolution limit for visible light ($\lambda \approx 550nm$) imaged by a high numerical aperture objective (oil immersion objective, $NA = 1.4$) is $\sigma_{PSF}^{x,y} \sim 200nm$ and $\sigma_{PSF}^{z} > 500nm$[1]. The PSF size will be more precisely described in Chapter 2.2.

	SIM			PALM/STORM	DNA-PAINT
	Linear	**Non linear**	**iSIM**		
Principle	Moiré effect with structured illumination		Multi-points scanning	Photoswitching and single molecule localization	Binding and unbinding of fluorescently labeled oligonucleotdes
Illumination emission	Linear	Non linear	Linear	Linear	Linear
Illumination excitation /Detection	Wide-field CCD/CMOS	Wide-field CCD/CMOS	Optical iterative points scanning and deconvolution	Wide-field CCD/CMOS	TIRF CCD/CMOS
X-Y resolution	100-130nm	50nm	1.7-fold in x,y	20-40nm	<20nm
Z resolution	250-350nm	Not applicable		<50nm (3D-STORM)	<50nm with spinning disk and astigmatism
Z range	10-20 μm	Not described	50-100 μm	100nm-few μm	
Time resolution	Milliseconds to seconds	Seconds to minutes	Milliseconds to seconds	Minutes	Several Minutes
Simultaneous colors	3	1	3-4	2	>10
Sample prep.	Easy	Easy	Easy	Difficult	Difficult

Table 1-1 Super-resolution light microscopy methods. The table presents a comparison between resolution, acquisition time and image colors achievable with the super-resolution approaches used in this work. Table based on [1,2,5–8] and [9].

In the last decade, several different fluorescence-based approaches have been developed in order to circumvent the intrinsic diffraction limitation.

In this work, I will mainly focus on one family within the super-resolution microscopy context: single molecule localization microscopy (SMLM) and specifically on Stochastic Optical Reconstruction Microscopy (STORM)[2] and DNA Points Accumulation for Imaging in Nanoscale Topography (DNA-PAINT)[3]. I will only briefly introduce the concept behind Structured Illumination Microscopy (SIM)[4], which is a patterned excitation approach we used to image *C.Crescentus* bacteria with a commercial microscope. Briefly, these two super-resolution techniques offer advantages which render them attractive over other super-resolution methods. In particular, SMLM techniques offer nanoscale resolution, which surpasses achievable resolutions by all fluorescence-based techniques. SIM on the other hand allows the acquisition of fast dynamics in living cells, with high spatial resolution using a relatively low laser irradiance.

1.1 Single Molecule Localization Microscopy (SMLM)

1.1.1 SMLM with photo-switching fluorophores

Among the most commonly used methods are localization microscopies (photoactivated localization microscopy, PALM[6] and stochastic optical reconstruction microscopy, STORM[2]). PALM and STORM are based on the photo-switchable properties of specific fluorescent molecules (fluorophores: fluorescent proteins or chemical dyes), which can be switched between a non–fluorescent (dark - OFF) state and a fluorescent (bright - ON) state by exposure to particular light wavelengths. In the case of dyes, photoswitching typically requires a reducing/oxidizing chemical buffer. Continuously acquiring images (frames) at a rate comparable with cycling the fluorophores between the OFF to an ON state makes it possible to distinguish each single fluorophores PSF within each frame. In such a way, it becomes possible to derive the actual fluorophore position from the analysis of its PSF with much better precision than analyzing the combined frames, as in widefield or even confocal microscopy (Figure 1-2).

The typical fluorophore switching rate ranges from $10\,Hz$ to $1000\,Hz$[10], thus limits the camera exposure time between $10\,ms$ and $100\,ms$ and the total acquisition time around 20 minutes to collect about 20 thousand images necessary for a sufficient target sampling.

The PALM and STORM methods, based on fluorophore localization, yield a spatial resolution down to approximately[2] $20nm$. This is due to the fact that the position μ_x of a single emitter can be determined to almost arbitrarily high accuracy if a sufficient number of photons generating its PSF are collected. Indeed, the localization precision of an estimation method, that assumes a Gaussian distributed PSF, can be defined in first approximation as the standard deviation of the estimated molecule location $\sigma(\mu_x)$ [11]:

$$\sigma(\mu_x) = \sqrt{\sigma^2(\mu_x)} = \sqrt{\frac{{\sigma_{PSF}}^2 + a/12}{N} + \frac{8\pi\sigma_{PSF}^4 b^2}{N^2 a^2}} \sim \sigma_{PSF}/\sqrt{N} \qquad 1.4$$

where a^2 is the pixel area, b^2 is assumed background expected noise per pixel, N is the number of expected photons and σ_{PSF} is the standard deviation of the point-spread function (assumed Gaussian distributed). The previous equation can be further improved by taking into account the EM gain of EMCCD cameras[12] (a more accurate description is reported in Chapter 2.3):

$$\sigma(\mu_x) = \sqrt{\sigma^2(\mu_x)} = \sqrt{\frac{2\sigma_{PSF}{}^2 + a/12}{N} + \frac{8\pi\sigma_{PSF}^4 b^2}{N^2 a^2}} \tag{1.5}$$

The localization precision is thus improved by increasing the number of emitted photons – more precisely by $\sqrt{N}$ – which increases with the illumination intensity.

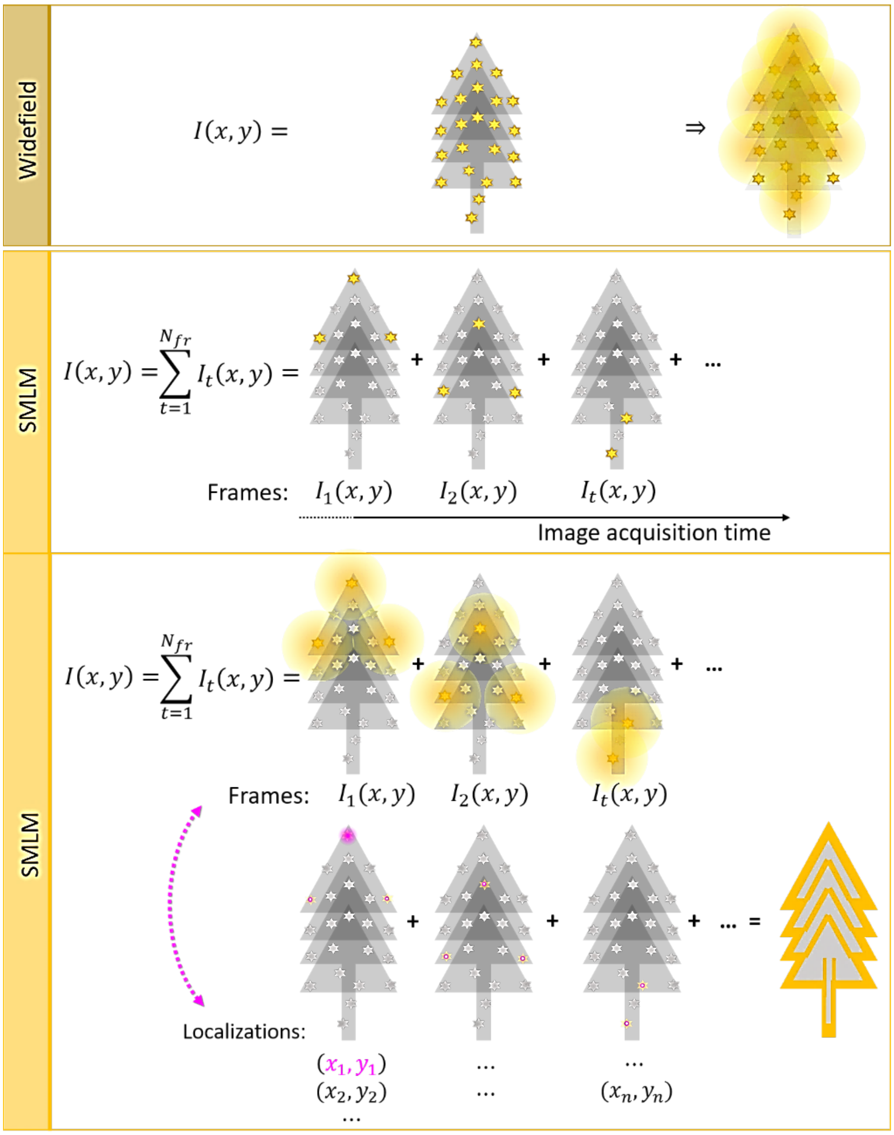
Widefield
$I(x,y) =$
⇒
SMLM
$I(x,y) = \sum_{t=1}^{N_{fr}} I_t(x,y) =$
+
+
+ …
Frames: $I_1(x,y)$ $I_2(x,y)$ $I_t(x,y)$
Image acquisition time
SMLM
$I(x,y) = \sum_{t=1}^{N_{fr}} I_t(x,y) =$
+
+
+ …
Frames: $I_1(x,y)$ $I_2(x,y)$ $I_t(x,y)$
+
+
+ … =
Localizations:
(x_1, y_1)
(x_2, y_2)
…
…
…
…
(x_n, y_n)

Figure 1-2 – Single Molecule Localization Microscopy concept. The top image represents the standard wide filed fluoresce microscopy approach: the image of a target fluorescently label is a diffraction limited image of the target. In a single molecule localization microscopy approach (bottom), the target structure of interest is labeled with photo switchable fluorophores. At the imaging start, all fluorophores are in a non-fluorescent OFF state upon irradiation with light of appropriate wavelength and intensity. A sparse subset of fluorophores is reactivated in an ON state either spontaneously or photo-induced with a second irradiation laser wavelength. The activated fluorophores, spaced further apart than the Nyquist's limit, can be precisely localized. Repetitive activation, localization and deactivation allow a temporal separation of spatially unresolved structures in a reconstructed image.

However, the intensity of the excitation light has a limit imposed by both phototoxicity and photobleaching. Toxic effects of light primarily arise due to generation of chemically reactive species such as free radicals and specifically singlet and triplet forms of oxygen[13]. Reactive oxygen species react with a large variety of cellular components that can easily oxidize, such as proteins, nucleic acids and lipids[14,15] and can be critical in the mitochondria respiratory chain for DNA-damage determination[16] and for directing the cell towards life or death[17]. These undesired reactions lead to loss of fluorescence signal (photobleaching) and physical damage to the cell or even cell death (phototoxicity).

Besides localization precision, another practical factor limits the resolution in PALM and STORM: the labeling density[18]. Too-low density of localizations results in an under-sampled structure, insufficient to resolve its organization[19]. Thus, leading to a loss of spatial information. On the other hand, if the fluorophore density is too high the images of individual fluorophores will overlap, thereby preventing each fluorophore from being localized with high precision.

Nyquist's criterion defines in first approximation the lower limit of the labeling density: the fluorophore-to-fluorophore distance, which is the inverse of "sampling frequency", has to be at least two times smaller than the smallest sample structural feature that has to be discerned[20]. If ρ is the density of labeling and D is the dimension of the sample that has to be imaged, the smallest resolvable feature size thus is defined via[19,21]:

$$\Delta_{nyq} \sim 2/\rho^{1/D} \qquad 1.6$$

which is two dimensions becomes:

$$\Delta_{nyq} \sim 1/\sqrt{\rho} \qquad 1.7$$

Therefore, to achieve 10-nanometer resolution, molecules must be spaced a minimum of 5 nanometers apart in each dimension to yield a minimum density of 4×10^4 molecules per square micrometer. This means, that in a diffraction-limited region of 250-nanometers in diameter (about 0.05 square micrometer) there should be about 2000 molecules to achieve 10-nanometer resolution. Since only one of these fluorophores should reside in its fluorescent state per cycle, the lifetime of the OFF state (τ_{OFF}) has to be 2000 times longer than the lifetime of the fluorescent ON state (τ_{ON}). τ_{OFF} has been reported to vary from 10 to $100\ ms$ to several seconds[10]. The lifetime of the ON state depends both on the fluorescence lifetime (the average time the molecule stays in its excited state before emitting a photon) and the number of times the molecule can cycle between its singlet ground state and the excited state before undergoing stochastically in the OFF state. Typical fluorescence lifetimes are within the range of 0.5 to 20 nanoseconds and the molecule can emit a photon about 1000 times before switching OFF. Therefore, the total time τ_{ON} a molecule can stay in the ON state is of few milliseconds at most.

Fluorophores with a higher τ_{OFF}/τ_{ON} ratio allow the sample to be labeled with higher density since the risk of false localizations caused by the overlapping of multiple fluorophore signals within the same diffraction-limited area, is lower. On the other hand, high photoswitching ratios result in a small number of localizations per image and thus prolong the acquisition time unnecessarily.

However, it is important to underline that the argument concerning the resolution link to label density is only true in a first approximation. Indeed, resolution also depends strongly on the underling sample structure, the presence of not uniform background and localization precision and can therefore be better described by the following expression[22,23]:

$$\Delta_{nyq} \sim 1/\sqrt{log\ \rho} \qquad 1.8$$

Today, fluorophores have become highly optimized in their targeting, photostability, and photoswitching[24–26] to make it possible to routinely resolve structures down to the nanometric scale.

1.1.2 *3D SMLM approaches*

Cells and their intra-cellular structures and organelles are fundamentally three-dimensional. For this reason, many efforts have been employed to access the third spatial dimension and to improve axial resolution. As previously mentioned, this work focuses mainly on the SMLM family. However, I will briefly compare the advantages and disadvantages of the SMLM approach with SIM: another approach we could easily access at EPFL through a commercially available microscope.

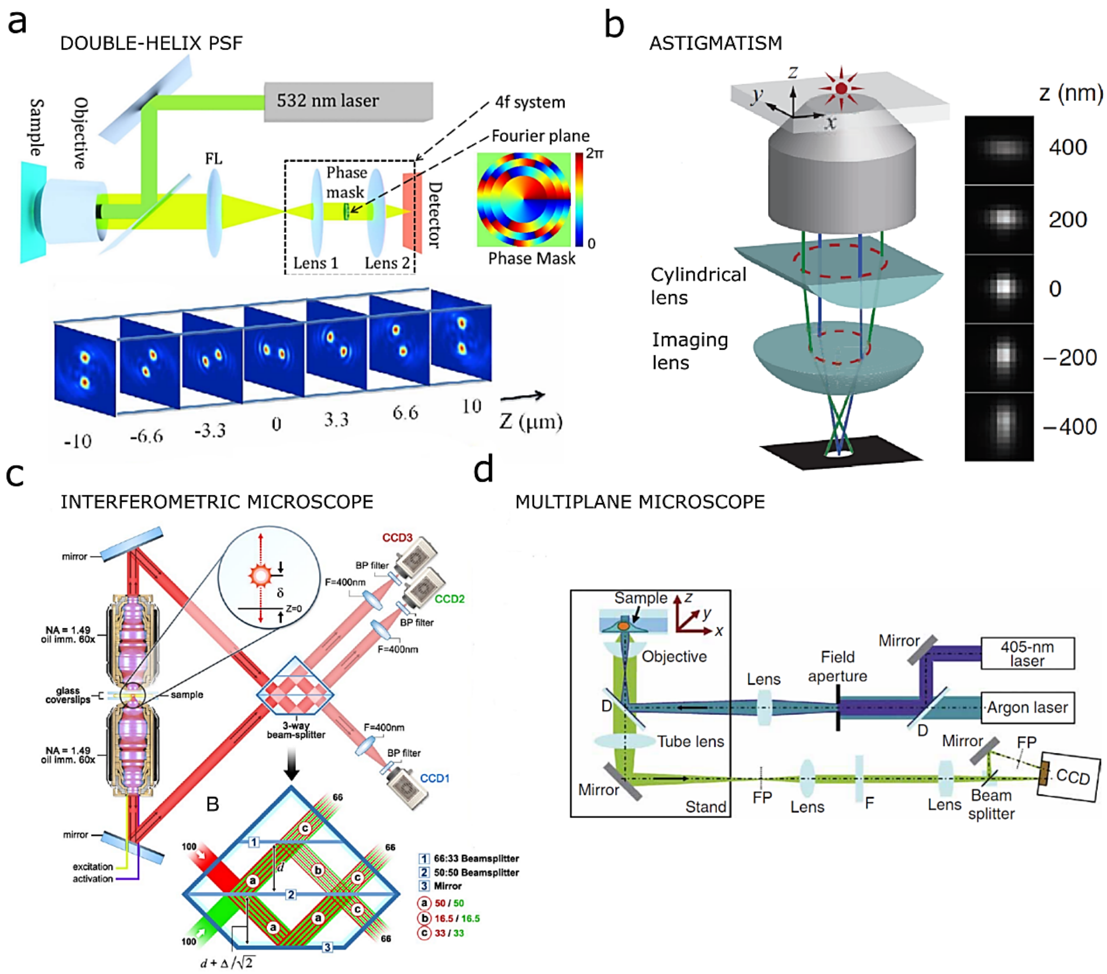
a
DOUBLE-HELIX PSF
532 nm laser
Sample
Objective
FL
Phase mask
Lens 1
Lens 2
Detector
4f system
Fourier plane
2π
0
Phase Mask
-10
-6.6
-3.3
0
3.3
6.6
10
Z (μm)
b
ASTIGMATISM
z
y
x
Cylindrical lens
Imaging lens
z (nm)
400
200
0
−200
−400
c
INTERFEROMETRIC MICROSCOPE
mirror
NA = 1.49 oil imm. 60x
glass coverslips
sample
NA = 1.49 oil imm. 60x
mirror
excitation
activation
δ
Z=0
CCD3
BP filter
F=400nm
CCD2
BP filter
F=400nm
3-way beam-splitter
F=400nm
BP filter
CCD1
B
100
100
66
66
66
d
d + Δ/√2
1 66:33 Beamsplitter
2 50:50 Beamsplitter
3 Mirror
a 50 / 50
b 16.5 / 16.5
c 33 / 33
d
MULTIPLANE MICROSCOPE
Sample
z
y
x
Objective
D
Tube lens
Mirror
Stand
Lens
Field aperture
Mirror
405-nm laser
Argon laser
D
Mirror
FP
FP
Lens
F
Lens
Beam splitter
CCD

Figure 1-3 – 3D SMLM approaches. a, Typical DH-PSF of a conventional wide-field microscope at different axial planes[37] (top); The phase mask is mounted in the Fourier plane, which is the center plane between Lens 1 and Lens 2 forming a 4f system. The phase mask is typically made of positive photo-resist (AZ-4210, Clariant) spin-coated on a glass slide with different thicknesses to generate different phase delays[38]. The simulated phase mask pattern shown approximates the double helix phase mask reported in [30]; **b,** Optical diagram to produce the desired astigmatic aberration of the PSF by introducing a cylindrical lens into the imaging path. The z coordinate is extracted from the ellipticity of its image. The right panel shows images of a fluorophore at various z positions[29] ; **c,** Schematics of an single-photon fluorescence interferometric microscope. A point source emits a single photon both upwards and downwards. The single photon interferes in a special 3-way beam splitter. Since, the difference in path lengths of the upper and lower beams directly depends on the axial position of the source, the axial position of the source molecule can be determined from the relative amplitudes of the source images from the 3 cameras[31]**; d**, Optical diagram of a multiplane microscope implemented into a conventional microscope for wide-field. Emission fluorescence is split into two paths to create two separate image planes on the same CCD camera[32].

Linear SIM has provided $\sim 100\ nm$ lateral and $\sim 300\ nm$ axial resolution in the mammalian nucleus [27], while non-linear SIM has so far only been demonstrated in two dimensions[28].

With single molecule microscopy techniques such as PALM/STORM, it is possible to simultaneously achieve higher lateral (around $\sim 25\ nm$) and axial resolution (around $\sim 50\ nm$)[1]. However, current 3D

PALM/STORM are limited to a maximal depth range of $100\ nm - few\ \mu m$ whereas 3D SIM has an axial range of $10\ \mu m - 20\ \mu m$[8].

For application where 3D resolution weight more than imaging depth, 3D SM approaches are the methods of choice. Different techniques have been developed for far-field SM localization microscopy based on the PSF engineering (such as astigmatic imaging[29] and double-helix (DH) PSF[30]), interferometry (such as iPALM- where the axial position is calculated from single photon interference between opposing objectives[31]) and multiplane imaging[32]. In the multiplane approach, the axial information is extracted from the simultaneous measurement of the PSF shape at different focal planes. Multiplane provides 3D imaging over a depth of less than one micron without axial scanning at a resolution of 30 nm laterally and 80 nm axially and over several micron with axial scanning[32]. However, this approach requires either the use of two cameras, which introduces synchronization and cost drawbacks, or the binning of one camera, which limits the field of view. While extremely precise[31] – its achievable axial resolution is 10-20 nm – the interferometric approach is not yet widely adopted. This is most likely due to the ease of adopting 3D capability by commercial engineered PSF or adding a simple lens to existing standard microscopes whereas an upgrade to iPALM requires extensive modification. The realization of a 3D single molecule platform based on the introduction of commercial engineered PSF or a lens, is easier to achieve with respect to the interferometric PALM technique which requires extensive modifications of a standard microscope[33] (see Figure 1-3). Additionally, the PSF engineering approach has a longer depth range with respect to pure interferometry. In fact, in the interferometric system the maximum depth is about $200\ nm$ [31], while the astigmatic and DH-PSF approaches provide a depth of field of about $600\ nm$ [34] and $2-3\mu m$ [33,35] respectively.

All together, a DH-PSF microscope is the technique that allows one to achieve the best axial localization precision (up to $20\ nm$) and lateral localization precision ($10\ nm$) over an axial range larger than $2\ \mu m$ [30]. The DH method is based on an engineered phase mask that, when added to a conventional widefield microscope, enables the generation of a PSF that changes with focus depth. The PSF generated by this mask appears as two bright lobes which revolve around one another as a function of z-axial position[36] (Figure 1-3 a and Figure 1-4).

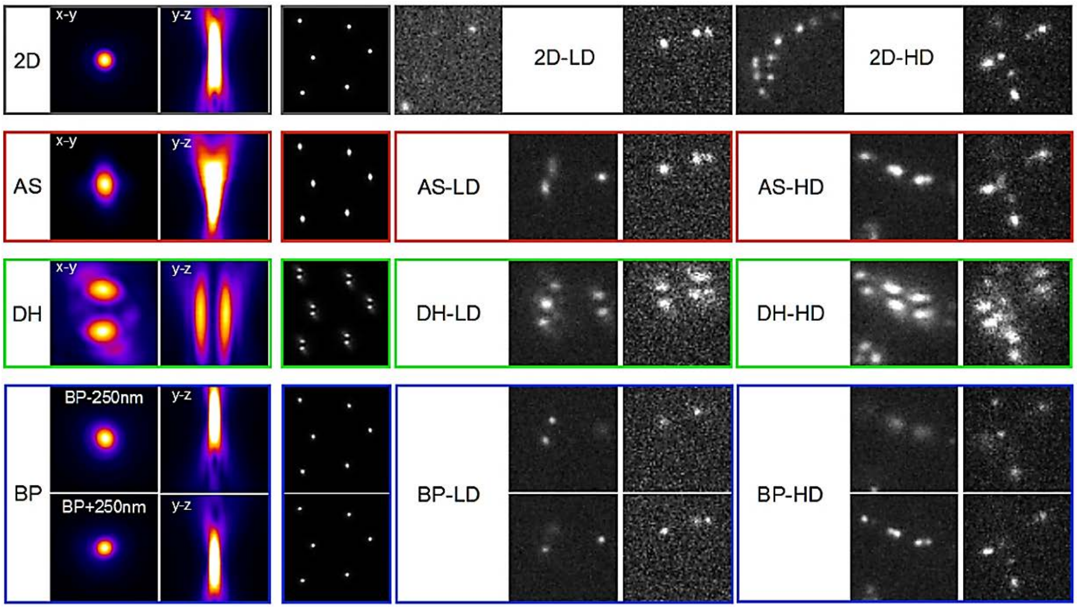

Figure 1-4 – 3D-PSF simulated dataset . Summary of different simulated datasets. Each dataset is characterized by its structure (endoplasmic reticulum (ER) or microtubules (MT)), by its modality (two dimensional (2D), astigmatic (AS), double helix (DH), biplane (BP)), its density (low density (LD) or high density (HD) and by its SNR determined by the level of noise. Figure taken from [39].

The angle of the axis connecting the center of the two lobes relative to a fixed reference axis, will encode the z position. The center of the midpoint between these two centers yields the lateral position of the fluorophore (Figure 1-3 a). A current limitation of this approach is set by the overall large size occupied by the two lobes of the PSF distribution. At high molecule density, DH-PSFs tend to overlap more frequently affecting the SNR and localization precision. Thus, the improved axial resolution and extended range introduced by DH-PSF engineering comes at the cost of limiting the experimental acquisition to low molecule density conditions.

1.1.3 *DNA Points Accumulation for Imaging in Nanoscale Topography (DNA-PAINT)*

“Points Accumulation In Nanoscale Topography” (PAINT)[40] provides several improvements over the above mentioned SMLM techniques such as precise and quantitative multiplexed imaging capability for in vitro or in situ experiments[3,41–44]. It combines multi-pseudocolor (more than ten tones) imaging with optimal localization precision and specificity[3]. Unlike other stochastic super-resolution methods, DNA-PAINT employs non-photoswitching fluorophores which do not blink between different fluorescence states. Instead, it leverages on the stochastic binding and unbinding of fluorescently labeled oligonucleotides ("imager" strands) in DNA-PAINT[3,42] and protein-fragment probes in ‘integrating exchangeable single-molecule localization’ (IRIS)[45] to obtain the same blinking effect.

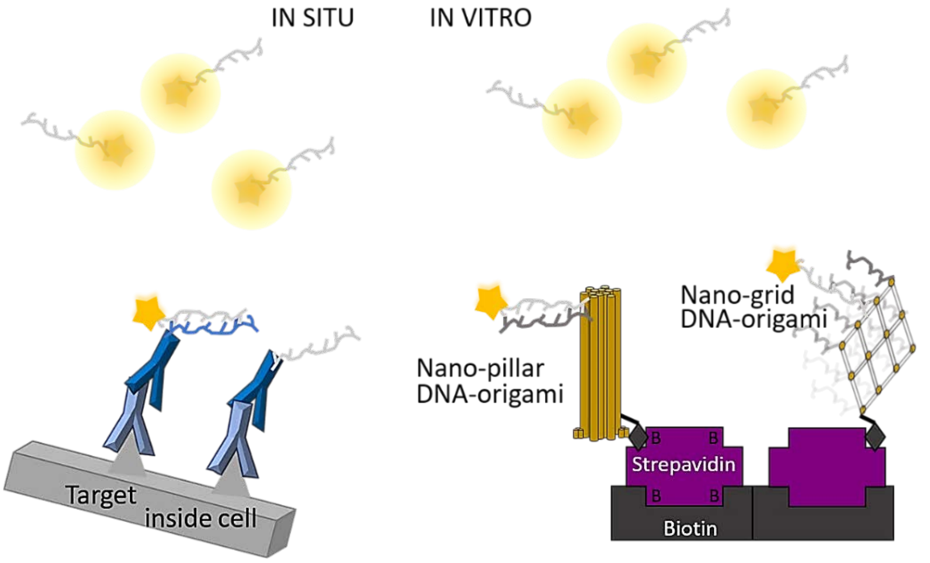

Figure 1-5 – DNA-PAINT sample scheme. Cell antibodies are chemically modified to become DNA-conjugated antibodies and used for in situ DNA-PAINT imaging of fixed cells (Left). DNA origami nanostructures can be easily seeded on BSA/biotin/streptavidin-coated surface for in vitro experiments (Right)[44]**.**

The sampling of the target sites with imager strands that are continually replaced, provides an effective solution to photobleaching, which limits standard fluorescence imaging approaches. Moreover, tagging the target with diverse docking strands and probing them with their respective complementary imager strands, enables sequential pseudo-color imaging with unlimited multiplexing. DNA-PAINT offers the possibility to perform *in situ* imaging of fixed cells or *in vitro* imaging of DNA-origami structures (Figure 1-5).

The *in situ* protein-labeling strategy is based on immunostaining with DNA-conjugate primary-secondary antibodies, where the antibodies are chemically modified to link the DNA-docking strand to the secondary antibody.

In vitro DNA origami structures provide a framework to test a fluorescence microscopy method by placing defined numbers of small molecules at nano-metric distances in a programmed way as distinct calibration marks[43].

DNA origami structures are created by folding a long single strain DNA molecule named ‘scaffold-strand’. The folding process is set by the specific binding of hundreds of short synthetic oligonucleotides (‘staple-strands’) to precise predefined regions on the scaffold[46,47] (Figure 1-6). To allow DNA-PAINT imaging, the staple strands of the DNA-origami structure are usually extended by adding single-stranded docking sites that can bind to the imager strands[41].

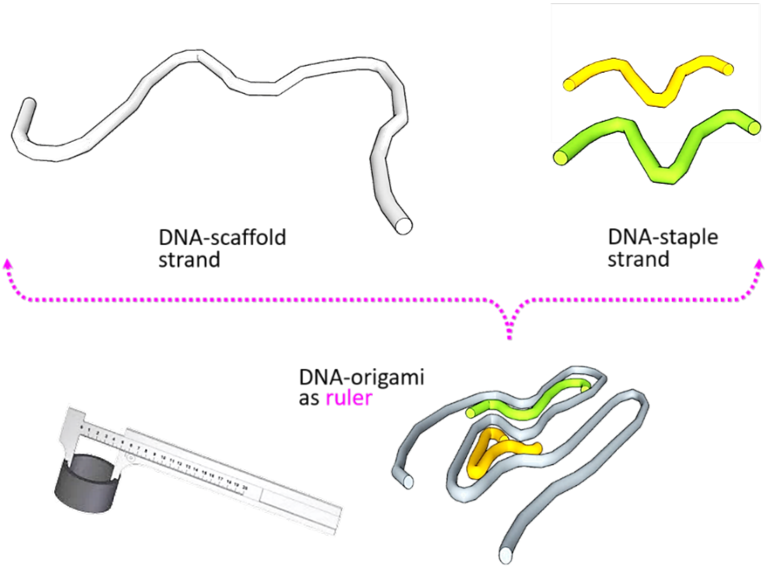

Figure 1-6 – DNA-ORIGAMI creation principle. DNA-nanoshapes are mainly made by a long DNA-scaffold strand. The scaffold strand is bent using DNA-staple strand placed at the designed corresponding scaffold-strand sites. The origami has exactly the size and shape design and can thus be used as a caliber to measure other unknown structures.

The sample and experiment design of both *in situ* and *in vitro* experiments can strongly affect the resulting performance of the experiment (such as achievable spatial and temporal resolution – see Figure 1-7). For example, when decreasing the site distance or increasing the imager strand concertation, the dark time τ_d (inter-event lifetime) decreases, which leads on one hand to a lower total imaging time but on the other hand to a higher probability of SM-PSF overlapping and hence lower localization precision. The following expression defines through τ_d, the necessary time to have at least one binding event with a probability higher than 98%:

$$P(1\ binding\ in\ \Delta t) = \int_0^{\Delta t} \frac{1}{\tau} e^{-\frac{t}{\tau}}\, dt = 1 - e^{-\frac{\Delta t}{\tau}} > 98\% \qquad 1.9$$

$$\Delta t > ln(1\ - 0.98)^{-1} \cdot \tau_d$$

$$\Delta t > 4 \cdot \tau_d$$

Since $\tau_d = (k_{on} \cdot c\,)^{-1}$ where c is the imager strand concentration (typically about 1-10 nM), and k_{on} the probe association rate (typically of 10^6 Ms^{-1}) the necessary waiting time for at least one binding event is about 100-1000s and a total imaging time of 400-4000s (10-60 minutes).

Another important parameter is the binding time τ_b (or the dissociation rate $1/\tau_b$) which exponentially depends on the length of the strand duplex (number of base pair for the binding). The design and estimation of such parameters determine the signal to noise (SNR) and the camera exposure time. Increasing the imager strand length increases the number of photons generated during one single binding event. However, this increase in Signal to Noise Ratio (SNR) comes at the expense of exposure time required to image a sample.

A major advantage of PAINT is that fluorophores in solution can iteratively sample the structures of interest[48], in a process that is only limited by the patience of the experimentalist[49]. Other advantages include the unlimited multiplexing of EXCHANGE-PAINT for multicolor imaging[3] and the possibility to quantify the number of binding sites at each location using qPAINT[50].

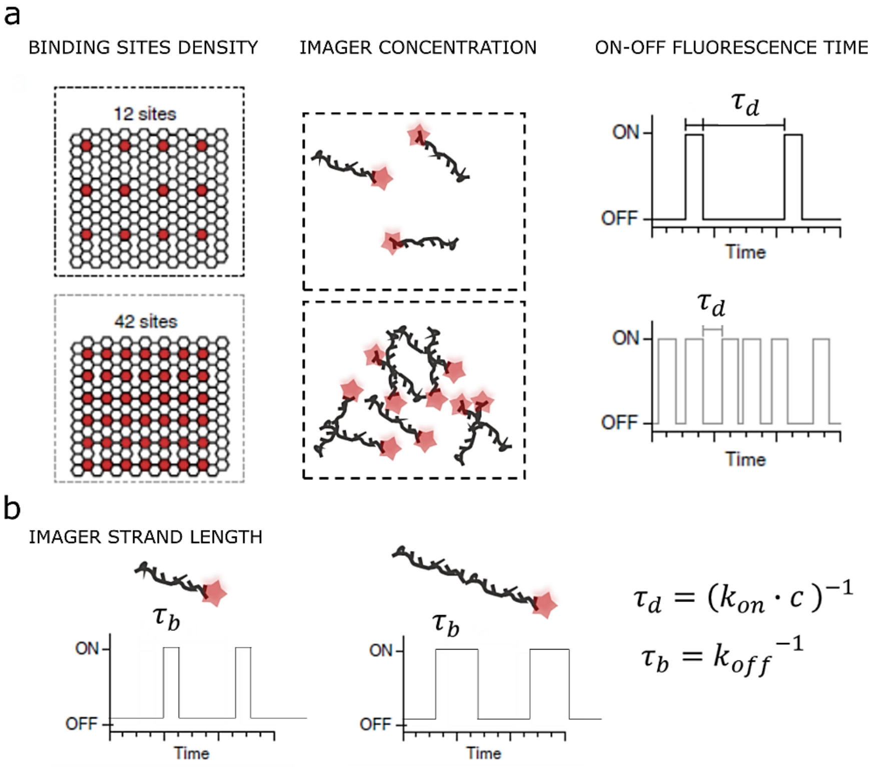

Figure 1-7 – DNA-PAINT experimental parameters affecting the imaging performances. **a**, The site density or the imager concentration affect the dark time τ_d (inter-event lifetime) and thus the total imaging time. **b**, The imager strand length affects the signal to noise but also the necessary camera exposure time. Figure inspired by [44].

To allow binding and dissociation, PAINT requires a reservoir of fluorescent probes (e.g. labelled DNA oligos) in solution surrounding the sample, which brings its own limitations to the method. First, it requires axial optical sectioning to reject the background signal from fluorophores in solution. This can be mitigated in the case of fluorescence enhancement upon binding as for fluorogenic dyes[40], quenching of unbound probes[51] or Förster resonance energy transfer-(FRET) PAINT[52,53]. However, these approaches come at the cost of reduced labeling flexibility, increased sample preparation complexity and a potential reduction in localization precision[54,55].

Although DNA-PAINT offers several advantages such as continuous replacement of possible bleached molecules, as well as high localization signal and large fluorophores pool availability, it presents two main challenges for the imaging system.

First, DNA-PAINT requires an optical sectioning illumination to minimize the background signal from the unbound imager strands. The most common way to realize such an illumination is either through objective-based Total Internal Reflection Fluorescence (TIRF) technique or light sheet illumination (Figure 1-8). However, both these two approaches are limited either in FOV size or uniformity. We will investigate the limitations of these approaches more deeply in the next Chapter 2.1.

A second DNA-PAINT limitation is set by the trade-off between binding duration and localization precision. To improve the localization precision, the most effective way is increasing strand length – and thus binding duration. This increases the number of photons generated during one single binding event. But the elevated Signal to Noise Ratio (SNR) comes at the expense of exposure time required to image a sample, which is typically ten times higher than other localization-based microscopy methods, such as PALM or STORM (a few hundred milliseconds instead of ten milliseconds)[44].

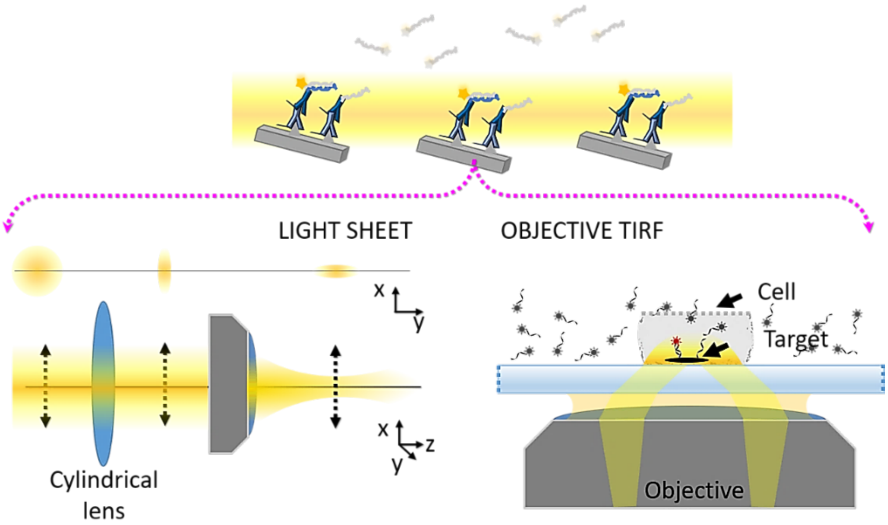

Figure 1-8 – Optical sectioning can be obtained by light sheet or TIRF approaches. DNA-PAINT requires optical sectioning to suppress the background generated by the fluorophore in solution. This can be obtained either with light sheet or TIRF microscopy.

Using waveguide-based evanescent field systems instead of the standard TIRF configuration for DNA PAINT microscopy, has several advantages. First, a waveguide illumination separates the excitation light from the fluorescence emission path, making it possible to achieve a uniform and large excitation field target, and to optimize the objective for the sole imaging purpose.

The larger excitation field leads to more sample being exposed within one FOV. Total data throughput is thus increased and acquisition times reduced. Furthermore, evanescent field illumination offers greater freedom in customizing the chip design to better fit the set up where it will be integrated. Although waveguide evanescence field illumination has been tested in fluorescence microscopy[56–59] and in superresolution microscopy[60], applying this solution to DNA PAINT imaging requires an apparatus capable to produce the required evanescent field, combined with a fast buffer exchange, with a specific design for the waveguide-chip and the microscope integration. We present in Chapter 4.2, an illumination field of uniform evanescent light, a flexible waveguide-based platform that provides a large and uniform evanescent excitation over a 100 × 2000 μm^2 area.

1.2 Structured illumination microscopy (SIM)

In the context of super-resolution, Structured Illumination Microscopy (SIM) is a wide-field microscopy technique which utilizes the projection of a known illumination pattern (often sinusoidal grids) onto the sample to extract higher resolution information[4,61]. In a diffraction limited microscope, the observable spatial frequencies in the sample define a circular region of radius $k_0 \sim 2NA/\lambda$ in the Fourier space (Figure 1-9, a) set by the diffraction limit of light. But, if the excitation light is modulated by a spatial frequency k_1, such as a sinusoidal pattern, previously unobservable information – containing frequencies from outside of the observable region – becomes encoded in the form of Moiré fringes. By recombining multiple images in Fourier space with different pattern positions and orientations, a super-resolved image is obtained with the maximum detectable spatial frequency increased to $k_0 + k_1$ (Figure 1-9, b) [4,61].

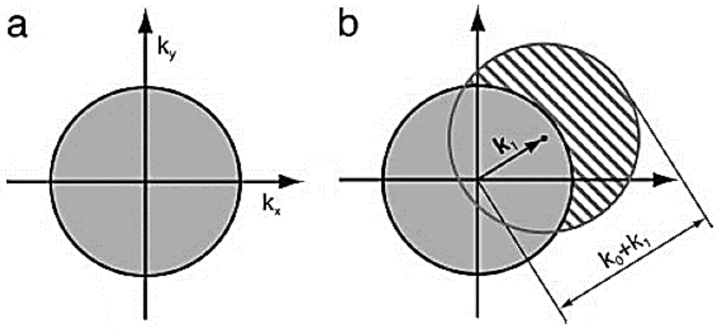

Figure 1-9 – Structured-illumination concept. (a) The set of sample spatial frequencies that can be observed by the conventional microscope defines a circular observable region of radius $\boldsymbol{k_0}$ in frequency space. (b) If the excitation light contains a spatial frequency $\boldsymbol{k_1}$, a new set of information becomes visible in the form of Moiré fringes (hatched circle). This region has the same shape as the normal observable region but is centered at $\boldsymbol{k_1}$. The maximum spatial frequency that can be detected (in this direction) is $\boldsymbol{k_0} + \boldsymbol{k_1}$ [62].

Since the projection of the illumination pattern itself is limited by the diffraction of light, the resolution limit can be extended by a factor 2 at most in the linear case. However, if the sample's fluorescence emission is non-linearly dependent on the illumination pattern intensity, such as in a saturated regime (Saturated Structured Illumination Microscopy – SSIM), the emission pattern could in principle contain arbitrarily higher spatial frequencies than the illumination pattern itself[62]. This particular nonlinear phenomenon is due to the non-instantaneous photon emission process of an excited fluorophore. After photon absorption, the fluorophore needs an average time (the fluorescence lifetime) to relax back to the ground state with a photon emission. Therefore, it cannot respond linearly to the illumination intensities above one photon per absorption cross section per lifetime.

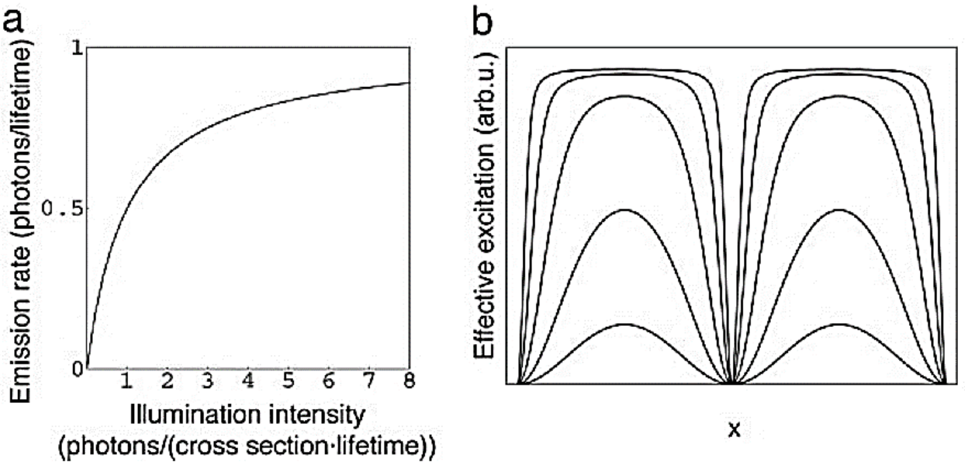

Figure 1-10 – Nonlinear fluorescence emission introduces high frequency harmonics. Figure (a) shows the nonlinear dependence of the fluorescent emission rate on the illumination intensity in the saturation regime. (b) The emission pattern resulting from sinusoidal patterned illumination with different peak pulse energy densities (from the bottom to top curve 0.25, 1, 4, 16, and 64 times the saturation threshold) [62].

If a sample is illuminated with a sinusoidal light pattern that has a light intensity above this threshold, the emission rate per fluorophore thus has a pattern with a nonsinusoidal shape (Figure 1-10). This pattern of emission contains higher spatial frequencies than the illumination pattern itself. Unfortunately, saturation requires extremely high light intensities that are likely to accelerate photobleaching and photodamage, making this implementation non suitable for studies of living cells.

However, another nonlinear SIM approach was later implemented by exploiting the optical photoswitching property of select fluorophores such as Dronpa fluorescent protein[63] to provide the required nonlinearity. Photoswitchable fluorescent molecules can be reversibly switched between a fluorescent ON state and nonfluorescent OFF state using light with two different wavelengths. Saturating either of these population states results in a nonlinear relationship between the fluorescence emission and the illumination intensity. In this case, the required intensity is six orders of magnitude lower than the one necessary in the traditional saturated SIM[63]. Thanks to this principle, a resolution of $<50nm$ has been achieved with non-linear SIM on purified microtubules labeled with the fluorescent photoswitchable protein Dronpa[63].

2 Image quality limitations in SMLM

The resolution, uniformity and size of a final reconstructed SMLM image is affected by several factors:

- the sample preparation (e.g. label density[64] and other general properties of a fluorescent molecule such as ON-OFF possible kinetics, duty cycle and photon budget[65])
- the sample illumination
- the fluorescence detection process (e.g quantum efficiency[66] of the setup, camera critical parameters such as quantum efficiency, read noise and speed, duration of the acquisition, background),
- the molecule localization and super-resolved image rendering processes[36] (i.e. the adopted localization algorithm)

We previously focus on the implication of the label density (i) on the image reconstruction quality. In this Chapter, we will discuss why the sample illumination (ii) quality is critical for SMLM image quality and the main approaches adopted to address the current challenges. We will also explore the advantages and disadvantages of different localization algorithms (iv). Further (Chapter 4.1), we will investigate the critical camera aspects setting the limit to the molecules detection process (iii).

2.1 Illumination aspects critical for image quality

Sample illumination is particularly critical in SMLM where the single molecule (SM) sampling uniformity and localization precision define the achievable super-resolved image resolution and quality. Indeed, intensity, background and uniformity of the illumination approach set the SMs density per frame (through the activation or photo-switching rate illumination intensity[5]) and their signal to noise and thus the continuity of the target sampling and the SM position estimation accuracy.

In this chapter, we will explore the possible factors that strongly influence and limit the sample illumination qualities such as the global and local spatial dependence of the illumination field resulting from a Gaussian beam and from the interference of coherent light respectively. Moreover, we will compare different illumination approaches adopted to reduce out of focus fluorescence background that arises from a standard epi-illumination.

Focusing an excitation beam at the objective's back focal plane produces a wide-field illumination with an illumination spot size proportional to the objective's numerical aperture (NA). Since the irradiance distribution of the input beam at the back focal aperture is typically Gaussian, the resulting illumination spot will present an intensity drop moving from its center to the periphery.

This aspect leads to different limitations. The irradiance inhomogeneity compromises the localization precision across the FOV and forces either to limit the final image to the central part of the FOV, where the irradiance meets the requirement for doing SMLM (1–10 kW cm^{-2} for STORM and PALM)[66,67], or to image over a longer acquisition time than the one achievable by flattening the same irradiance. When the irradiance is too high, the emitter density per frame is low and the acquisition time to sample all the possible labelled sites becomes long. On the other hand, where the irradiance is too low, the molecule density per frame is high and with low signal. The result can be both the production of artifacts and a lower resolution. The illumination uniformity is therefore fundamental for the optimization of the quality, time and size of a SMLM imaging process.

2.1.1 *Global field flattening with Köhler integrator or beam shaping elements*

The Köhler integrator[68,69] has been previously adopted to address this need. Our work presents a straightforward integration and extension of this solution in a SMLM CMOS-based microscope[70]. A Köhler integrator is a combination of multiple parallel Köhler illumination systems, typically realized with microlens arrays, which minimizes both the spatial and angular dependence of the light source irradiance.

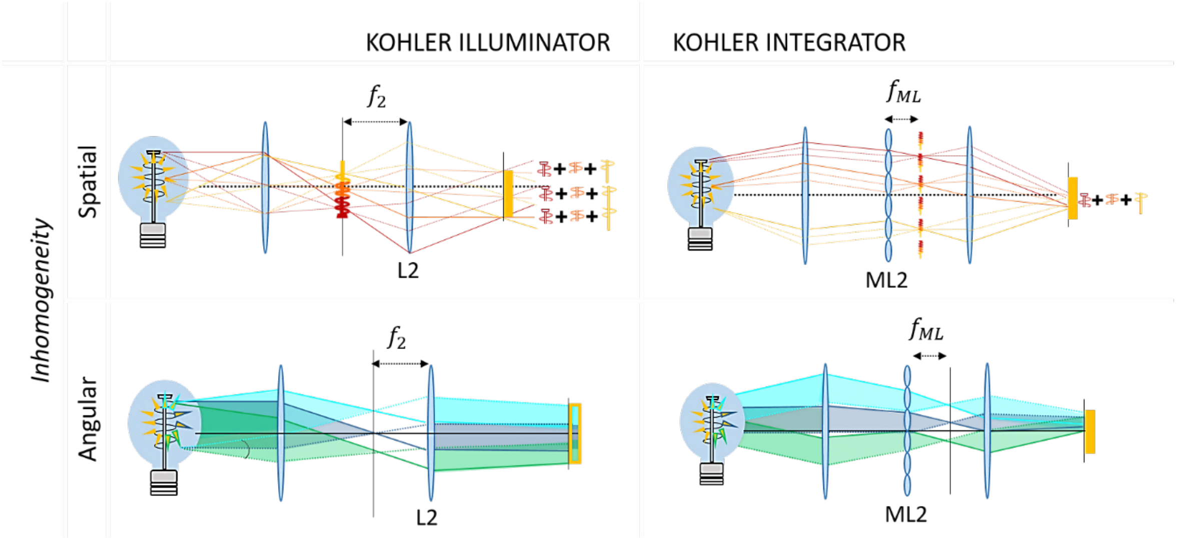

Figure 2-1 – A Kohler integrator. A Kohler integrator system provides a flat field and homogenous illumination independent of angular field and shape of the light source. A simple Köhler illumination system (left-top panel) illuminates each point at the target area with every emitter point at different positions across the source so that the spatial irradiance variations across the source are averaged out at the target illumination. However, this simple configuration cannot account for intensity variations of light source that generates a high directed beam (left-bottom panel). In a Köhler integrator, the light from the source is collected by an array of lenses to account for both angular and spatial inhomogeneity.

As shown in Figure 2-1, a simple Köhler illumination can only average out the irradiance spatial variations by overlapping an image of each light source point at each point of the target illumination area. This is achieved by simply focusing the light at the back focal aperture of the imaging objective.

However, in the presence of high directional source, which emits a stronger signal at a certain angle acceptance compared to another angle range (such as lasers used in SMLM imaging), a simple Köhler illumination will project every angle range always at the same position producing a spatial irradiance inhomogeneity.

A micro-lens-array-based (MLA) Köhler integrator addresses this problem by using a micro-lens-array comprised of lenses placed at different positions around the optical axis, with each collecting ray bundles coming out from the source at different angles. The rays coming out from the source at different angles will therefore overlap at every point in the resulting illumination area, averaging out any angular dependence of the source. A system with two MLA (Figure 2-3 b), where the second MLA is placed at one focal length after the first, will further improve the illumination thanks to the lenslets in the second MLA which cancel the quadratic phase curvature imparted by the first MLA[71].

An alternative approach for achieving a so called 'top-hat' illumination profile has been demonstrated with both diffractive and refractive beam shaping elements[72–74]. Single low-cost refractive beam-shaping element are commercially available and can be easily placed in any PALM/STORM microscope.

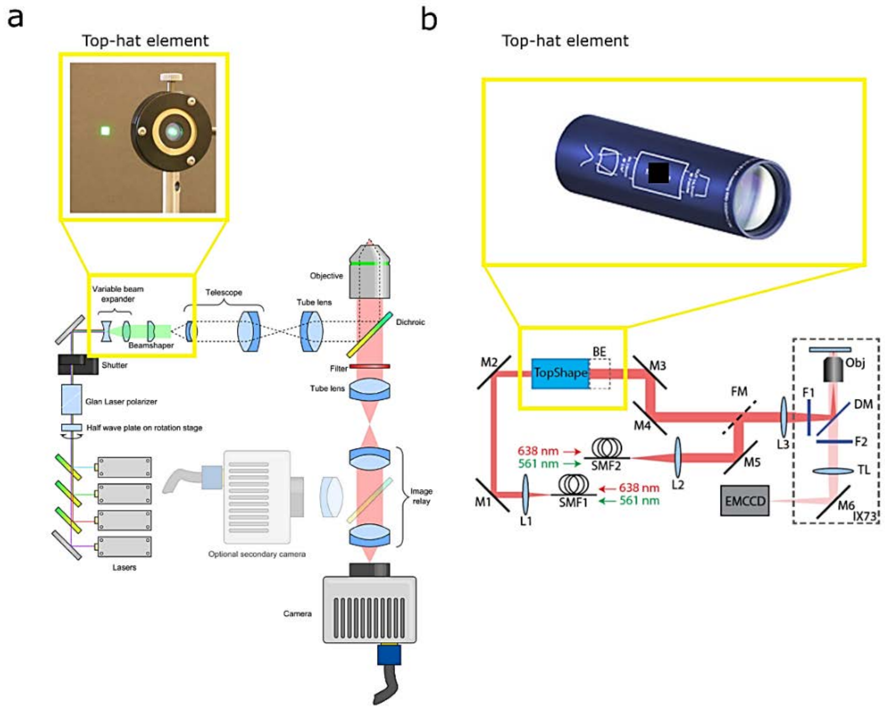
a
Top-hat element
Variable beam expander
Beamshaper
Telescope
Tube lens
Objective
Dichroic
Shutter
Filter
Tube lens
Glan Laser polarizer
Half wave plate on rotation stage
Image relay
Optional secondary camera
Lasers
Camera
b
Top-hat element
M2
TopShape
BE
M3
M4
FM
L3
F1
Obj
DM
F2
TL
638 nm
561 nm
SMF2
M5
L2
M1
L1
SMF1
638 nm
561 nm
EMCCD
M6
IX73

Figure 2-2 – Flat-field illumination employing beam shaper diffractive elements. a, The laser beams passing through the beam-shaper element emerges with a top-hat profile which is imaged onto the sample via a telescope and reflection off a dichroic mirror[73]. **b,** The laser beams are coupled into two single mode fibers. One output fiber beam is collimated and passes through the beam-shaper element producing a top-hat profile[74].

2.1.2 *Local speckles and interference fringes homogenization*

The free space excitation laser light along the optical path undergoes scattering and diffraction at the mirrors, lenses and coverslip surfaces. The production of mutually coherent sources, with different phase at every surface, generates interference fringes that vary with sample position and composition and with any optical component micro-position displacement. These unpredictable patterns produce non-uniformities in the sample illumination eventually giving rise to artifacts.

To degrade the spatial coherence of the beam and to reduce the illumination in-homogeneity a spinning diffuser is typically adopted[70,75] (Figure 2-3 a and b). However, this approach eliminates only the speckles and fringes due to imperfections in the optical system. To also remove the fringes arising from sample irregularities itself, the excitation beam should illuminate the sample from different directions. Radial scanning with an off-axis focused beam the back focal plane of the microscope objective, produces a collimated beam incident on the sample with a constant polar angle β (lower than 90°) and a rotating azimuthal angles (Figure 2-3 c). This solution can be implemented by using either an optic, such as galvomirrors, or a spinning wedge[76].

Another approach for achieving a homogenous excitation field employs optical multi-mode or single mode fiber. Single mode fiber generate a homogenous excitation field but with a global not-flat irradiance that requires an extra beam-shaper element for profile flattening[74] (Figure 2-3 d). On the other hand, multimode optical fibers generates a flat field with intensity fringes due to the modes interference. Mode scramblers are commercially available and they can be easily adopted[75,77] (Figure 2-3 e). However, the speckle-reducer results in significant loss of total laser power. An efficient mode scrambling can be achieved through a more sophisticated setup using either a multi-length optical fiber bundle[78] or a high-frequency vibration motor[79] (Figure 2-3 f). These methods are not limited by the speed of the wedge, mirror, diffuser or speckle-reducer and they do not involve the transmission through extra optical component and thus enabling low-power losses and high-speed imaging.

In the next Chapter, we will discuss which of these approaches can be compatible with a total internal reflection TIRF illumination and their limitations.

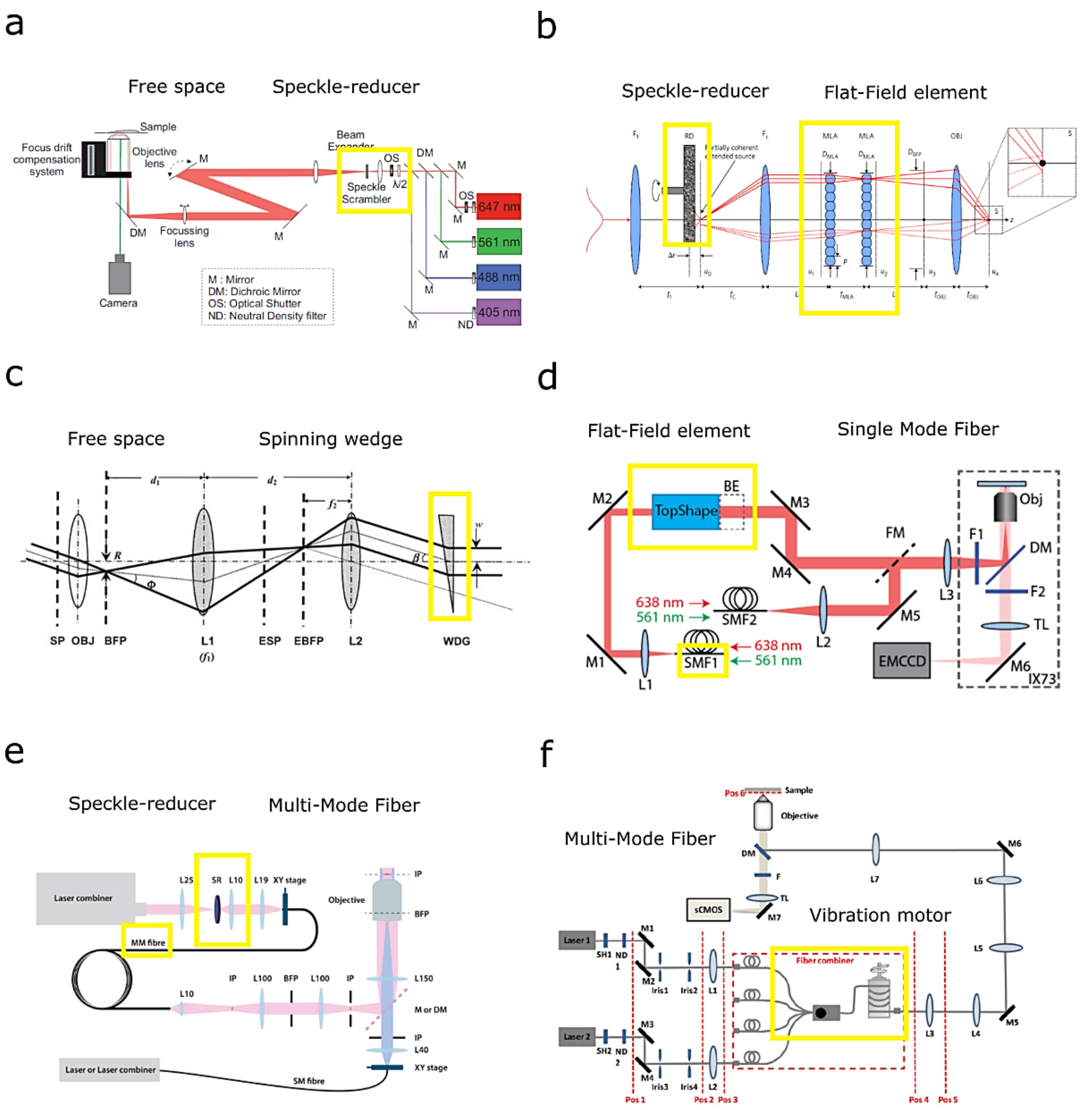
a
Free space
Speckle-reducer
Sample
Focus drift compensation system
Objective lens
M
Beam Expander
OS
DM
Speckle Scrambler
λ/2
647 nm
561 nm
488 nm
405 nm
DM
Focussing lens
Camera
M : Mirror
DM: Dichroic Mirror
OS: Optical Shutter
ND: Neutral Density filter
ND
b
Speckle-reducer
Flat-Field element
RD
MLA
MLA
OBJ
c
Free space
Spinning wedge
SP
OBJ
BFP
L1
ESP
EBFP
L2
WDG
d
Flat-Field element
Single Mode Fiber
M2
TopShape
BE
M3
Obj
FM
F1
DM
M4
L3
F2
638 nm
561 nm
SMF2
M5
TL
M1
L1
SMF1
638 nm
561 nm
L2
EMCCD
M6
IX73
e
Speckle-reducer
Multi-Mode Fiber
Laser combiner
L25
SR
L10
L19
XY stage
Objective
IP
BFP
MM fibre
L10
IP
L100
BFP
L100
IP
L150
M or DM
L40
XY stage
Laser or Laser combiner
SM fibre
f
Multi-Mode Fiber
Pos 6
Sample
Objective
DM
M6
F
L7
L6
sCMOS
TL
M7
Vibration motor
Laser 1
M1
SH1
ND 1
M2
Iris1
Iris2
L1
Fiber combiner
L5
Laser 2
M3
SH2
ND 2
M4
Iris3
Iris4
L2
L3
L4
M5
Pos 1
Pos 2
Pos 3
Pos 4
Pos 5

Figure 2-3 – Speckles and interference fringes homogenization approaches. . a and b, The spatial coherence of the beam can be degraded by introducing in the free space optical path a spinning diffuser that reduces the illumination in-homogeneity[70,75]. **a,** Scheme of the optical arrangement of a PALM/STORM apparatus build around an Olympus IX-71 inverted fluorescence microscope where a speckle scrambler is placed on the intermediate focal plane of a Keplerian beam expander[75]. **b,** The spinning diffuser element can be easily integrated in a Koehler integrator system and its position (Δr) determines the extended source size. f_1, f_c and f_{OBJ}, are the focal lengths of corresponding thin lenses; D_{MLA}, D_{BFP}, aperture sizes; MLAs micro-lens arrays with identical fical length f_{MLA}[70]. **c and d,** An uniform excitation can be produced by temporally and spatially varying the input beam using a spinning wedge or shaping the input beam with a diffractive optical element. Both these two approaches are compatible with a TIRF illumination because they do not degraded the coherence of the input beam that would make it hard to focus the beam at the back focal aperture of the objective. **c,** A spinning wedge diverts the beam into a hollow cone and the following lenses converge the collimated beam into a focused spot that traces a circle at the objective's back focal plane. When the wedge is spun rapidly, the different interference patterns are averaged out over a single camera exposure. SP, sample plane; OBJ, objective; BFP, back focal plane of the objective; L1, lens 1; ESP, equivalent sample plane as formed by L1; EBFP, equivalent back focal plane as formed by L1; L2, lens 2; WDG, spinning wedge[76]**.**

d, Imaging system was constructed with an Olympus IX73 inverted microscope where the laser sources were coupled into two single mode fibers. One output beam from a single-mode fiber was collimated with an achromatic lens and sent to the beam shaper (TopShape, asphericon GmbH).BE, 1.5x beam expander; DM, dichroic mirror; F1-2, excitation/emission filters; FM, flip mirror; L1-3, lenses; M1-6, mirrors; Obj, objective; SMF1-2, single mode fibers; TL, tube lens.[74]. **e, and f,** Multi-mode fibers are employed to achieved a flat field illumination in combination with a speckle reducer (e) and a vibration motor (f). **e,** Free-space propagating lasers are focused on the speckle-reducer before coupling into a multimode fiber. The fiber is coiled to further mix the laser modes. The image of the fiber output is then formed into the sample by relay lenses. The second optical path, is designed to perform standard TIRF illumination by focusing the light on the back-focal plane of the objective. Lxx: achromatic lens with focal length of xx mm, SR: speckle-reducer, MM: multimode, SM: single-mode, IP: image plane, BFP: back-focal plane, M: mirror and DM: dichroic mirror[77]. **f,** A uniform and flat field illumination is achieved by employing a multi-mode fiber combiner realized to reduce the speckle pattern contrast[79]. The optical setup for quantifying the illumination homogeneity at the sample plane. M1-M7: mirrors; Iris1-Iris4: Iris diaphragms; L1/L2: Fiber coupler with a focusing lens; L3: Microscope objective (10 × /NA0.25, Olympus); L4: Achromatic doublet lens; L5: Achromatic doublet; L6: Achromatic doublet lens; L7: Achromatic doublet lens; TL: Tube lens; Objective: Water-immersion microscope objective (60XW/NA1.2, Olympus); DM: Dichroic mirror; F: Emission filter.

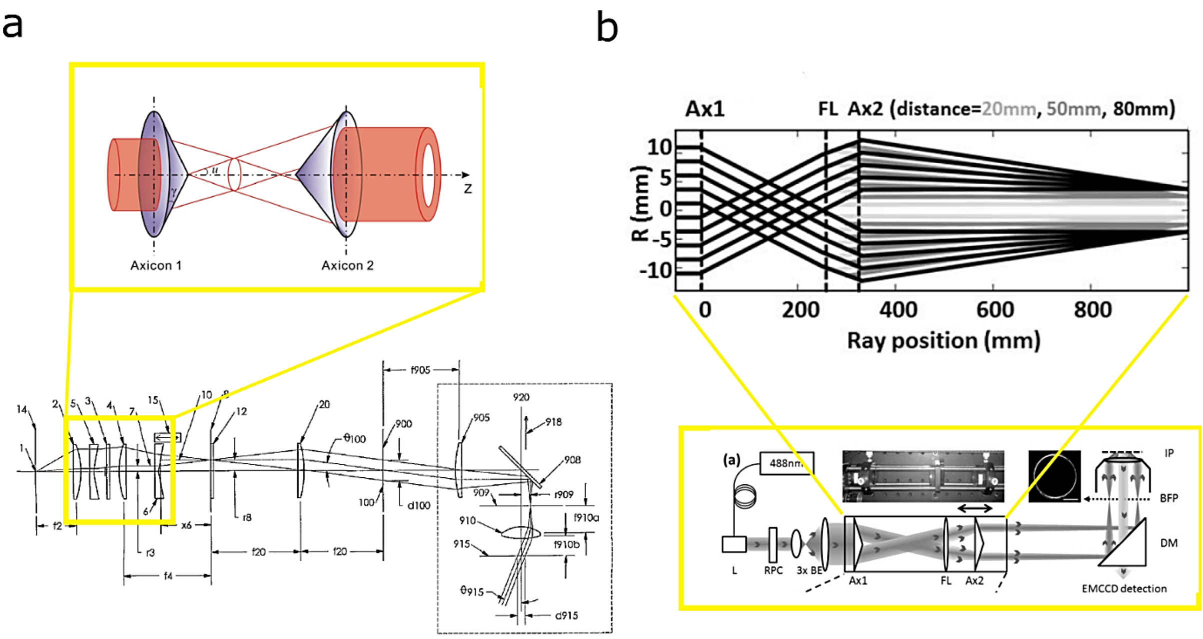

Figure 2-4 – Flat-field TIRF illumination using axicon lens. **a,** A collimated beam is generated by placing the light source (1) at the focal point of a lens-2 with focal length f2. A mask (3) is used to block the center portion of the beam that could produce scattering from the imperfection of the axicon lens center. Another lens (4) of focal length f4, focuses the light to a point in an image plane while the first stationary axicon lens (5) placed between these two lens (1 and 2) shifts the direction of the converging beam in a radial outward direction. The second axicon (6) shifts further outward the converging beam emerging from lens 2 and converging on the image plane (8) where it creates an annular illumination of a radius set by the distance x6 which increases linearly with x6. The disk of light is then collimated and relayed from the image plane (8) to the back pupil plane of the objective (909), by anther lens (20), the tube lens (905) and the objective (910). Figure taken from[80]. Magnified view of the axicon lens principle taken from [81]. **b,** Main optical components of another TIRF setup realized with two axicons (Ax1 and Ax2) lens, laser (L), radial polarization converter (RPC), beam expander (BE), focus lens (FL), and a dichroic mirror (DM). A disk of light is focused on the objective back focal (BFP) to produce a TIRF illumination at image plane (IP)[82].

2.2 Optical sectioning techniques

The quality of the imaging process does not depend only on the sample illumination uniformity. The viability of the biological sample is also crucial for obtaining meaningful and reliable biological results. Thus, many efforts have been done to find a strategy to minimize unnecessary dose of light delivery. A straightforward solution is to illuminate the sample target with a thin layer of light to avoid the excitation of the surrounding area. An optical sectioning approach has the advantage, not only to minimize the phototoxicity, but also to decrease the background and thus to improve the single molecule SNR.

Optical sectioning can be provided by light sheet[83], highly inclined and laminated optical sheet (HILO)[84], confocal rejection[85] or total internal reflection fluorescence (TIRF)[41]. However, confocal rejection also reduces the number of detected signal photons, while light sheet, HILO or objective TIRF are typically limited in both size and uniformity of illumination (Figure 2-5).

I previously described sophisticated setups using scanning of the coherent excitation light, such as the one based on a spinning wedge to rotate the beam[86,87] (Figure 2-3 c), to homogenize speckle pattern. These approaches are compatible with an objective-TIRF illumination and can reduce interference patterns, but they do not eliminate the spatial dependence of the field resulting from a focused Gaussian beam.

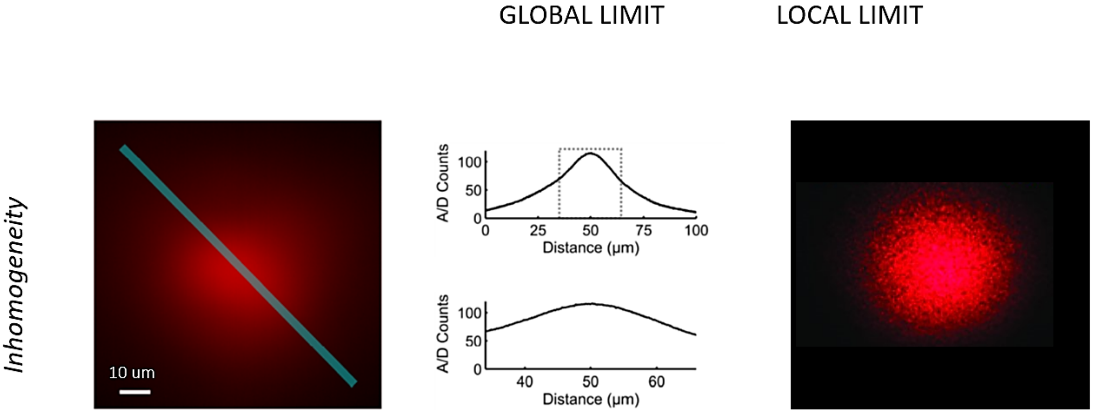

Figure from R. Diekmann, *Nat. Photonics*, 2017]

Figure from Cao, *Micromachines,* 2018]

Figure 2-5 – Objective TIRF limitations. Objective TIRF illumination suffers of global and local in homogeneities.

Another elegant approach is based on axicon lens[80,82,88] (Figure 2-4) to produce a small annular illumination at the objective back focal aperture suitable for objective-TIRF illumination and on a moving diffuser to spatially and temporally vary the excitation beam to eliminate the effects of laser speckle and interference fringes. This approach results in very low light loss compared to a much larger loss from the annular aperture and in a uniform TIRF illumination. However, the achievable field-of-view (FOV) is limited by the objective lens.

Other flat-field illumination methods that are easy to implement but not compatible with TIRF illumination are the previously described approaches based on multimode fiber combined with a speckle reducer[77,79,89] (Figure 2-3 b, e and f). In fact, they rely on the loss of the beam spatial coherence which prevents tight focusing of the beam at the back focal plane of the objective for TIRF illumination.

More recently, an effective flat-field objective-TIRF illumination has been proven by employing commercial beam shaper elements[74] (Figure 2-3 d). However, also this approach presents a limited uniformity and achievable field-of-view (FOV) size set by sample uniformity and the objective NA respectively.

A waveguide-TIRF approach provides a flat thin excitation field as large as the waveguide surface with an optical configuration that decouple the excitation light path from the detection path and thereby decreasing unwanted excitation light in the detection path and letting a free choice of the imaging objective.

In the next chapter, we will discuss when a light sheet or HILO illumination is more suitable and the main advantages and disadvantages of a waveguide TIRF approach.

2.2.1 *TIRF illumination*

Total internal reflection fluorescence (TIRF) microscopy relies on the evanescent field generated by the light that undergoes total internal reflection at the interface between coverslip and the sample[90]. The decay length d of the evanescent field intensity *I* sets the optical sectioning thickness and can be tuned by properly setting the incident beam angle θ, the beam wavelength λ and the difference ($n_{cs} - n_s$) between the sample holder (coverslip) and sample refractive indices:

$$I = I_0 e^{-z/d} \tag{2.1}$$

$$d = \frac{\lambda}{4\pi} \frac{1}{\sqrt{{n_{cs}}^2 \, sin^2\, \theta - {n_s}^2}} \tag{2.2}$$

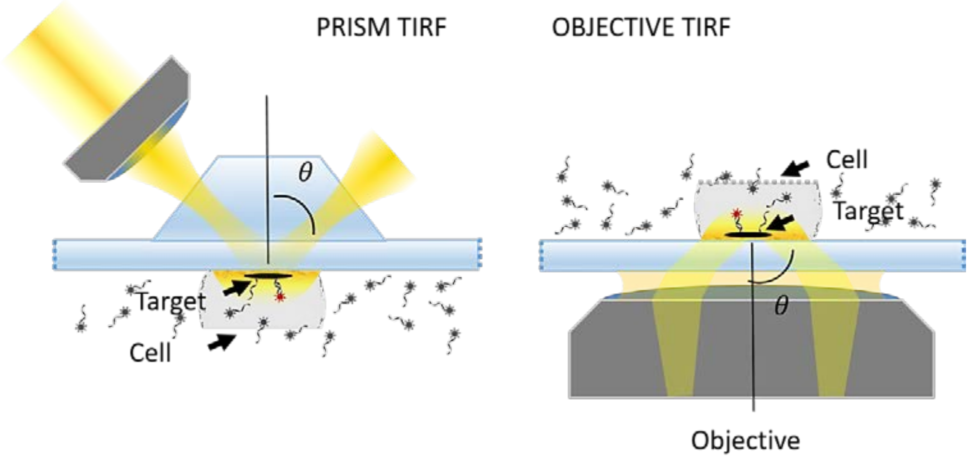

Figure 2-6 – Prism-TIRF and objective-TIRF configurations. Simplified sketch of the working TIRF principle for prism and objective TIRF approaches: the beam hits the sample-coverslip interface at an angle higher than the critical angle producing an evanescent field for sample excitation.

TIRF illumination typically generates a thin excitation field of about 200 nm just above the sample glass surface (Figure 2-6) making it suitable to efficiently detect, localize and track molecule events near the cell plasma membrane. Because of its uniquely thin selective illumination, only targeted fluorophores near the sample-glass interface are excited leading to less phototoxicity for the cell and higher signal to noise (2000 fold less background[91]) compared to standard wide field epi-illumination prone to out of focus fluorescence signal.

There are different configurations for producing a TIRF illumination commonly named objective-TIRF[90], prism-TIRF[91,92] and waveguide-TIRF[57] depending on the strategy used to produce the reflection of the excitation beam at the glass-aqueous solution interface. In a standard objective-TIRF approach, the same imaging lens is also used to cast an off-axis light beam such that it undergoes total internal reflection at the coverslip-sample interface. This ensures that only the resulting evanescent light field actually illuminates the target[93]. The optical constraints of such a configuration limit the size and uniformity of the sample illuminated area, and force the use of extremely high aperture lenses. While in the objective-TIRF and prism-TIRF configuration, the excitation beam is directly steered at an angle higher than the critical angle:

$$\theta_c = sin^{-1} \frac{n_s}{n_{cs}} \tag{2.3}$$

the waveguide-TIRF approach relies on the waveguide mode excitation to generate a continuum beam reflection all along the waveguide.

Although objective-TIRF is widely adopted due to its commercial availability and the easy switching between epi and TIRF mode, it limits the objective choice to high NA objectives and it is more prone to scattered unwanted light than the prism approach where the excitation and imaging paths are decoupled. Specifically, with a typical sample media and coverslip ($n_{cs} = 1.55, n_s = 1.38$) and with $\lambda = 647\ nm$ the critical angle is roughly $\theta_c \sim 66°$ thus the minimum required numerical aperture is about $NA = n_{cs} \sin \theta_{max} = 1.4$. Indeed, with such NA the maximum achievable angle is roughly $\theta_{max} \sim 73°$ and the maximum penetration depth d is roughly $d \sim 160\ nm$ at the critical angle $\theta_c \sim 66°$. Notice that with such a NA the available angle range for TIRF illumination is only of about 7°.

On the other hand, prism-TIRF is limited due to restricted access to the sample and the prism presence and it is not commercially available.

In a waveguide-TIRF approach, the evanescent field is generated by the light trapped in a shallow trench (waveguide core) characterized by a high refractive index with respect to the bottom cladding it lays within and the aqueous solution covering it. The light undergoes total internal reflection at the interface between the core and the aqueous solution, producing an optical sectioning illumination of the target of interest that lies at the waveguide surface (Figure 2-7).

The waveguide TIRF approach, compared with other flat field TIRF approaches such as refractive beam-shaping elements[73,74,79], introduces additional flexibility including the freedom to image with a low magnification objective[57] and the generation of an evanescent field with a uniform penetration depth[59,60], as well as built-in reference markings for correlative measurements. Even more important, the waveguide-TIRF approach can generate a uniform excitation field over an area as large as the entire waveguide surface.

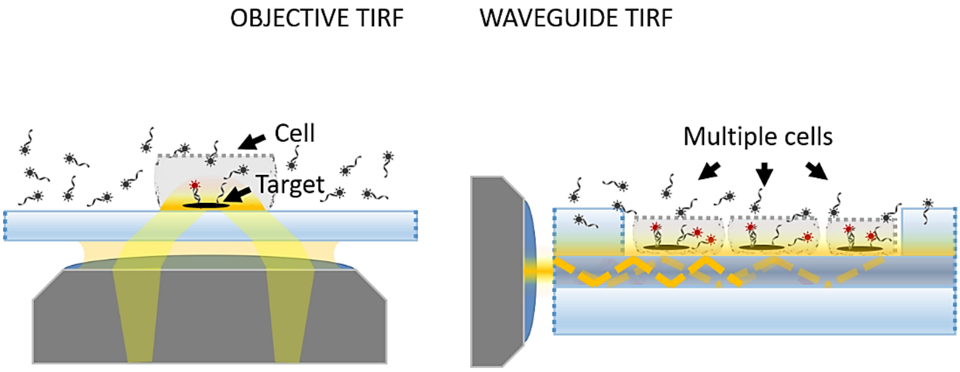

Figure 2-7 – Classical objective-TIRF and waveguide-TIRF approaches. With objective TIRF, the illumination field size is limited by the objective lens size and magnification and by a roll-off in intensity away from the central axis. In waveguide TIRF, the light (yellow) undergoes total internal reflection at the interface between the core and the aqueous solution, producing an optical sectioning illumination over the entire waveguide surface (up to 100 µm × 2000 µm in our chips).

Waveguide-TIRF excitation for fluorescence microscopy has previously been demonstrated with both low-refractive-index from polymethylmethacrylate (PMMA)[57] and high-index waveguide cores fabricated from either tantalum pentoxide (Ta_2O_5)[56,94] or silicon nitride (Si_3N_4)[60,95]. However, only High refractive Index Contrast (HIC)[59,60] waveguides-based TIRF platform have demonstrated imaging with a resolution beyond the diffraction limit (e.i. STORM)[60] and more in general they represents a compatible choice for fluorescence bio-imaging due to their chemical stability and their good transparency. HIC shows high confined mode field intensity and low propagation losses, yet the increased mode interaction at the interface produces a scattering loss enhancement where surface roughness is present[96,97]. Moreover, HIC waveguide light coupling suffers from high coupling losses, back-reflections and excitation of radiation modes due to both the mode-size and effective index mode mismatch and the input facet roughness[98–100]. Nevertheless, waveguide chip fabrication using Si_3N_4 processing is a convenient choice due to the maturity of the process and the know-how readily available within the Photonics Integrated Circuit (PIC) field, where low propagation losses has become a central requirements for on-chip waveguide[101–106].

2.2.2 *Light sheet illumination*

Although TIRF illumination can provide a straightforward and uniform optical sectioning illumination, this approach is limited to a region about 200 nm thick above the glass-coverslip surface.

Light-sheet microscopy has the potential of an optical sectioning at a much higher depth within the sample and with much higher thickness, and thus can be applied, for example, for imaging of the central nervous system, fish embryos or other tissues[107]. Although, light sheet was originally designed for low-magnification imaging involving an illumination volume much larger than a typical cell (such as COS7, HeLa, etc.), a thinner light sheet illumination combined with high numerical-aperture (NA) detection objective has been establish as valuable effective approach in SMLM.

Various implementations of light-sheet illumination have been proposed, such as highly inclined and laminated optical sheet (HILO)[84], inverted selective plane illumination microscopy (iSPIM)[108], individual molecule localization SPIM (IML-SPIM)[109], reflective light sheet microscopy (RLSM)[110], light-sheet Bayesian microscopy (LSBM) or prims-based SPIM[111]. These methods generate a PSF extended in the beam propagation direction and strongly flatten in the plane perpendicular to the propagation direction by collimating a Gaussian beam onto a cylindrical lens[83] or by using the diffraction of a beam entering the sample glass slide at high angles thorough an TIRF objective or a prism.

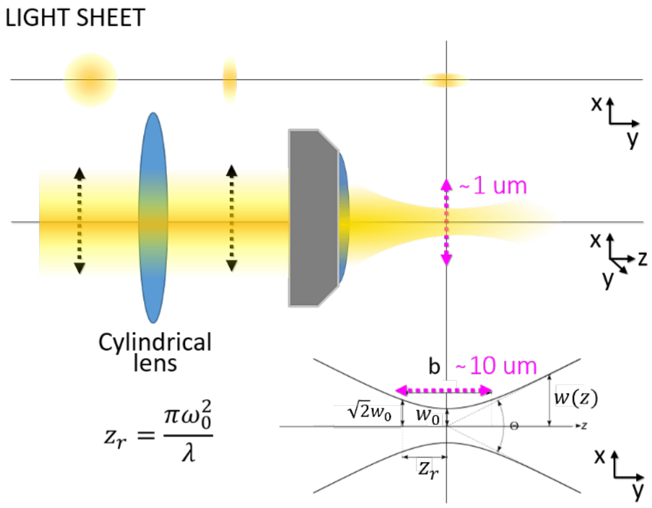

Figure 2-8 – Light sheet approach limits. Standard light sheet approach is limited in the FOV by the Rayleigh length and in thickness by the lens numerical aperture. Higher numerical aperture leads to a thinner light sheet but with faster divergence.

The main parameters describing the PSF of a focused Gaussian beam are the beam waist thickness w_0, which defines the light sheet minimum thickness ($2w_0$), and the Rayleigh range z_R, (the propagation length over which the beam intensity diverges less than $1/e^2$) which set the maximum imaging FOV size ($2z_R$) (Figure 2-8).

Laser beams propagating in free space can be described as pure transverse electric and magnetic fields almost perpendicular to the direction of propagation. In other words, their wave analysis can be derived as a deviation from a simple plane wave by assuming that the electrical field is of the form:

$$E(x, y\,, z) = E_0 \psi(x, y, z) e^{-ikz} \qquad 2.4$$

Here we assumed the field variation in the propagation direction (z) is a term of the approximate form e^{-ikz}, where $k = \frac{\omega n}{c} = \frac{2\pi}{\lambda}\frac{n}{c}$ and $\psi(x, y, z)$ represents how the beam deviates from a uniform plane wave. In free space, with neither charge nor current present, Maxwell's equation reduces to $\nabla \cdot E = 0$, substituting the previous expression in the time invariant wave equation $\nabla^2 E + \left(\frac{\omega n}{c}\right)^2 E = 0$, we obtain the central equation of the Gaussian beam [112] (Chapter 3):

$$\nabla^2 \psi - i2k\frac{\partial \psi}{\partial z} = 0 \qquad 2.5$$

Solving this equation in cylindrical coordinates leads to the final expression of the electrical field:

$$\begin{aligned} \frac{E(x, y, z)}{E_0} = \quad & \frac{w_0}{w} e^{-\frac{r^2}{w(z)^2}} && \mathit{amplitude} \\ \times \quad & e^{-i\left[kz - tan^{-1}\left(\frac{z}{z_0}\right)\right]} && \mathit{longitudinal\ factor} \\ \times \quad & e^{-i\frac{kr^2}{2R(z)}} && \mathit{radial\ factor} \end{aligned} \qquad 2.6$$

where

$$\begin{aligned} w(z)^2 &= w_0^2\left[1 + \left(\frac{z}{z_R}\right)^2\right] \\ R(z) &= z\left[1 + \left(\frac{z_R}{z}\right)^2\right] \\ z_R &= \frac{\pi {w_0}^2}{\lambda} \end{aligned} \qquad 2.7$$

The parameters w_0 and z_R can be easily extracted from the beam wavelength λ, the refractive index within the sample (n) and the NA of the excitation lens[107]:

$$2w_0 = 2\frac{n\lambda}{\pi NA} \qquad 2.8$$

$$2z_R = 2\frac{\pi {w_0}^2}{\lambda} = 2\frac{n^2\lambda}{\pi NA^2} = 1.7 \times FWHM \qquad 2.9$$

where the beam waist diameter w_0 is computed assuming a diffraction from a simple linear aperture or lens (Figure 2-9 a, top). In this case, the field distribution is described by the simple *sinc* function:

$$I(\vartheta) = I_0\left(\frac{sin\,\Phi}{\Phi}\right)^2 \qquad 2.10$$

where $\Phi = \frac{\pi D}{\lambda} \sin\vartheta$.

The resulting waist beam w_0, is then defined as the distance between the two first zero at the side of the central maximum. Thus, since $w \approx f \sin\vartheta = f\frac{\Phi\lambda}{\pi D}$ and the zero points of an unnormalized sinc function occurs for Φ equal to non-zero integer multiples of π,

$$I(\vartheta) = 0 \leftrightarrow \Phi = \frac{\pi D}{\lambda} sin\,\vartheta = m\pi \qquad \text{with}\, m \in \mathbb{Z} \tag{2.11}$$

the first zeros positions for $m = 1$ are at $w = \pm f\frac{\lambda}{\pi D}$ and thus:

$$2w_0 = 2\frac{\lambda f}{\pi D} = 2\frac{n\lambda}{\pi NA} \tag{2.12}$$

where *f* and *D* are the focal length and diameter of the lens.

A more accurate description of a focused beam assumes the presence of a circular aperture generating a diffraction pattern known as Airy disk or Fraunhofer diffraction pattern. The intensity profile is the squared modulus of the Fourier transform of the circular aperture (Figure 2-9 b):

$$I(\vartheta) = I_0\left(\frac{2J_1\Phi}{\Phi}\right)^2 \tag{2.13}$$

where the excitation field is now described by the more complex Bessel function J_1 and the resulting beam waist(Rayleigh limit) is computed from the first zeros of the order-one Bessel function:

$$2w_0 = 1.22\frac{\lambda}{NA} \tag{2.14}$$

The Gaussian approximating the Airy disk provides the relationship between the beam waist (corresponding to 1/e2 drop of intensity), the width and the full width at half maximum and the standard deviation of the Gaussian beam:

$$2w_0 = \frac{\sqrt{2}\,FWHM}{\sqrt{ln\,2}} = 1.7\,FWHM = 4 * \sigma_{PSF} \tag{2.15}$$

From the equations describing the beam waist diameter, we observe that by tightly focusing a Gaussian light sheet with high-NA objective, the resulting beam will diverge rapidly away from the focus reducing the maximum imaging FOV. Vice versa, low-NA lens generates a more extended PSF that increases the Rayleigh range of the excitation lens but with lower axial resolution.

Different approaches have been proposed to overcome the tradeoff between FOV size and axial resolution based on input Bessel beam[113] or Airy beam[114] instead of a Gaussian beam. Although Bessel beams are diffraction-limited like any other beam, they produce a light sheet with a flat profile over many times the Rayleigh range achieved with Gaussian input beam at the same illumination objective NA. However, Bessel beams generate side lobes and thus out-of-plane background that requires either structural illumination or multiphoton to be removed and Airy beam approach is limited to low NA imaging objective which is not compatible with SMLM approaches.

More recently, other methods achieved large FOV (over 50 µm)[115] and high axial resolution (about 450 nm) relying on sweeping a moderate-high NA Gaussian beam through the sample along the propagation axis rather than on beam shaping. However, their sweep process increases the total imaging time and presents a potential high photo-damage drawback.

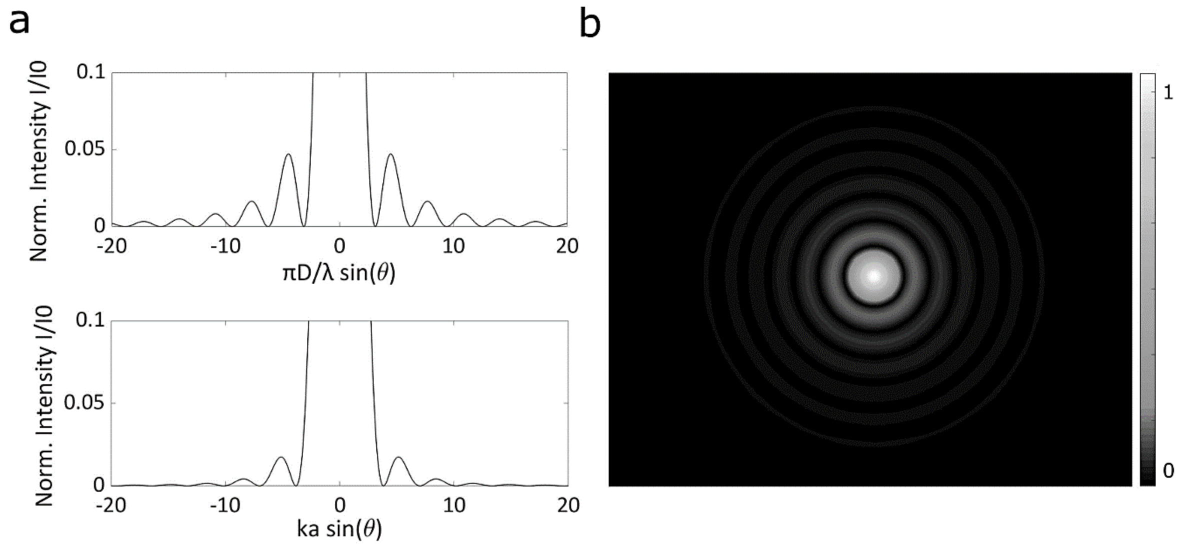

Figure 2-9 – Beam propagation from rectangular and circular aperture. **a,** Propagation from a rectangular and circular aperture can be described by a Sinc (top) and Bessel functions respectively (bottom); **b,** 2D diffraction from circular aperture is simulated using beam propagation theory: the far field of the plane wave crossing the aperture is the Fourier transform of the aperture.

To sum up, light sheet achieves axial resolution higher than the one achieved by simple wide field or confocal-like approaches. Indeed, the axial resolution of the light sheet is defined by the waist of the excitation beam rather than the larger Rayleigh range which depends on the square of the NA providing a more selective z range choice^{116}.

A summary of the main advantages and disadvantages of the different optical sectioning approaches is reported in Table 2-1.

	Im-Obj. limited to	**Maximum LS Depth [nm]**	**Minimum LS Thickness [nm]**	**Max. FOV @min. thickness limited by**	**Field axial uniformity limited by**	**Solution for intrinsic fringes -speckles**	**Axial scanning done through**
OBJ-TIRF	High NA > 1.46	~200 nm depends on Δn	~200 nm depends on Δn	NA	Input beam profile	- Temporal averaging of the scanned input beam - Single mode fiber design	Shift position of beam at the BFA of the Im. Obj.
WG-TIRF	-	~200 nm	<100 nm	-	Flat	As OBJ-TIRF	-
HILO[84]	High NA > 1.46	~ few µm	Diffracted limited	NA	Input beam profile	As OBJ-TIRF	As OBJ-TIRF
SPIM	-	>200 µm	Limited by w_0 ~ 1 µm	z_R <10 µm	Input beam profile and ill. Obj. NA	- Temporal averaging of the scanned input beam	Moving the sample stage or the input beam at the BFA of the Im. Obj.
Inverted SPIM *iSPIM*[108]	As SPIM	As SPIM	As SPIM proved up to beam thickness w_0 ~ 1 µm	As SPIM	As SPIM	- Input beam scanning producing a rotation at the imaging plane	Galva mirror at the BFA of the Im. Obj.
3D astigmatic SMLM SPIM *IML-SPIM*[109]	-	Proved up to ~100 µm	As SPIM but SM axial resolution ~100 nm proved with a few µm thick light sheet at ~100 µm depth	Proved up to z_R < 50 µm over	Input beam profile and ill. obj. NA	As SPIM	Sample stage
RLSM[110]	-	Proved up to ~10 µm	Limited by w_0 ~ 1 µm	z_R <10 µm	Illumination obj. NA	As SPIM	AFM cantilever
Prism Bayesian SPIM *LSBM*[111]	-	Proved up to ~10 µm	As SPIM. Proved down to beam thickness w_0 ~ 1 µm	Proved up to z_R <15 µm	Input beam profile and ill. obj. NA	As SPIM	Changing input beam angle at the prism-sample interference
Bessel-SPIM[113]	-	Proved up to ~50 µm	Proved down to ~0.3 µm	Proved up to z_R <15 µm	Bessel beam lateral lobes suppressed via SIM or two photon excitation	As SPIM	z-axis galvanometer

Table 2-1 Light-sheet microscopy methods compatible with SMLM. The table presents a comparison between optical sectioning maximum depth, thickness, field of view (FOV), uniformity, resolution and axial scanning approach achieved with different optical sectioning approaches (SPIM). Ill-Obj. illumination Objective; Im-Obj. imaging Objective; LS, light sheet; Obj. Objective, Obj-TIRF Objective TIRF; WG-TIRF waveguide TIRF; BFA back focal aperture; Δn refractive index difference between coverslip and sample; SIM structured illumination microscopy.

2.3 Single molecule localization precision

The quality of super-resolution images obtained by single-molecule localization microscopy are strictly related to the software used to detect and localize the signal spikes[117].

A standard way to access the molecule position (θ_x, θ_y) and other set of parameters describing the molecule signal distribution (e.g. maximum amplitude θ_N, variance ${\theta_\sigma}^2$, background θ_b) is based on a two-dimensional (2D) Gaussian (plus a constant background) interpretation of the PSF followed by a least-squares (LS) fitting:

$$\chi(\boldsymbol{\theta}, \mathbb{D}) = \sum_{x,y \in \mathbb{D}} \frac{1}{\sigma_{x,y}^2} (I(x,y) - PSF(x,y \mid \boldsymbol{\theta}))^2 \qquad 2.16$$

$$\widehat{\boldsymbol{\theta}} = \underset{\boldsymbol{\theta}}{\arg\min} \sum_{x,y \in \mathbb{D}} \frac{1}{\sigma_{x,y}^2} (I(x,y) - PSF(x,y \mid \boldsymbol{\theta}))^2 \qquad 2.17$$

where $\sigma_{x,y}$ accounts for the uncertainty in the number of detected photons, $I(x,y)$ is the detected image intensity and

$$PSF(x,y \mid \boldsymbol{\theta}) = \frac{\theta_N}{2\pi{\theta_\sigma}^2} e^{-\frac{(x-\theta_x)^2+(x-\theta_x)^2}{2{\theta_\sigma}^2}} + \theta_b \qquad 2.18$$

However, it has been shown that maximum likelihood based algorithms can produce more accurate results than a least squares approach specifically in the presence of Poisson distributed data with low signal levels[118,119].

A maximum likelihood estimator (MLE) provides parameter estimates by finding the parameter values that maximize the likelihood function. Such an estimator has a precision defined by the Cramér-Rao-Lower-Bound (CRLB) that is at least as high as the inverse of the Fisher information $I_{ii}(\theta)$. Indeed, each parameter θ_i can be estimated with a maximum precision given by the diagonal elements of the matrix inversion $I_{ii}(\theta)$ [120]:

$$\sigma_{CRLB}(\theta_i) = \frac{1}{I_{ii}(\theta)} = \frac{1}{-E[\ln \mathcal{L}(\boldsymbol{\theta}, \mathbb{D})'']} \qquad 2.19$$

where with $E[\ln \mathcal{L}(\boldsymbol{\theta}, \mathbb{D})'']$ we donated the expected value of the second derivative of the log-likelihood function.

The CRLB of any parameter of the PSF of an isolated molecule digitally imaged (here assumed with a classical Airy profile) is thus set by[121,122]:

$$\Delta\theta \geq \sigma_{CRLB}^{EMCCD} = \frac{\sqrt{2}}{\sqrt{N}\sqrt{i(\theta)}} \qquad 2.20$$

where N is the number of photons in the image, and θ any PSF parameter (e.g. the position coordinate), $i(\theta)$ is the information content of a single photon and is calculated from the PSF and the factor $\sqrt{2}$ is included to account for the excess noise of an electron-multiplying charge-coupled device (EMCCD) camera[123].

The variance of single molecule localization estimate computed with estimator that account for noise sources of noise and the finite pixel area, is then given by [121]:

$$\sigma^2(\theta_x) = \sqrt{\sigma^2(\mu_x)} = \sqrt{\frac{\sigma_a^2}{N}\left(\frac{16}{9} + \frac{8\pi\sigma_a^2 b^2}{Na^2}\right)} \sim \sigma_{PSF}/\sqrt{N} \qquad 2.21$$

where the EMCCD camera noise has been taken into account, a^2 is the pixel area, b^2 is assumed background expected noise per pixel and $\sigma_a^2 = {\sigma_{PSF}}^2 + \frac{a^2}{12}$ and *N* the number of photons collected. This variance estimate differs from eq. 1.4 because it accounts systematically for the dependence on finite pixel area as well for the main source of noise. Indeed, equation 1.4 neglects the a^2-dependence of the term proportional to b^2 and the factor 16/9 (Supplementary Note of [121]).

Equation 2.21 underlines other important factors affecting the localization precision: the photon collection efficiency of the system (included the objective NA and detection Q.E.) and the back-projected camera pixel size – i.e. by the pixel size and the objective magnification. It is worth noting that by decreasing the pixel size, we reduce the pixilation effect and thus we increase the signal spatial sampling. However, this process does not lead to a continuous increase in the localization precision. Indeed, the pixel size reduction decreases also the number of detected photons in each pixel, whereas the measurement noise remains the same. Typically, the best pixel size is about (Figure 2-10)[11]:

$$a^4 \sim \sigma_{PSF}^4 \frac{100\pi b^2}{N} \qquad \xrightarrow[\substack{b\sim1 \\ N\sim100}]{} \qquad a \sim 1.3 \cdot \sigma_{PSF} \qquad 2.22$$

A Least Square fitting approach identifies the best parameter estimates by defining an analytical function (in our case just a simple 2D Gaussian function) and by searching for the set of parameters, which minimizes the sum of the squared weighted errors. Instead, a MLE maximizes the probability that a parameter set describes our data as better as possible.

We assume that the dominant noise of the image pixels is the shot noise – thus assuming that the number of photons hitting over time the camera pixels follow independent Poisson distributions:

$$\mathcal{P}(k,\lambda) = \frac{\lambda^k e^{-\lambda}}{k!} \qquad 2.23$$

$$\text{where} \qquad \begin{aligned} \lambda &= PSF(x,y,\boldsymbol{\theta}) \\ k &= I(x,y) \end{aligned} \qquad 2.24$$

Moreover, we account for the finite size of the detector pixel[124]:

$$PSF(x,y \mid \boldsymbol{\theta}) = \frac{\theta_N}{2\pi{\theta_\sigma}^2}\int_{A_p} e^{-\frac{(u-\theta_x)^2+(v-\theta_x)^2}{2{\theta_\sigma}^2}}\, dudv + \theta_b \qquad 2.25$$

which includes the PSF integration over finite pixels, which is the integral over the finite area A_p of the *p*th pixel, which is centered at (x,y).
Then, the likelihood function $\mathcal{L}(\boldsymbol{\theta},\mathbb{D})$ from which to extract the best parameter estimate $\widehat{\boldsymbol{\theta}}$ becomes:

$$\mathcal{L}(\boldsymbol{\theta},\mathbb{D}) = \prod_{x,y\,\in\,\mathbb{D}} \frac{PSF(x,y \mid \boldsymbol{\theta})^{I(x,y)} e^{-PSF(x,y \mid \boldsymbol{\theta})}}{I(x,y)!} \qquad 2.26$$

$$\begin{aligned}\widehat{\boldsymbol{\theta}} &= \underset{\boldsymbol{\theta}}{\arg\max}[\ln \mathcal{L}(\boldsymbol{\theta}, \mathbb{D})] \\ &= \underset{\boldsymbol{\theta}}{\arg\max} \sum_{x,y \in \mathbb{D}} I(x,y) \ln PSF(x,y \mid \boldsymbol{\theta}) - PSF(x,y \mid \boldsymbol{\theta})\end{aligned} \qquad 2.27$$

The Fisher information matrix is defined as [120]:

$$I_{ij}(\theta) = \mathrm{E}\left[\frac{\partial \mathcal{L}(\boldsymbol{\theta}, \mathbb{D})}{\partial \theta_i} \frac{\partial \mathcal{L}(\boldsymbol{\theta}, \mathbb{D})}{\partial \theta_j}\right] \qquad 2.28$$

Using eq. 2.26, eq. 2.28 and the Stirling approximation ($\ln n! \sim n \ln n - n$), the Fisher information becomes:

$$\begin{aligned} &I_{ij}(\theta) = \\ &= \mathrm{E}\left[\sum_{x,y \in \mathbb{D}} (I(x,y) - PSF(x,y \mid \boldsymbol{\theta}))^2 \frac{1}{PSF(x,y \mid \boldsymbol{\theta})^2} \frac{\partial PSF(x,y \mid \boldsymbol{\theta})}{\partial \theta_i} \frac{\partial PSF(x,y \mid \boldsymbol{\theta})}{\partial \theta_j}\right]\end{aligned} \qquad 2.29$$

Since we are assuming the data are described by Poisson process, the variance of the process $(I(x,y) - PSF(x,y \mid \boldsymbol{\theta}))^2$ is equal to the expected value λ of the process (see eq. 2.24), and since the expected operator is a linear operator ($E(X+Y) = E(X) + E(Y)$), $I_{ij}(\theta)$ becomes:

$$I_{ij}(\theta) = \sum_{x,y \in \mathbb{D}} \frac{1}{PSF(x,y \mid \boldsymbol{\theta})} \frac{\partial PSF(x,y \mid \boldsymbol{\theta})}{\partial \theta_i} \frac{\partial PSF(x,y \mid \boldsymbol{\theta})}{\partial \theta_j} \qquad 2.30$$

Deriving eq. 2.25 we obtain:

$$\begin{aligned} \frac{\partial PSF(x,y \mid \boldsymbol{\theta})}{\partial \theta_x} &= \frac{\theta_N}{2\pi {\theta_\sigma}^2} \int_{A_p} (\theta_x - u) e^{-\frac{(u-\theta_x)^2 + (v-\theta_x)^2}{2{\theta_\sigma}^2}} dudv \\ \frac{\partial PSF(x,y \mid \boldsymbol{\theta})}{\partial \theta_y} &= \frac{\theta_N}{2\pi {\theta_\sigma}^2} \int_{A_p} (\theta_x - u) e^{-\frac{(u-\theta_x)^2 + (v-\theta_x)^2}{2{\theta_\sigma}^2}} dudv \\ \frac{\partial PSF(x,y \mid \boldsymbol{\theta})}{\partial \theta_N} &= \frac{1}{2\pi {\theta_\sigma}^2} \int_{A_p} e^{-\frac{(u-\theta_x)^2 + (v-\theta_x)^2}{2{\theta_\sigma}^2}} dudv \end{aligned} \qquad 2.31$$

Expressing the Gaussian function in term of the error function *erf*:

$$PSF(x,y \mid \boldsymbol{\theta}) = \theta_N \Delta E_x(x,y) \Delta E_x(x,y) + \theta_b \qquad 2.32$$

where

$$\Delta E_x(x,y) = \frac{1}{2}\mathrm{erf}\left(\frac{x - \theta_x + \frac{1}{2}}{2{\theta_\sigma}^2}\right) - \frac{1}{2}\mathrm{erf}\left(\frac{x - \theta_x - \frac{1}{2}}{2{\theta_\sigma}^2}\right) \qquad 2.33$$

$$\Delta E_y(x,y) = \frac{1}{2}\mathrm{erf}\left(\frac{x - \theta_y + \frac{1}{2}}{2{\theta_\sigma}^2}\right) - \frac{1}{2}\mathrm{erf}\left(\frac{x - \theta_y - \frac{1}{2}}{2{\theta_\sigma}^2}\right)$$

then, the integration of eq. 2.31 gives[124]:

$$\frac{\partial PSF(x,y\,|\,\boldsymbol{\theta})}{\partial\theta_x}=\frac{\theta_N}{\sqrt{2\pi}\theta_\sigma}\left(e^{-\frac{\left(x-\theta_x-\frac{1}{2}\right)^2}{2\theta_\sigma{}^2}}-e^{-\frac{\left(x-\theta_x+\frac{1}{2}\right)^2}{2\theta_\sigma{}^2}}\right)\Delta E_y(x,y)$$

$$\frac{\partial PSF(x,y\,|\,\boldsymbol{\theta})}{\partial y}=\frac{\theta_N}{\sqrt{2\pi}\theta_\sigma}\left(e^{-\frac{\left(y-\theta_y-\frac{1}{2}\right)^2}{2\theta_\sigma{}^2}}-e^{-\frac{\left(y-\theta_y+\frac{1}{2}\right)^2}{2\theta_\sigma{}^2}}\right)\Delta E_x(x,y) \qquad 2.34$$

$$\frac{\partial PSF(x,y\,|\,\boldsymbol{\theta})}{\partial\theta_N}=\Delta E_x(x,y)\Delta E_y(x,y)$$

It is worth to noticed that, when the number of photons per molecule increases, the process starts approaching a normal random process and the likelihood function becomes:

$$\mathcal{L}(\boldsymbol{\theta},\mathbb{D})=\prod_{x,y\,\in\,\mathbb{D}}\frac{1}{2\pi\sigma_{x,y}^2}e^{-\frac{(I(x,y)-PSF(x,y\,|\,\boldsymbol{\theta}))^2}{2\theta_\sigma{}^2}} \qquad 2.35$$

In the presence of pixels with almost equal signal variances $\sigma_{x,y}^2$, the maximization of the likelihood function then reduces to a LS minimization problem:

$$\begin{aligned}\widehat{\boldsymbol{\theta}}&=\underset{\boldsymbol{\theta}}{\arg\max}[\ln\mathcal{L}(\boldsymbol{\theta},\mathbb{D})]\\&=\underset{\boldsymbol{\theta}}{\arg\min}\sum_{x,y\in\mathbb{D}}\frac{1}{\sigma_{x,y}^2}(I(x,y)-PSF(x,y\,|\,\boldsymbol{\theta}))^2\end{aligned}$$

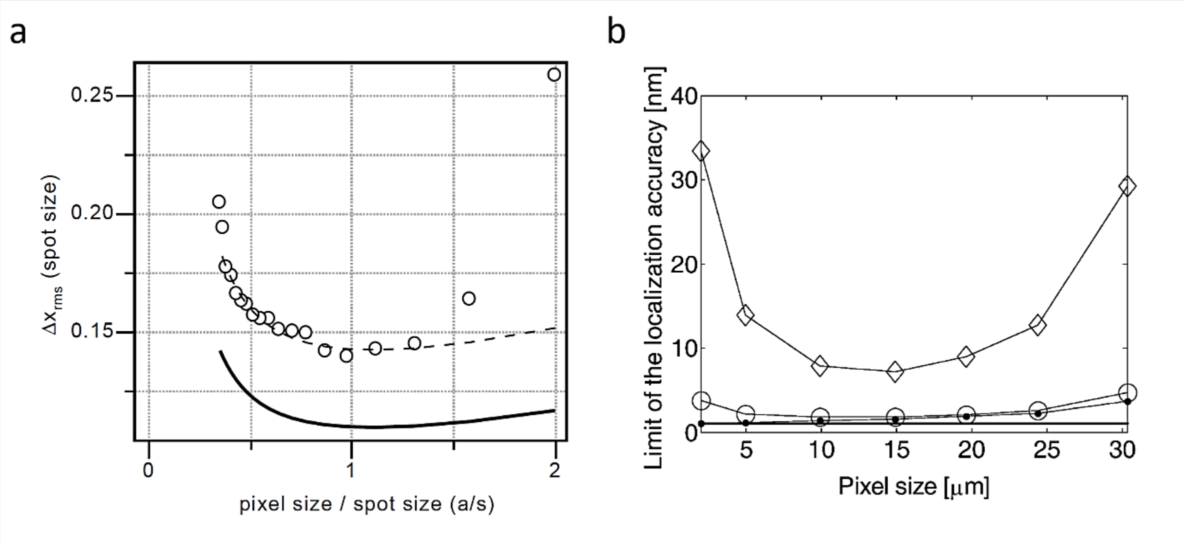

Figure 2-10 – Dependence of the localization accuracy on the pixel size. a, The localization uncertainty Δx_{rms} (expressed in PSF-size σ_{PSF} unit) increases at small pixel sizes due to increased background noise weight and for large pixel sizes due to the lower sampling rate. The theoretical prediction given by Thompson's equation 1.4 (solid line) shows that results from computer-generated images (circles) are offset from the theoretical prediction by 30% (dashed line) do to the neglected dependence on finite pixel area as well for the main source of noise. However, the position of the minimum of the curve, is accurately predicted at $(a/\sigma_{PSF})^4 = 100\,\pi\,b^2/N$. Figure taken from[11]. **b,** Limit of the localization accuracy of the x-coordinate of a single molecule as a function of pixel size (not divided by the magnification) for a pixelated detector in the presence of measurement noise. Empty diamond and circle correspond to different readout noise levels (57 e-/pixel and 7 e-/pixel respectively). Filled circle correspond to localization precision limit in the absence of noise. Figure taken from [122].

2.3.1 *3D SMLM DH-PSF localization algorithms*

In the last decade, many algorithms have been implemented to obtain a 3D SM super-resolved image based on DH-PSF raw data (Figure 2-11). A crucial aspect for the final image reconstruction and resolution is the accuracy of the localization algorithm. The localization can be easily based on simple geometrical interpretation of the DH-PSF (e.g. 2D Gaussian least square (LS) based fitting[125], centroid, rotation angle). Alternative fitting approaches, such as cubic splines accurately capture the shape of any PSF[126,127] or are based on 3D phase retrieval (PR)[128–130]. Methods based on the approximation of the DH-PSF as two rotating 2D-gaussians are computationally faster but they are suboptimal because they may not accurately capture the PSF or lack specific noise statistics[33,124].

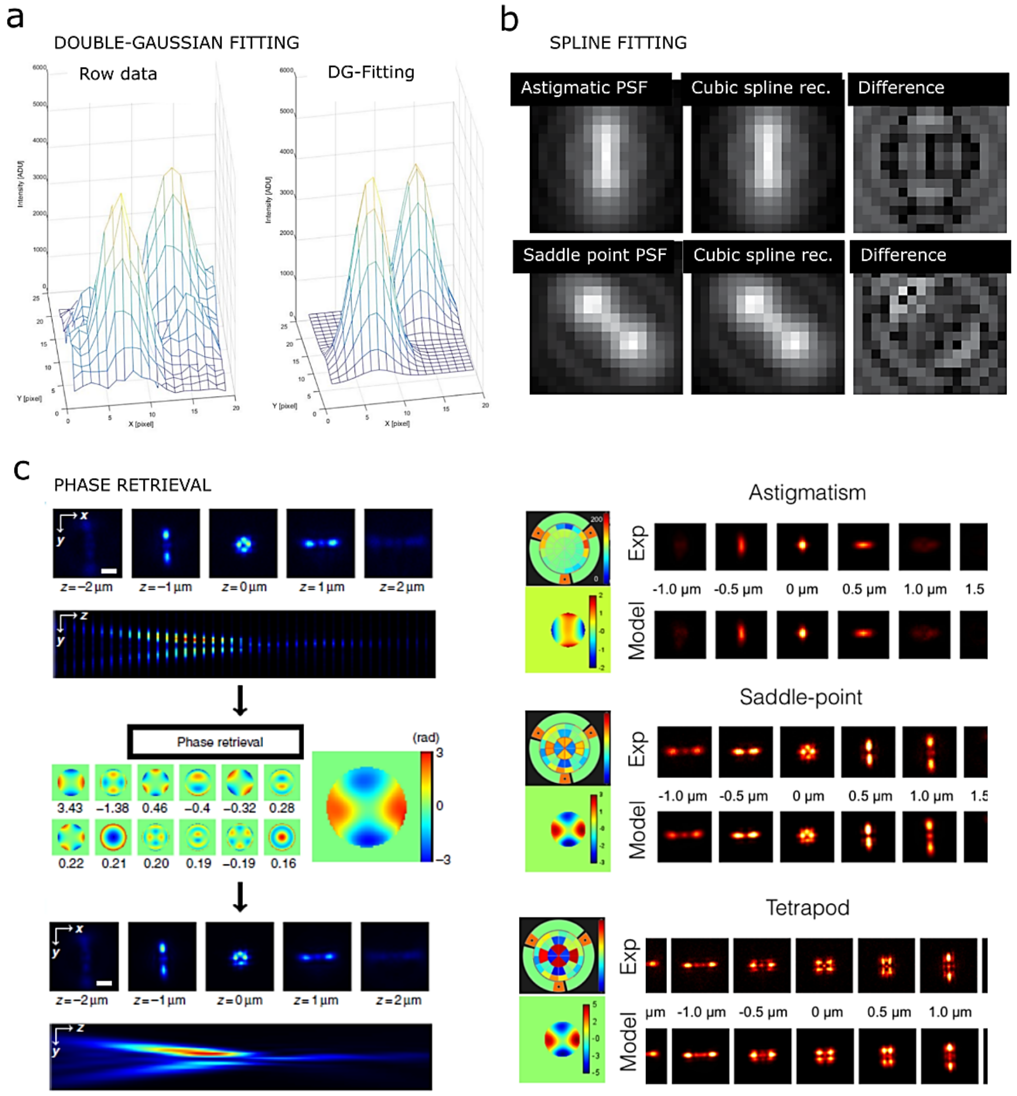

Figure 2-11 – DH-SMLM algorithms. a, Typical 2-Gaussian analytical fitting of the DH-PSF.; **b,** Spline PSFs reconstruction of an astigmatic and saddle PSFs[127]; **c,** Left ZOLA phase retrieval approach[128]. PSF calibration from bead images taken over an axial range of 4 µm, with Δz = 100 nm steps. Scale bars, 1 µm. ZOLA uses these images to compute a maximum likelihood estimation of the phase as a linear combination of Zernike polynomials to accurately reconstruct the SMs PSFs from the retrieved phase; **c,** Right, Experimental and model PSFs obtained for three different experimental settings. The top row ("Exp.") shows a z-stack of a fluorescent bead, i.e. an approximation of the experimental PSF. The bottom left panel shows the phase model retrieved by ZOLA, in radians. The bottom row ("Model") shows a z-stack of the model PSF[128]**.**

Cubic splines — through the *CSpline* algorithm – represent an excellent approach to precisely capture the PSF shape by lowering the computational coast of the phase-retrieved pupil functions. However this method, for a single point estimation, still requires 128 operations for a single point estimation, as compared to 10 operations to evaluate the elliptical Gaussian[131].

A further aspect that affects the localization algorithm accuracy, is the ability to recognize SMs spatial and temporal overlap and to perform a multi-emitter evaluation. This aspect it is particularly crucial for engineered PSF where the large axial range comes at the expense of larger lateral extent and thus increasing PSF overlapping from nearby molecules (see Figure 1-4).

Yet, the implementation of an efficient, fast and easy to use double-helix multi-emitter approach is not available yet. Therefore, we aimed to develop a fast and precise multi-emitter DH-PSF localization maximum-likelihood estimator (MLE) algorithm. To minimize its computation cost, we would base it on simple analytical fitting of a double Gaussian while increasing its accuracy accounting for different sources of noise (camera noise and molecule signal shot noise).

To guide researchers on the choice of the most suitable localization software for their experiments, a large community effort has be done in the context of a 3D SMLM Challenge competition. This provided an extensive characterization and ranking of the available packages against realistic simulated datasets for popular imaging modalities – 2D, astigmatic 3D, biplane 3D, and double helix 3D[39] (Figure 2-12). To provide standard test data or metrics, the simulated dataset were generated from experimentally acquired point spread functions with signal and noise levels based closely on common experimental conditions and including a 4-state model of fluorophore photophysics[132].

The main metric used to evaluate the software localization quality were following:

- the lateral and axial root mean square error (RMSE [nm]),
- recall $\left(\frac{TP}{TP+FN}\right)$ [%], precision $\left(\frac{TP}{TP+FP}\right)$ [%] and
- Jaccard index – $JAC = \left(\frac{TP}{TP+FN+FP}\right)$ [%], which simultaneously conveys the recall and precision metrics where: TP are the true positive, the number of paired activations, *FP* the false positive (*FP*), the number of unpaired estimated activations, and FN the false negative (FN), the number of unpaired true activations.

The 2016 Challenge Results show that the double helix software present more uniform performance than astigmatism-based ones on high SNR low spot density condition. The best-in-class DH software, SMAP-2018, uses a single emitter spline fitting of an analytical function to the experimental PSF. SMAP-2018 exhibits a limited improvement compared with average software (lateral RMSE is equal to 27 nm for the best and 37 nm on average; axial RMSE is 21 nm for the best and 34 nm on average; the Jaccard index 77 % best vs 73 % average)[39]. On high SNR low spot density, DH-PSF imaging may affect less the software-to-software variation than astigmatic imaging because the DH-PSF shape and intensity are fairly constant as a function of Z. In astigmatic imaging, on the other hand, spot size, shape and intensity vary greatly as a function of Z [39].

For DH-PSF dataset, in general software localization performance was close to the Cramér-Rao lower bound and relatively uniform even far from the focal plane[39]. Double helix software performance decreased significantly for low SNR condition and for high spot density, particularly in terms of best-in-class Jaccard index. The poor performance at high spot density is probably due to the large DH PSF width that statistically produces more easily PSF overlapping and thus lower SNR. The best-in-class-DH-PSF software also performed poorly on the high spot density datasets at high SNR (best software CSpline which uses multi-emitter spline fitting)[39].

Interestingly, top performers software uses temporal grouping of molecules detected multiple times in adjacent frames, and average their position. This is a common post-processing approach to improve localization precision[133].

Although CMOS cameras have recently been widely adopted in SMLM, the 2016 3D SMLM Challenge did not include CMOS specific simulated dataset - only dataset with typical EMCCD noise. The proposed noise model assumed as main contributions to the stochastic noise:

- σ_S, the shot noise produced by the fluorescence background and signal and the spurious charge. Shot noise can be derived from the second moment of the Poisson distribution
- σ_R, the read noise of EMCCD camera, which is described by the second moment of the Gaussian distribution
- σ_{EM}, the electron multiplication noise introduced by the gain process, which is described by the second moment of the Gamma distribution[134]

The final noise will be given by the sum of the not correlated noise sources $X_i = \Gamma, \mathcal{G}$:

$$Var\left(\sum_{i=1}^{N} X_i\right) = \sum_{i=1}^{N} Var(X_i) \qquad 2.36$$

$$\sigma_{tot} = \sqrt{\sigma_S + \sigma_{EM}}$$

The final simulated photon electrons will thus be given by:

$$n_{ie} = \mathcal{P}(QE \cdot n_{photIn} + c) \qquad 2.37$$

$$n_{oe} = \Gamma\big(n_{ie}, EM_{gain}\big) + \mathcal{G}(n_e, \sigma_R)$$

which leads to the final pixel counts:

$$ADU_{out} = min\left(\frac{n_{oe} - n_{oe} mod\ e_{ADU}}{e_{per_{adu}}} + BL, 65535\right) \qquad 2.38$$

Where:

- QE is the camera quantum efficiency
- C, the manufacturer quoted spurious charge
- EM_{gain} the electron multiplication gain
- G the total system gain
- e_{adu} , electron per ADU ADC conversion factor
- BL, the offset

The estimation of the maximum achievable localization accuracy using EMCCD camera (the Cramér-Rao lower bound - CRLB) has been previously derived elsewhere [135,136] and the beginning of this Chapter (2.3).

To develop a MLE algorithm for CMOS based datasets, however, a CMOS specific noise model should be included in the localization process.

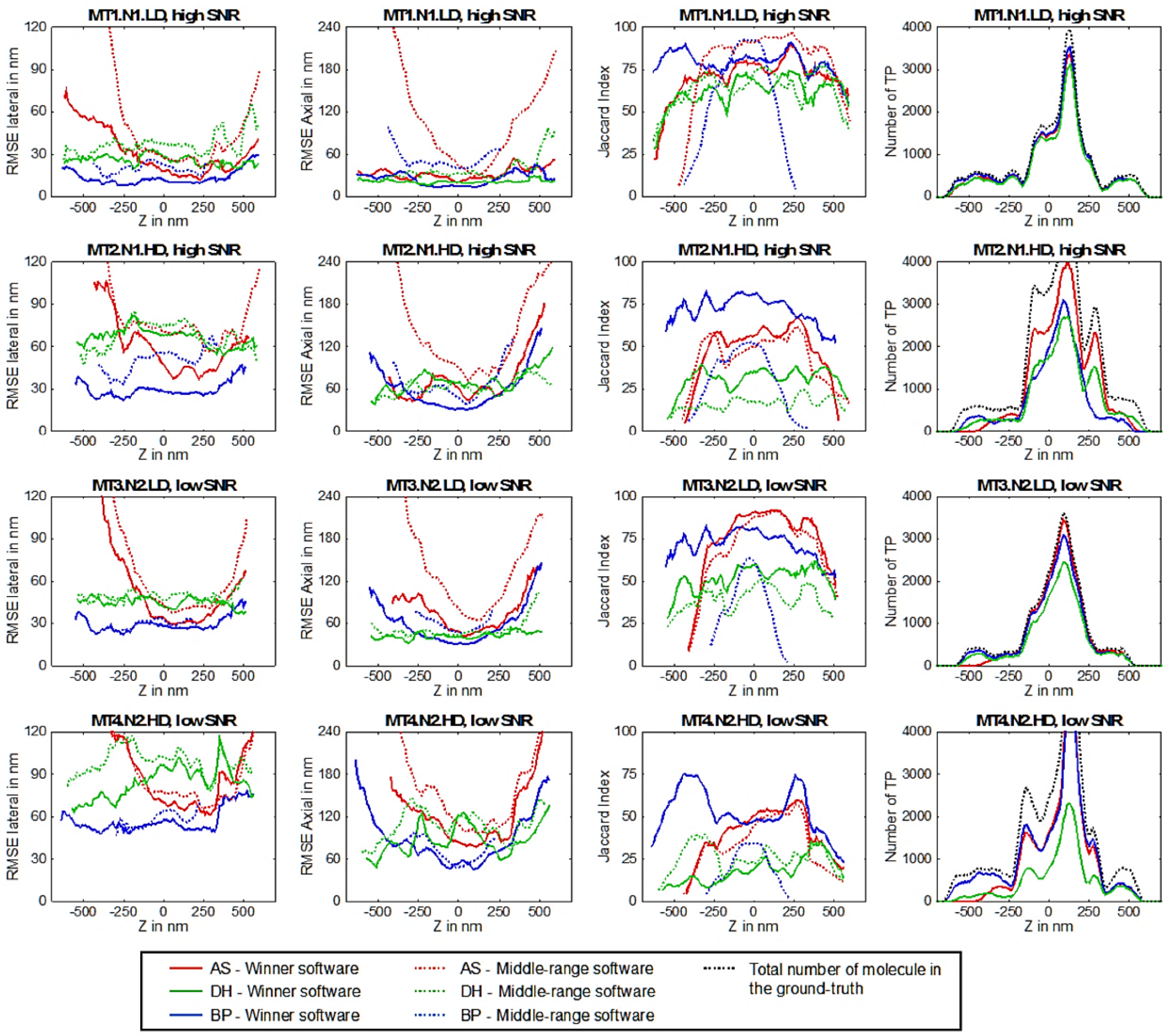

Figure 2-12 – DH-SMLM best-in-class algorithm performance. Figure taken from[39]. 3D software performance as a function of depth Z (axial position of the molecule) for each competition dataset**.**

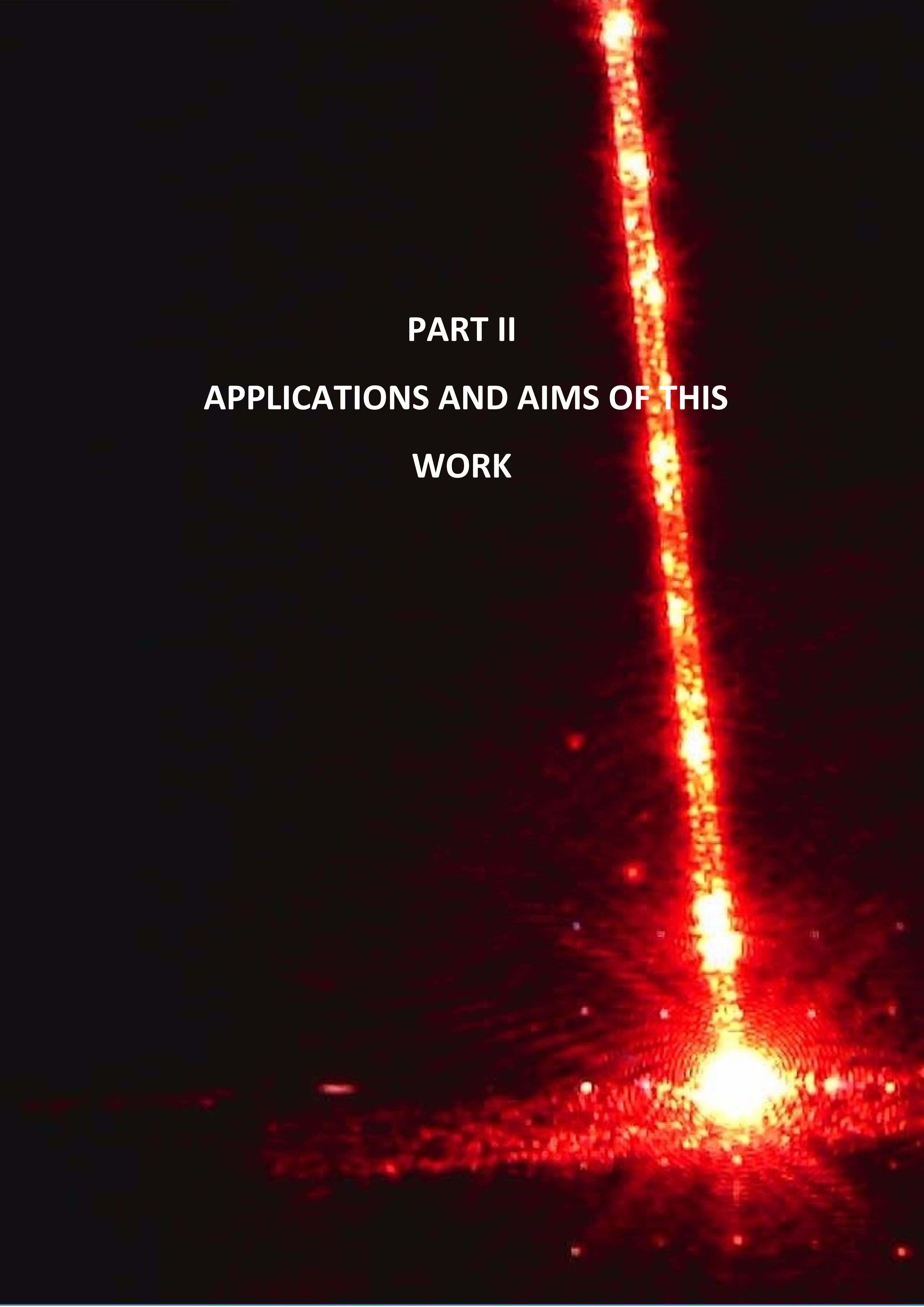

PART II

APPLICATIONS AND AIMS OF THIS WORK

3 Resolving bacterial cell shape dynamics

3.1 *Principles of C. crescentus* constriction rate modulation in cell shape dynamics

The setting of a specific cell shape and size at birth (size control) and its maintenance over multiple generations (size homeostasis) have been universally observed among prokaryotes[137]. They have been found to be critical regulatory processes for cell survival determination. Indeed, a too small a cell volume can limits the physical displacement of DNA to initiate chromosome segregation[138] or the spatial access of essential machinery essential for life. On the other hand, cell that are too large may be more vulnerable to nutrient uptake limitations and distribution[139].

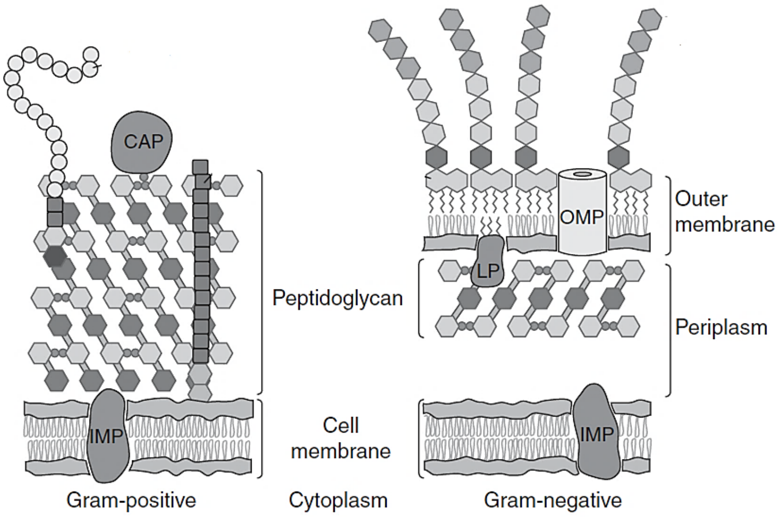

Figure 3-1 – C. crescentus cell envelope. Gram-positive (Left) and Gram-negative (right) cells envelopes with typical membrane proteins. CAP covalently attached protein; IMP, integral membrane protein; LP, lipoprotein; LPS, lipopolysaccharide. Figure from [140].

A ubiquitously adopted cell shape is the rod-like shape which has been embraced by many commonly studied species such as *Escherichia coli* and *C. crescentus* and by diverse organisms ranging from bacteria to fungi to plants[141]. The rod-like shape is easily parameterized by its width and length. In fact, the dynamics of the constriction and elongation determine growth rate, the cell cycle and ultimately the cell shape[142,143].

The bacterial cell envelope is typically a multi-layered structure (Figure 3-1) consisting of an inner, cytoplasmic membrane enclosed by a cell wall, and in the case of gram-negative bacteria, an outer membrane. The main element in determining the shape of the cell is the cell wall: a mechanically elastic structure composed of a crosslinked peptidoglycan (PG) network[144].

By remodeling the peptidoglycan (PG) network, the cell can tune different parameters such as the elongation rate, the constriction rate and the constriction onset and thereby regulate its size at the time of division. Thus, understanding how cell shape and size are set for individual cells requires an investigation into how the cell wall is built and remodeled[145] over both the elongation and the constriction processes. Remarkably, constriction makes up a significant portion of the cell cycle in many bacteria[146], for example, up to 40% for E. coli[147] or *C. crescentus* grown in minimal media[148].

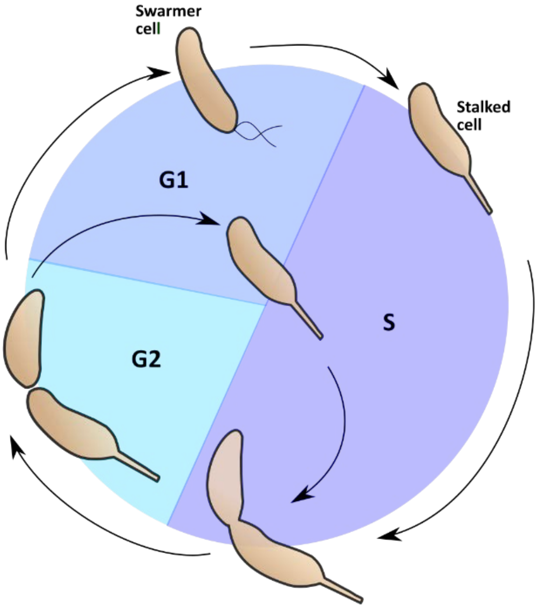

Figure 3-2 – *C. crescentus* cell cycle. Cells divide asymmetrically into a swarmer and a stalked cell at the end of G2. The swarmer cell must differentiate into a stalked cell to undergo DNA replication and proceed through cell cycle.

To reveal the roles of cell elongation and constriction in bacterial size regulation during cell division, we investigated the shape dynamics of *C. crescentus* in wildtype and under different perturbations, namely a hyperconstriction mutant FtsW**I* (to speed up the constriction process) or a fosfomycin inhibition (to slow down the constriction process). We choose to work with *C. crescentus* because of the relative ease of isolating large populations of cells synchronized in their cell cycle stage. *C. crescentus* undergoes asymmetric cell division and differentiates into swarmer and a stalked phenotypes (Figure 3-2). The swarmer cell inherits a flagellum and is motile, and it cannot undergo DNA replication (G1 phase, blue region). The other daughter inherits a stalk and is sessile, and undergoes active DNA replication (S phase, green region). During the last stage of the cell cycle (G2 phase, orange region), the predivisional-stalked cell is preparing for cell division. These two cell types can be separated by density centrifugation allowing the isolation of the swarmer cells from the rest of the population. In fact, lower density stalked and predivisional cells float near the top of the gradient while dense swarmer cells end up toward the bottom of the tube centrifugal tube[149].

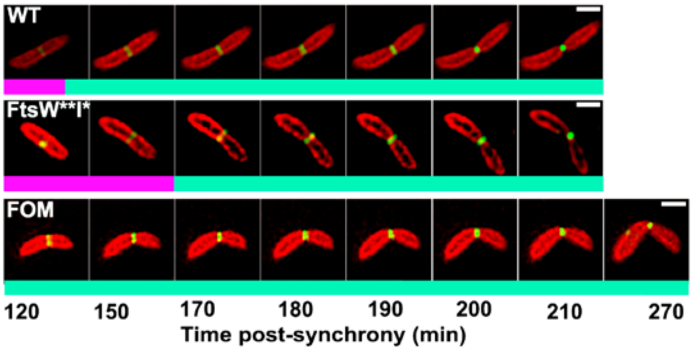

Figure 3-3 – Time-lapse dual color images of *C. crescentus*. SIM images of the inner membrane (mCherry-MTS2, red) and FtsZ (FtsZ-GFP, green). Each row corresponds to wildtype (WT), FtsW**I* mutant, and fosfomycin-treated cells respectively. Cell are images over the cell cycle till the end of constriction. Figure taken from [137].

In late stages of the constriction, the *C. crescentus* diameter at septum cannot be observed using conventional wide field microscope. Hence, superresolution microscopy is necessary to follow the constriction until the end of the cell cycle. In order to overcome the tradeoff between high resolution, phototoxicity and time resolution we aimed to use different superresolution techniques to access different information via different approaches.

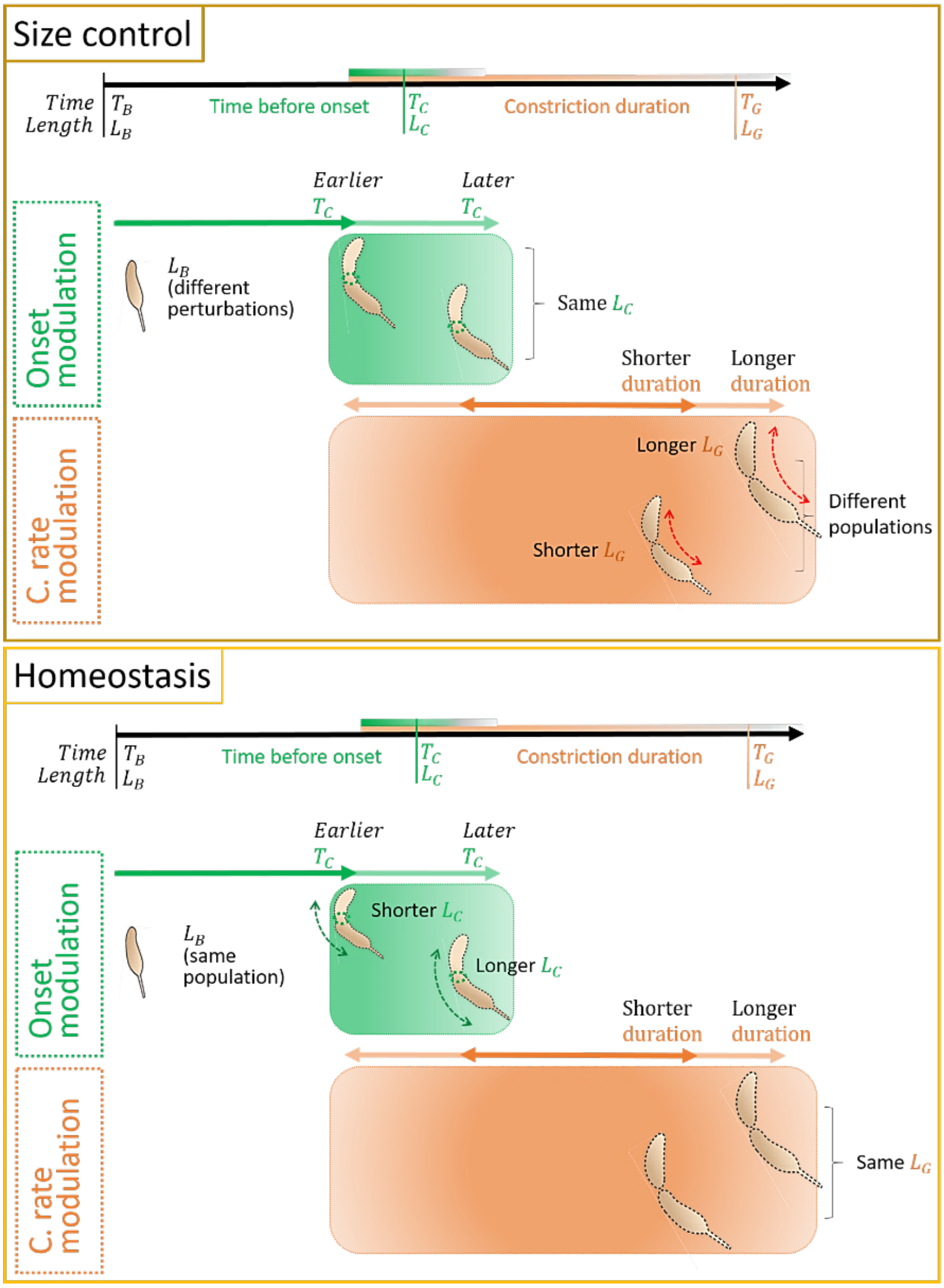
Size control
Time T_B Length L_B
Time before onset
T_C L_C
Constriction duration
T_G L_G
Earlier T_C
Later T_C
Onset modulation
L_B (different perturbations)
Same L_C
Shorter duration
Longer duration
C. rate modulation
Longer L_G
Shorter L_G
Different populations
Homeostasis
Time T_B Length L_B
Time before onset
T_C L_C
Constriction duration
T_G L_G
Earlier T_C
Later T_C
Onset modulation
L_B (same population)
Shorter L_C
Longer L_C
Shorter duration
Longer duration
C. rate modulation
Same L_G

Figure 3-4 – Model for cell size control and homeostasis in *C. Crescentus*. Constriction rate coordinates with the onset mechanisms to regulate the cell size within and across different populations.

We used a commercial SIM imaging[150] to perform live-cell dual color imaging of cell shape dynamics at the single cell level. However, we aim to implementation a double-helix (DH-PSF) 3D PALM method that could allow us to extract more detailed morphological information about the the entire 3D cell septum at higher resolution. To perform time-lapse dual color imaging we target the cell inner membrane protein MinD with a mCherry-MTS2 label[151] and the divisome proteins FtsZ and FtsW with a GFP label (Figure 3-3).

We investigated the role of constriction rate in cell size control and homeostasis and we showed that the constriction rate is coordinated with onset of constriction: cells that elongate more than average before constriction undergo a more rapid constriction thereby limiting the elongation during constriction, and vice versa. Specifically, differences in elongation before constriction for all conditions were insufficient to account for the observed differences in final length among the three different perturbations (size control). Although FtsW**I* cells have a later average onset time than WT and FOM-perturbed cells, they exhibited, on average, a shorter final length while having a similar average elongation before constriction.

Constriction rate modulation drives these changes across different perturbations (size control) and defines the overall cell elongation during constriction, which compensates for the differences in length before constriction (size homeostasis) - Figure 3-4.

3.1.1 *Cell size regulation*

In the presence of sufficient nutrients, the bacterial length dynamics can be described with an exponential function of time[152,153].

$$l(t) = L_0 e^{\lambda t} \tag{3.1}$$

The cell shape is dynamically modified by continuous remodeling of the cell wall layer through a "make before break" mechanism where new glycan chains are inserted by cross-linking to existing peptidoglycan before the old cross-links are broken. As soon as the old cross-links are broken, the new chains are pulled into the stress-bearing plane of the peptidoglycan by osmotic pressure[154].

Two main machineries regulate the cell wall remodeling process: the elongasome and the divisome which refer to the protein complexes involved in the longitudinal growth and inward growth respectively.
One of the main elongasome players around which are organized the other proteins is MreB an actin homolog which creates circular filaments along the cell length where PG remodeling occurs[155].
The divisome includes a filament forming protein, FtsZ, a homolog of tubulin that is recruited and assembled at the midcell. FtsZ filaments act as a scaffold to direct cell wall remodelers, such as the glycosyltransferase FtsW, to the division site. In turn FtsW is required for its cognate transpeptidase FtsI correct location[156].

In this work, we used *C. crescentus*-several-point-mutant FtsW**I* of both FtsW and FtsI[157,158] to induce an increase in the constriction rate. This perturbation together with fosfomycin inhibition (slowing down the constriction process) allowed us to investigate the role of constriction rate in cell control and homeostasis under different perturbations.

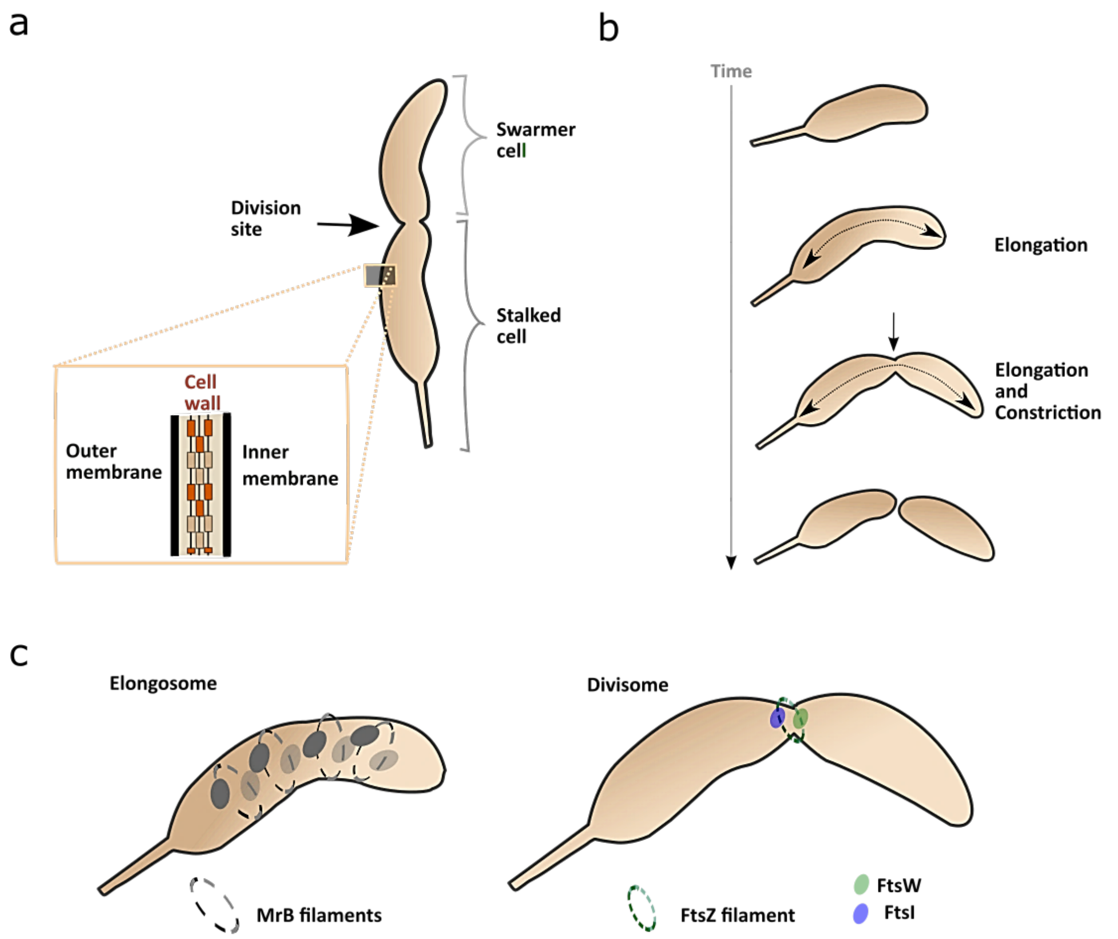
a
Swarmer cell
Division site
Stalked cell
Cell wall
Outer membrane
Inner membrane
b
Time
Elongation
Elongation and Constriction
c
Elongosome
MrB filaments
Divisome
FtsZ filament
FtsW
FtsI

Figure 3-5 – *C. crescentus* cell shape scheme. a, C. crescentus undergoes asymmetric cell division and differentiation into swarmer and stalked phenotypes by remodeling the crosslinked peptidoglycan (PG) network in the cell wall. **b,** Elongation and constriction machinery are inter-players in the cell shape regulation process. **c,** Main protein complexes involved in the elongation and constriction.

3.2 Aims of this work: cell shape parameters analysis

My goal within this project was to implement specific tools to extract and quantify the main cell shape dynamics parameters such as:

- implement a complete pipeline for cell shape dynamics analysis. More specifically, develop an interactive routine to visually inspect the desired images and automatically process hundreds of cells to extract, from each of them, their main shape parameters over every sampled time point of the cell cycle;
- implement a prototype of a simple cell shape simulator to predict the effect of constriction rate perturbation on the cell septum shape
- develop fast 3D reconstruction software to localize and render images of single molecule with a point spread function characterized by two lobes that moving in the axial direction generate a double helix (DH-PSF).

3.2.1 *Development of an automated image processing method and cell dynamic simulator*

The study of the shape of *C. crescentus,* and specifically of its constriction site dynamics, requires an accurate image processing approach capable of resolving and measuring the cell minimum diameter, which is hard to access due to the inward growth of the cell membrane.

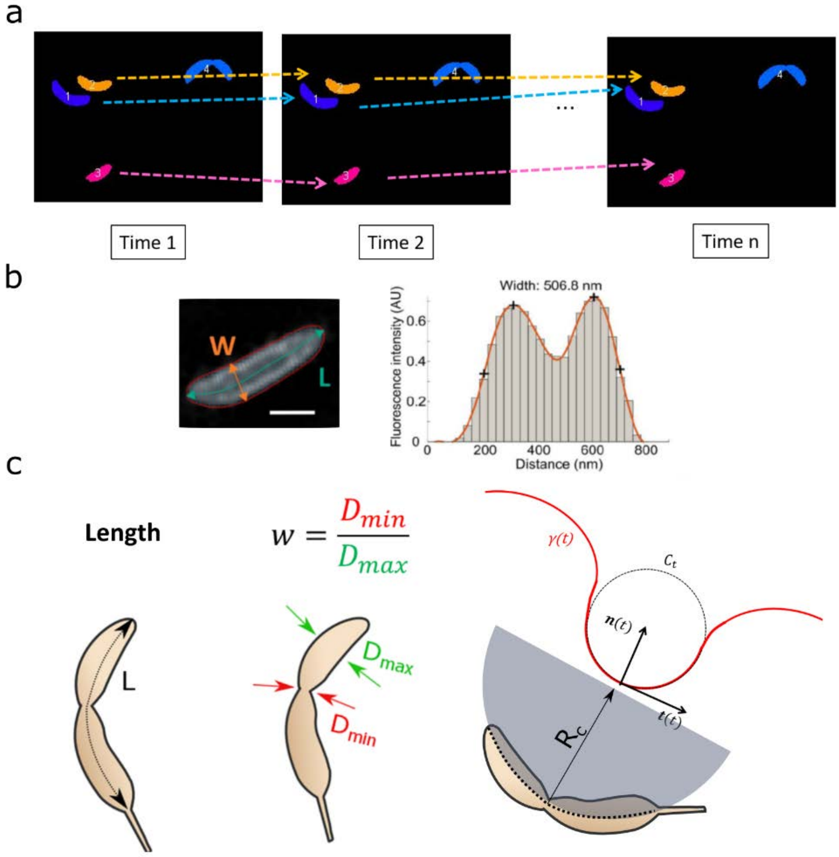

Figure 3-6 – *C. crescentus* shape images analysis. The analysis of *C. crescentus* septum dynamics requires three main steps: **a,** cell tracking; **b,** accurate edge detection; Left panel: at equal intervals along the centerline, the width W is measured by extracting the intensity profile along a slice (cyan rectangles) perpendicular to the centerline (thick cyan colored line) . The red line represents the first guess of the contour. Right panel: The extracted intensity profile (grey bars) is smoothed by fitting a spline (orange line). The maxima are calculated (top plus signs on orange line), and the outer position with the half-maximum value is found (lower plus sign on orange line). The distance between these two positions is defined as the width. Panel taken from realized by Aster Vanhecke[137]. **c,** Cell shape parameter extraction. The waist diameter *w* is the ratio between the local and the maximum diameters; The curvature is define as the inverse of the radius of the osculating circle. Scale bar 700 nm.

This is why we developed a specific which can not only measure cell shape parameters performing standard cell segmentation, tracking and shape parameter measurements, but also provides extremely narrow edge detection of the septum (Figure 3-6). The algorithm extracts the main cell shape parameters such as length, diameter (W) and curvature (1/k), where the curvature is extracted via the fitting and average of the osculating circle:

$$k(t) \overset{\text{def}}{=} \|\gamma''(t)\| \cdot \frac{1}{[1+\gamma'(t)^2]^{3/2}}$$
$$R_C = \frac{1}{k(t)} \qquad 3.2$$

where $\gamma(t) = (x(t), \quad y(t))$ is a parametric representation of the bacteria contour, *k* is the curvature and R_C the radius of the osculating circle.

We further investigated the septum dynamics using simulation starting based on a simple geometrical parametrization and on the hypothesis that septum formation occurs on two hemispherical surfaces[159] corresponding to the two new cell poles (Figure 3-7). Thus, the inserted surface at time *t* on one side of the septum is:

$$S(t) = [2\pi \cdot R^2 - 2\pi \cdot R \cdot h(t)\,] \cdot 2 \tag{3.3}$$

where R is the radius of the 3D hemispherical cap (assumed equal to half of the maximum width of the bacteria) and *h* is the height of the missing section of the new cap.
Thus, the radius of the septum at the time t:

$$r(t) = \sqrt{R^2 - (R - h(t))^2} \tag{3.4}$$

narrow edge detection of the septum.

Now, assuming that the septal region grows at a constant rate, the height *h* of the missing section of the new cap is zero when the constriction finishes (at the generation time t_g) and it is equal to *R* when the constriction starts (t_c):

$$\begin{cases} \dfrac{dS(t)}{dt} = \dfrac{d}{dt}[4\pi \cdot R^2 - 4\pi \cdot R \cdot h(t)] = cost \\ \dfrac{dR}{dt} = 0 \\ h(t_g) = 0; \quad h(t_c) = R; \end{cases} \tag{3.5}$$

then,

$$h(t) = R \cdot \left(\frac{t_g - t}{t_g - t_c}\right) \tag{3.6}$$

Now, since

$$\begin{aligned} \frac{r(t)}{R_{max}} &= \frac{1}{R_{max}}\sqrt{R^2 - (R - h(t))^2} \\ &= \frac{R}{R_{max}}\sqrt{1 - \left(1 - \frac{h(t)}{R}\right)^2} \end{aligned} \tag{3.7}$$

and defining the septum waist diameter $w(t)$ as:

$$\frac{r(t)}{R} = \frac{w(t)}{2} \qquad and \qquad \frac{R}{R_{max}} = \frac{w_{max}}{2} \tag{3.8}$$

The septum waist diameter dynamics becomes[159]:

$$w(t) = w_{MAX} \cdot \sqrt{1 - \left(1 - \frac{t_g - t}{t_g - t_c}\right)^2} = w_{MAX} \cdot \sqrt{1 - \left(\frac{t - t_c}{t_g - t_c}\right)^2} \tag{3.9}$$

We assumed this dynamics of the waist diameter for a qualitative shape prediction of the new poles forming at septum.

The average cell volume dynamics behavior is straightforward to derive since it depends directly on the growth rate[160]. More precisely, the logarithm of the average cell volume is proportional to the growth rate (λ) multiplied by a constant time (T), equal to 60 minutes at 37°C:

$$log\,V \sim \lambda \cdot T \tag{3.10}$$

known as the growth law.

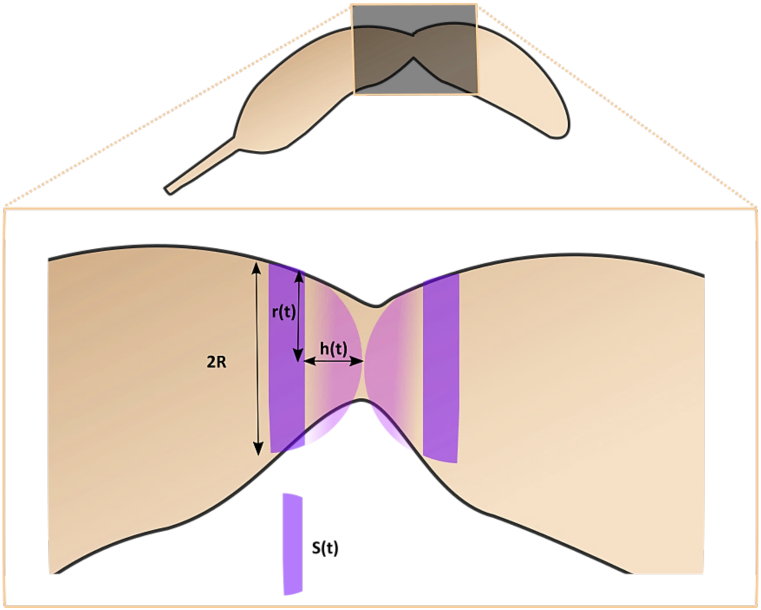

Figure 3-7 – *C. crescentus* septum shape dynamics. C. crescentus septum dynamics can be roughly approximated assuming a hemispherical surface insertion with a constant rate up to division.

3.2.2 *Development of 3D Double-Helix PSF software*

To accurately probe the *C. crescentus* septum at different stages of the entire cell cycle form the start (where the diameter is roughly 500 nm) to the very last phase of constriction, a 3D SMLM approach based on engineered PSF represents the best candidate to achieve high axial resolution over a larger range than the standard astigmatism approach or iPALM.

In Chapter 1.1.2, we described the advantages and disadvantages of the 3D DH-PSF-based SMLM approach with a specific focus on the limitation of the currently available DH-PSF algorithm that we would like to overcome. In particular, we underlined that 3D SMLM approaches based on an engineered PSF provide a more extended axial range at the cost of increasing the lateral extent of the PSF. This characteristic aspect leads, on one hand, to a localization performance uniform and close to the CRLB even far from the focal plane, but on the other hands to poor performance at high molecule density[39].

We aimed to develop a fast and easy-to-use MLE algorithm specific for DH-PSF to process thousands of single molecule images from hundreds of bacteria. Specifically, our goal was to implement a multi-emitter DH-PSF localization maximum-likelihood estimator (MLE) algorithm based on analytical fitting of a double Gaussian and capable of taking into account different sources of noise (camera noise, molecule signal shot noise and variable background). We thus set the following intermediate goals to study and address this challenge:

- Develop a simple DH-PSF simulator to generate a DH-SM 3D ground truth to test the algorithm
- Develop a least-squares (LS) based fitting algorithm of the PSF intensity profile $I(x, y)$ with a reduced number of free parameters compared to the previously proposed approach125:

$$I(x,y) = I_0^A exp\left(-\frac{(x-x_A)^2+(y-y_A)^2}{2\sigma_A^2}\right) + I_0^B exp\left(-\frac{(x-x_B)^2+(y-y_B)^2}{2\sigma_B^2}\right) \tag{3.11}$$

- Use LS fitting as a first guess for an MLE algorithm implementation
- Develop a low pass temporal filter to account for the variable spatial background due to the more extended DH-PSF axial range and lateral extent.
- Develop a fast C++ identification and lobe-coupling step
- Develop an intermediate rejection step which uses the information extracted from the calibration procedure to limit the parameter landscape
- Develop a spatio-temporal grouping of localizations belonging to the same molecule
- Develop a set of result rendering functions (apply wobble correction, save localization data, display 3D histogram, etc.)

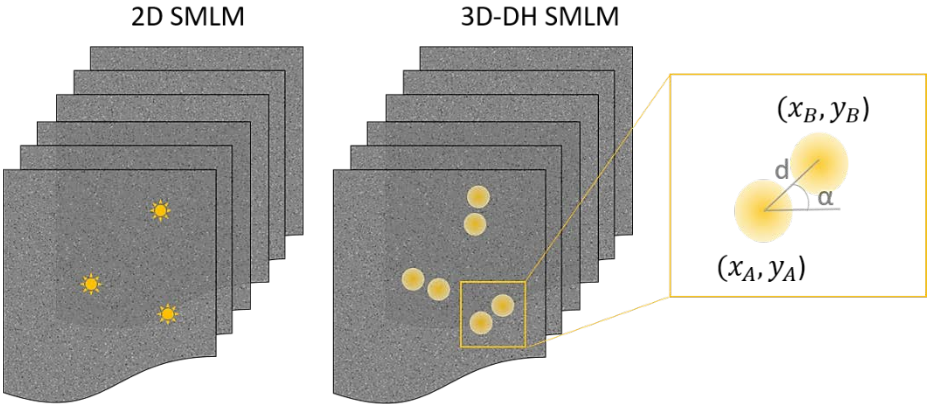

Figure 3-8 – From 2D SMLM to 3D DH-PSF data. A DH-PSF phase mask transform the SM standard quasi-Gaussian PSF into a double-lobe quasi-double-Gaussian PSF where the axial position is encoded in the angle formed by the relative position of the two lobes with centers (x_A, y_A) and (x_B, y_B).

4 High-throughput nanoscopy of subcellular structure: large flat field STORM and PAINT

Building on its ability to investigate large-scale macromolecules networks in their natural environment and with specificity, fluorescence microscopy is further evolving by the development of quantitative and high-throughput methods to characterize such networks[161–164]. Recently, HT-STORM combined with a semi-automated computational workflow demonstrates the capability of accurately reconstructing 3D protein structures starting from large 2D multicolor particle datasets[165].

Large datasets require either the temporal or the spatial extension of the imaging capability. Previous implementations of high-throughput microscopy made use of scanning smaller fields of view[163], which makes axial alignment a challenge and extends the imaging time. This is why we aimed to develop a large FOV system and to extend a flat-illumination techniques to other methods such as optical sectioning.

First, we achieved a flat-field epi fluorescent excitation building a Koehler integrator system into a STORM microscope equipped with a speckle scrambler (the rotating diffuser) placed near the intermediate focal plane of the telescope (the beam-expander) and with a sCMOS camera.

Second, we developed a large and uniform TIRF platform for performing DNA-PAINT experiments.

4.1 Aim of this work: CMOS camera characterization for MLE sCMOS-specific algorithm

The detection is the last active stage in the molecule signal collection. Indeed, the camera characteristics set the achievable field of view, imaging speed and signal to noise ratio of the imaging process. Recent advances in SMLM leaded to the replacement of Electron-Multiplying Charge Coupled Device CCDs (EMCCD) in favor of sCMOS (scientific-grade Complementary metal–oxide–semiconductor) sensors to improve either speed[66] or FOV size[70].

In sCMOS cameras, each pixel has its own readout amplifier that converts photoelectrons to voltage before the column level amplification and analog to digital conversion stages. This per-pixel conversion followed by a column-wide gain and digitalization results in a faster operation than the one achievable in a EMCCD sensor where photoelectrons are first collected at each pixel, then transferred row by row down to the readout register and finally converted in voltage. However, the speed and flexibility in sCMOS pixel architecture require the presence of optically insensitive transistors at each pixel that compete with the active area for photon detection. In other words, the pixel readout speed comes at the expense of the pixel fill factor making it hard to reduce the pixel size.

Nevertheless, thanks to the advance in CMOS technology, sCMOS camera can now be fabricated with lower pixel size than typical EMCCD camera pixel size[166], with higher quantum efficiency and lower price[166,167]. This aspect is particularly crucial not only for improving the spatial molecule sampling but also for reducing the read noise. In fact, read noise depends not only on the readout speed but also on the area of the active capacitor storing the charge[168].

Although sCMOS camera capability to perform SMLM has been demonstrated[169], its sensor architecture introduces pixel dependent signal variance, offset and gain. At low photon emission, where the pixel readout noise is not anymore strongly dominated by the molecule signal shot noise, a specific SMLM algorithm capable to incorporate the noise statistics in the likelihood function[66] is particularly crucial for improving the localization precision (Figure 4-1).

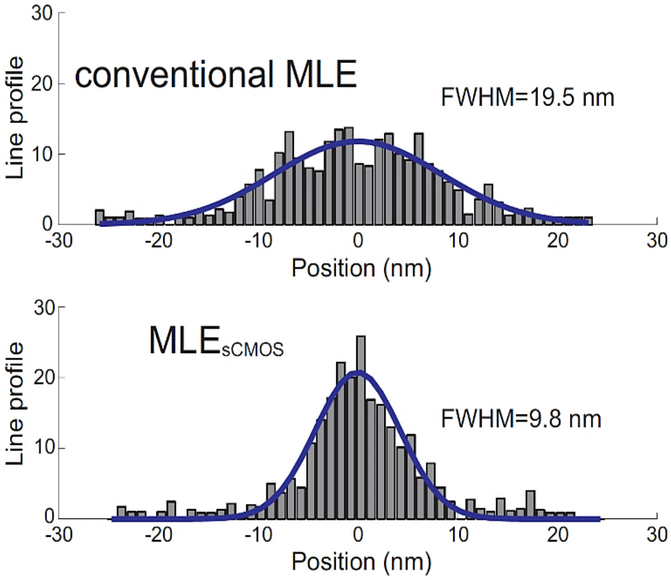

Figure 4-1 – Localization precision with sCMOS specific MLE algorithm. Comparison between a sCMOS MLE algorithm versus conventional MLE approach where the pixel dependent noise is not taken into account. Figure taken from [66].

This is why we took care of the characterization of our sCMOS camera and we test its performance with a suitable SMLM sCMOS specific software[66].

To characterize the sCMOS camera I developed a specific MATLAB routine that takes as inputs the dark images and images stacks at different intensities and compute the main camera parameters that are pixel dependent: the gain and the noise. Finally, we tested the CMOS specific algorithm with artificial 2D SM datasets generated with different signal to noise ratio.

Noise is a probabilistic process that affects every uncertain events that have to be measured. In fluorescence microscopy, noise involves the photon emission, the background generated by laser scatter light, background produced by out of focus auto florescence signal, the photon detection process, the photoelectrons readout, the detector thermal couple production. The noise corresponds to the standard deviation of the distribution describing the probabilistic behavior of the system. Fundamental sources of noise present in a detection process performed with a sCMOS camera are:

- the shot noise σ_S due to the quantum proprieties of fluorescence emission photon signal. This noise contribution is independent on camera characteristics.
- the read noise σ_R due to the conversion of the analog signal to the digital signal. Such a noise is the sum of the pixel amplifier noise and any other noise sources that are independent of the signal level.
- the dark noise σ_D due to the generation of thermal electron-hole pairs production which gives false photo-electrons events.

The noise sources are reasonably independent of each other since their corresponding events are uncorrelated. Then, the variance of the sum of these events is equal to the sum of their variances, or, expressed symbolically:

$$Var\left(\sum_{i=1}^{N} X_i\right) = \sum_{i=1}^{N} Var(X_i)$$

$$\sigma_{tot} = \sqrt{\sigma_S + \sigma_R + \sigma_D} \tag{4.1}$$

The shot noise is the fluctuation of the photons flux hitting the detector following a Poisson distribution. Thus, the shot noise is equal to square root of the average number of photons and increases with intensity. On the contrary, read noise is independent on photon signal intensity since it is a normal random process depended on the gain and the exposure time of the camera. Finally, the thermal noise can be neglected considering that sCMOS camera are typically cooled down to limits the dark current down to about 0.1-0.2 e-/pixel/sec. Thus, equation 4.1 becomes:

$$\sigma_{tot} = \sqrt{\sigma_S + \sigma_R} \tag{4.2}$$

To extract the gain g of each pixel we first study its relationship with the final measured signal in ADUs (Analog-to-Digital conversion Units). If we subtract the dark counts (offset) from the measured signal s, s becomes:

$$s = g \cdot n_e \ \text{[ADU]} \tag{4.3}$$

where g is the gain measured in [ADU/e-]. Since the number of detected electrons is a Poisson process:

$$n_e = {\sigma_{n_e}}^2 \tag{4.4}$$

the standard deviation of s becomes for simple propagation:

$$\sigma_S = g \cdot \sigma_{n_e} \tag{4.5}$$

and thus, the final total noise is linked to the gain and read noise by:

$$\sigma_{tot}^2 = \left(g \cdot \sigma_{n_e}\right)^2 + \sigma_R^2 \tag{4.6}$$

To find a robust approach to extract the gain g from measured dataset, we further study equation 4.6:

$$\sigma_{tot}^2 = g^2 \cdot \frac{s}{g} + \sigma_R^2 \quad \Rightarrow \quad s \cdot g = \sigma_{tot}^2 - \sigma_R^2 \tag{4.7}$$

thus:

$$(\sigma_{tot}^2 - \sigma_R^2) - s \cdot g = 0 \tag{4.8}$$

Measuring σ_{tot}^2, σ_R^2 and s at different intensity level *k:*

$$\begin{cases} \left({\sigma_{tot,1}}^2 - {\sigma_R}^2\right) - s_1 \cdot g = 0 \\ \left({\sigma_{tot,2}}^2 - {\sigma_R}^2\right) - s_2 \cdot g = 0 \\ \vdots \\ \left({\sigma_{tot,k}}^2 - {\sigma_R}^2\right) - s_k \cdot g = 0 \end{cases}$$

the best estimation of the gain for each pixel can be computed:

$$g = argmin \sum_{k=1}^{K} \left[\left({\sigma_{tot,k}}^2 - {\sigma_{R,k}}^2\right) - s_k \cdot g\right]^2 \qquad 4.9$$

The Least-Squares solution theorem states that for a linear equation of $\boldsymbol{g} \in \mathbb{R}^n$ (here $\boldsymbol{g} \in \mathbb{R}^1$):

$$S\boldsymbol{g} = V \qquad 4.10$$

where $S \in \mathbb{R}^{m \times n}$ and $V \in \mathbb{R}^m$ (here $S \in \mathbb{R}^{K \times 1}$ and $V \in \mathbb{R}^K$):

$$S = \begin{pmatrix} s_1 \\ s_2 \\ \vdots \\ s_k \end{pmatrix} \qquad V = \begin{pmatrix} {\sigma_{tot,1}}^2 - {\sigma_{R,1}}^2 \\ {\sigma_{tot,2}}^2 - {\sigma_{R,2}}^2 \\ \vdots \\ {\sigma_{tot,k}}^2 - {\sigma_{R,k}}^2 \end{pmatrix}$$

the general form of leas-squares solutions is given by:

$$\boldsymbol{g} = S^+V + (\mathbf{1} - S^+S)\boldsymbol{z} \qquad 4.11$$

where $\boldsymbol{z} \in \mathbb{R}^n$ is an arbitrary vector and $\mathbf{1}$ is an identity matrix. The minimum norm solution among all the solutions provided by equation 4.11 is

$$\boldsymbol{g} = S^+V \qquad 4.12$$

where $S^+$is the pseudo-inverse (Moore-Penrose inverse) of *S*, for $m > n$:

$$S^+ = (S^TS)^{-1}S^T \qquad 4.13$$

Thus:

$$\boldsymbol{g} = \left(\begin{pmatrix} s_1 \\ s_2 \\ \vdots \\ s_k \end{pmatrix}^T \begin{pmatrix} s_1 \\ s_2 \\ \vdots \\ s_k \end{pmatrix}\right)^{-1} \begin{pmatrix} s_1 \\ s_2 \\ \vdots \\ s_k \end{pmatrix}^T \begin{pmatrix} {\sigma_{tot,1}}^2 - {\sigma_R}^2 \\ {\sigma_{tot,2}}^2 - {\sigma_R}^2 \\ \vdots \\ {\sigma_{tot,k}}^2 - {\sigma_R}^2 \end{pmatrix} \qquad 4.14$$

Where

$${\sigma_{tot,k}}^2 = \frac{1}{K} \sum_{k=1}^{K} (\bar{s} - s_k)^2 \qquad 4.15$$

$${\sigma_R}^2 = \frac{1}{M} \sum_{m=1}^{M} (\bar{o} - o_m)^2 \qquad 4.16$$

where o_m and $\bar{o}$ are the counts signal and offset (average dark count over M frames) measured in the dark.

Another straightforward approach to compute the gain in a rough but easy and fast way is based on the following observation. For an increase in illumination of Δn_e, the camera's average signal level will change by $g \cdot \Delta n_e$. In contrast, the same increase in illumination level will cause the signal variance ${\sigma_s}^2$, to change by $g^2 \cdot \Delta n_e$ (using equation 4.4 and 4.5). The ratio of these two quantities is the slope of the line measured when plotting the signal variance as a function of the average signal. Thus, the camera gain g, is obtained by fitting a line to this variance curve in the shot noise limited region and measuring the slope of that line.

4.2 Aim of this work: development of a waveguide-based platform for DNA-PAINT

As we previously explained (Chapter 2.2), employing a waveguide chip to generate an evanescent-field fluorescence illumination is a promising approach to achieve TIRF excitation over a large FOV in fluorescence microscopy applications. This is particularly true for DNA-PAINT microscopy where a waveguide-based TIRF illumination would decisively enhance the imaging performance, thanks to the uniform and wide excitation area. Furthermore, it would augment the setup flexibility, permitting a greater range of objective lens.

Although waveguide evanescence field illumination has been tested for fluorescence microscopy[56–59] and in super-resolution microscopy[60], making this approach an optimized solution for DNA PAINT requires further development. The waveguide-PAINT platform should provide a uniform evanescent field, a system for easy waveguide chip mounting and unmounting under the microscope and a simple access for buffer exchange.

To enable waveguides to be used for PAINT, we needed to build a chip holder that would allow access to the entrance window of the waveguides for coupling with excitation light. It also needed to hold the liquid imaging buffer over the sample to allow fluorophore exchange. Ideally, the holder would also facilitate alignment for easy coupling, and prevent scattered light from entering the detection path. In the previously proposed waveguide platform[60] the chip was secured with a vacuum holder which is more prone to vibration and devoid of the aforementioned features.

Here we developed a waveguide chip and chip holder system optimized for easy waveguide coupling and fast buffer exchange. It enables large and uniform FOV TIRF DNA-PAINT combined with an upright, cost-effective custom made microscope.

The flexibility of the waveguide platform stems from the customizable holder and chip layout. A compact microscope realization is achieved with a two Z-stage system integrated in an independent four-column mechanical structure. All this is realized with off-the-shelf opto-mechanical components. Finally, the high refractive-index contrast waveguide chip embeds a long mode-expansion-nanotaper to enhance mode selectivity and simplify coupling. Together this platform ensures an efficient and uniform illumination when combined with a rotating polarizer.

PART III

METHODS DEVELOPMENT AND RESULTS

5 Resolving bacterial cell shape dynamics

In Chapter 3.1 we explained why we investigated the shape dynamics of *C. crescentus* under different perturbation using mutant FtsW**I* mutant to speed up the constriction process and fosfomycin inhibition to slow down the constriction process. In this chapter, we will explain how we studied *C. crescentus* cell shape dynamics[137].

To follow the cell envelop and divisome proteins FtsZ and FtsW we targeted the cell inner membrane protein MinD with mCherry-MTS2 label and the divisome proteins with GFP labels.

Time-lapse dual color imaging of the cells was performed with 488 nm and 561 nm lasers excitation of the divisome protein-eGFP channel and the mCherry-MTS2 channel respectively under a commercial 3D NSIM Nikon microscope equipped with a back-illuminated EMCCD camera (iXon 3, Andor Technology). The acquisition time was set at 200 ms and 100 ms (5 fps and 10 fps) for the 561 and 488 channels with laser power of 4 W/cm^2. Every FOV was the results of fifteen images – five phase-shifted images per angle at each of the three interference pattern angles – reconstructed with the Nikon NIS-Elements commercial software. High-resolution, live-cell imaging over the cell cycle was achieved by capturing every FOV at 5 min or 10 min (for fosfomycin-treated cells) time intervals to minimizing photo-bleaching. The super-resolved SIM images were then processed via a custom-made software package called sDADA (Shape Dynamics Automated Data Analysis) which will be described in the following paragraph 5.1.

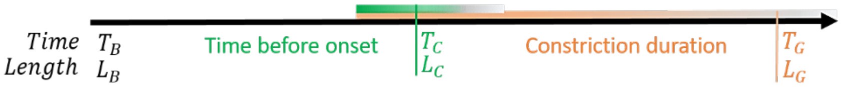

Figure 5-1 – Parameter space in cell shape dynamic study. The main parameters involved in the analysis are the cell lengths at birth T_B, at constriction start T_C and end of division T_G.

For the analysis, we defined the following parameters:

- time zero (T_0) the time at which the suspension of synchronized bacteria is added to the agarose pad. This occurred approximately 20-40 minutes before starting time-lapse SIM acquisition.
- T_Z, and T_W are the constriction onset time measured with different approaches. T_Z is the time of the FtsZ assembly, which we assumed to occur when the fluorescence intensity of FtsZ-eGFP at mid-cell was three times higher than elsewhere. T_W is the FtsW arrival time measured as the moment at which the FtsW signal appeared stable at midcell .
- T_C is the time at which the constriction invagination depth is equal to a predetermined normalized waist width threshold. To find the optimal threshold, we tested different thresholds in the reasonable range from 80% up to 99% of the maximum diameter, with step sizes of 1 %. Since FtsW arrival time is an alternative readout of the constriction start the T_C values computed from the waist diameter versus time should strongly and robustly correlate with the T_W values. For each threshold, we computed the Pearson’s correlation coefficient for the scatter plot of the T_C values versus the T_W values of all the cells. We found that a threshold of 92% had the best correlation coefficient and minimal least square error for T_C versus T_W.
- Generation time (T_G) and final length (L_G) are the time and the length at which the cell divide.
- Constriction duration τ is the difference between T_G and T_C, or when specified, T_W.
- The length at birth, L_B and the elongation rate λ are extracted from the exponential fitting of the elongation versus time curve.

- The length at the constriction onset, L_C, L_Z or L_W, were measured as the lengths at T_C, T_Z and T_W respectively. The total elongation is the difference between L_G and L_B.
- Elongation before constriction and during constriction are defined respectively as the difference between L_G and L_C, and between L_C and L_B. When specified, L_W can be used instead of L_C.

5.1 Bacteria cell image processing: sDaDa

sDaDa is a quantitative image analysis tool for cell shape dynamics study. Specifically, I developed sDaDa in a MATLAB environment for processing time-lapse dual color images of bacteria such as *C.crescentus* (FtsZ-GFP, FtsW-GFP (green channel) and mCherry-MTS2 (Szeto et al., 2003) (red channel)). I implemented the skeleton building blocks of the software pipeline (e.g. image segmentation, cell tracking, edge detection) with the support of my colleague Aster Vanhecke who added the pipeline block for the second channel analysis of the divisome protein, took care of debugging the code and implemented the necessary code for the statistical tools. The code has been used to analyze the data on our published work[137].

sDADA generates scatter plots, histograms and violin plots to study key parameters controlling the cell size and homeostasis, such as: elongation rate, constriction duration, length at birth, onset, onset time. sDADA extracts these parameters from the analysis of the cell shape dynamics thanks to semi-interactive modules for image segmentation, edge detection, cell filtering, cell tracking and statistical analysis. The first cell identification and edge detection guesses are inspired by microbeTracker[170] approach. However, to be able to measure the constriction site up to the last stages of the constriction we needed to implement a further optimization of the edge detection step by tightly slicing the cell along its length and analyzing the intensity profile across each slice to extract the maxima corresponding to the cell edges.

The program takes as input the time-lapse images, the camera parameter (i.e. pixel size) and a set of experimental parameters (i.e. starting time, time interval between two consecutive frames, the field of view (FOV)). The program outputs a data structure containing all the measurements of each cell at each frame and a set of figures with the results of the measurements.

The description of the main features of the sDaDa program and of the general steps in a typical pipeline (Figure 5-2) are (1) image segmentation and first edge detection guess, (2) cell tracking, (3) edge detection refinement and shape parameters measurement, (4) divisome ring identification (5) shape parameters correlation analysis and outputs display.

More specifically, the segmentation step (1) is on a first Otsu's thresholding approach[171] to distinguish background pixels from foreground one followed by neighborhood pixels connection. The Otsu's method sets a proper threshold via maximizing the inter-class variance of the bi-modal histogram of the pixel intensities (foreground pixels and background pixels). Connected pixels that have a signal value higher than the threshold are tagged with the same number and identify as part of a cell only if they form an area bigger than 0.5 μm^2. We used two built-in MATLAB functions for Otsu's image thresholding and to identify each individual cell. The `model2mesh.m` function form microbeTracker[170] defines the first cell contour guess and returns two semi-contours, corresponding to the 'left' and 'right' sides of the cell. From the two semi-contours, the bacteria poles (the two farthest apart points on the contour) and the centerline (the average of the two half contour parts) can be easily identified.

The cell shape search, control and refinement is done thanks to an interactive tool which allows the user to manipulate the cell area such as removing parts, joining two regions, smoothing, expanding. The user can also choose to delete the current time point of the cell or to mark the cell as divided, after which it will no longer be followed.

Each single cell is tracked – step (2) – in consecutive frames comparing the cell area and their relative barycenter distance. The two regions correspond to the same cell if the difference between these two spatial distributions is lower than a user-defined tolerance parameter. The tracking search stops when the cell divides or when one region does not pass the search criteria.

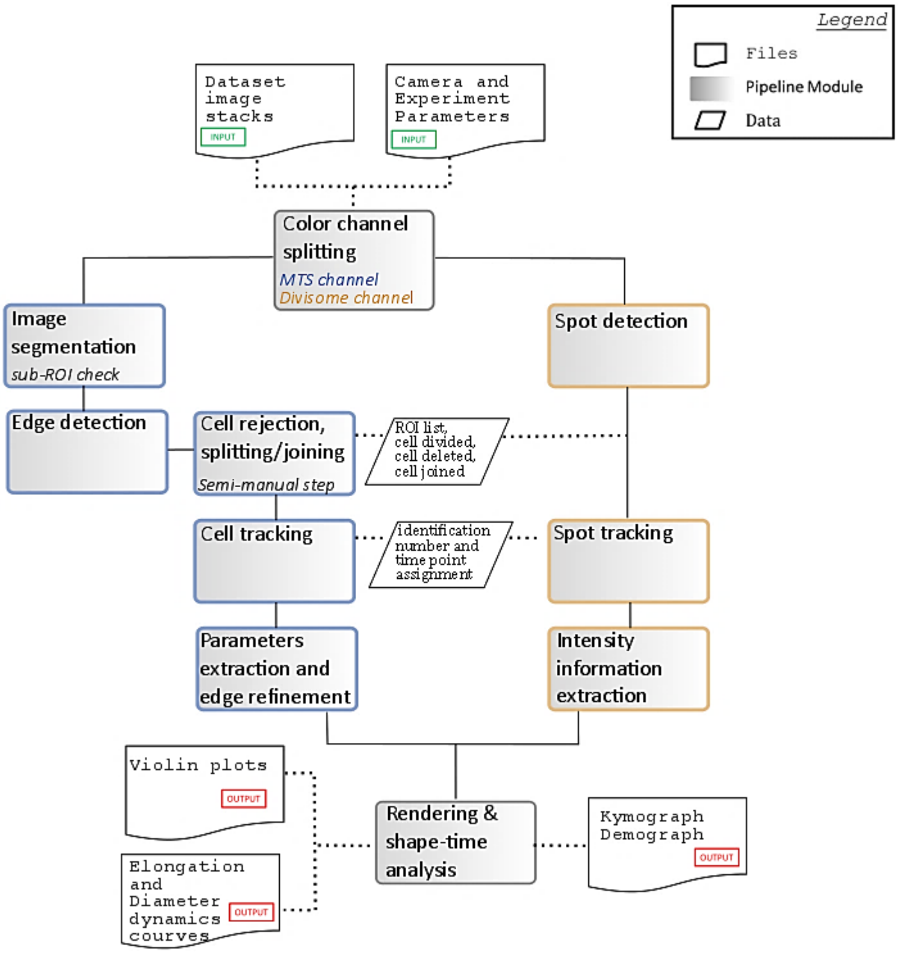
Legend
Files
Pipeline Module
Data
Dataset image stacks
INPUT
Camera and Experiment Parameters
INPUT
Color channel splitting
MTS channel
Divisome channel
Image segmentation
sub-ROI check
Spot detection
Edge detection
Cell rejection, splitting/joining
Semi-manual step
ROI list, cell divided, cell deleted, cell joined
Cell tracking
identification number and time point assignment
Spot tracking
Parameters extraction and edge refinement
Intensity information extraction
Violin plots
OUTPUT
Rendering & shape-time analysis
Kymograph Demograph
OUTPUT
Elongation and Diameter dynamics courves
OUTPUT

Figure 5-2 – Cell shape analysis program sDaDa pipeline. The figure shows: the main software steps (light gray), the main inputs (green label) and outputs (red label). The pipeline splits into two colors (blu and yellow) which represent the two software braches developed to analysis the two channels (MTS and Divisome respectively).

The segmented regions, containing a well-identified cell, can therefore enter the second stage (3) where the program extracts and accurately measures the shape parameters described below.
The diameter is measured by taking perpendicular slices of the bacteria image along its centerline length.

Using the intensity profile along each slice, a histogram with two maxima corresponding to the cell edge will define the diameter. The intersection of the histogram with a line parallel to the abscise axis at half maximum high, identifies up to four abscises (two for each maximum). The diameter is thus the difference between the two furthest apart abscises. Repeating this procedure for each slice of the bacteria, the diameter profile as a function of the length could be achieved (Figure S2). The minimum between two maxima of the diameter as a function of the length will then define the measure and the position of the constriction site. As a consequence, the waist width will be easily defined: the ratio of the width of the constriction site and the maximum diameter along the cell. Lastly, the length is measured by calculating the arc length of the centerline.

The program examines the temporal evolution of the length and the waist width for all single cells detected in a time-lapse experiment. From these curves, it extracts the elongation rate, the length at birth (L_B) and the division time (T_G). The volume and the surface area of a cell are estimated based on the measured widths along the length of the bacterium. The width versus the length profile is first smoothed using a spline function, to filter out the noise that would inflate the surface area estimation. The bacterium is assumed symmetric along its central axis. Therefore, assuming cross-sections perpendicular to the axis are circular, the volume and surface area can be computed by treating the measured 'segments' of the bacterium as a series of conical frusta.

The FtsZ and FtsW divisome assembly time (T_W and T_Z) is determined by monitoring the intensity profile along the centerline length over the cell cycle – step (4).

The last stage (5) provides a set of statistical tools to study the correlations between the parameters extracted and to measure their average and variance. The user can generate a scatter plot for each possible couple of parameters combination (e.g. the scatter plots in Figure 3). Moreover, the user can generate a violin plot for each parameter to inspect its statistical distribution over the entire population. To conclude the program computes the correlation coefficient of each couple of parameters.

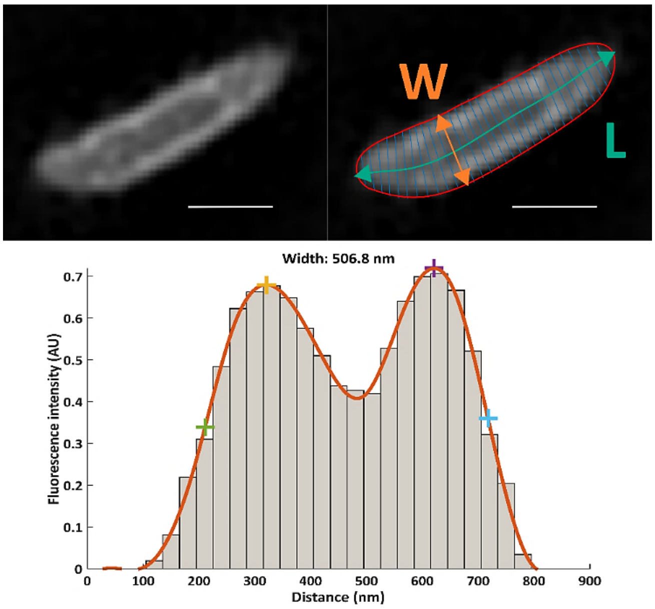

Figure 5-3 – Edge detection optimization. Cell shape slicing for edge detection and diameter measurement. The cell edges (green and blue cross) are identified thanks to the intersection of the histogram with a line passing at the half maximum high and parallel to the abscise. Scale bar correspond to 1µm.

5.2 Bacteria pole shape dynamics simulator

We observed that differences in constriction rate between WT and FtsW**I* *C. crescentus* cells lead not only to differences in cell size, but also in pole shape. Indeed, FtsW**I* cells exhibited blunter poles while WT cells have more tapered poles. To understand whether this difference can be directly set by the constriction rate and elongation dynamics at the constriction site, under the guidance of Dr. A. Lambert, we simulated, with a simplified interpretation, how the new two poles of a *C. crescentus* are geometrically built at the bacteria septum when the constriction starts. This qualitative simulator is based on the following hypothesis:

- when the constriction starts all the contributions to the elongation are given at the septum

- the elongation is dominated by an exponential process that is due to an insertion of peptidoglycan (PG) at the pole that is built up during the constriction
- the constriction is an iterative process that produce at each step, a new point, an elongation that can be approximated with a translation of each point of the constriction site and an inward constriction of the new last point.

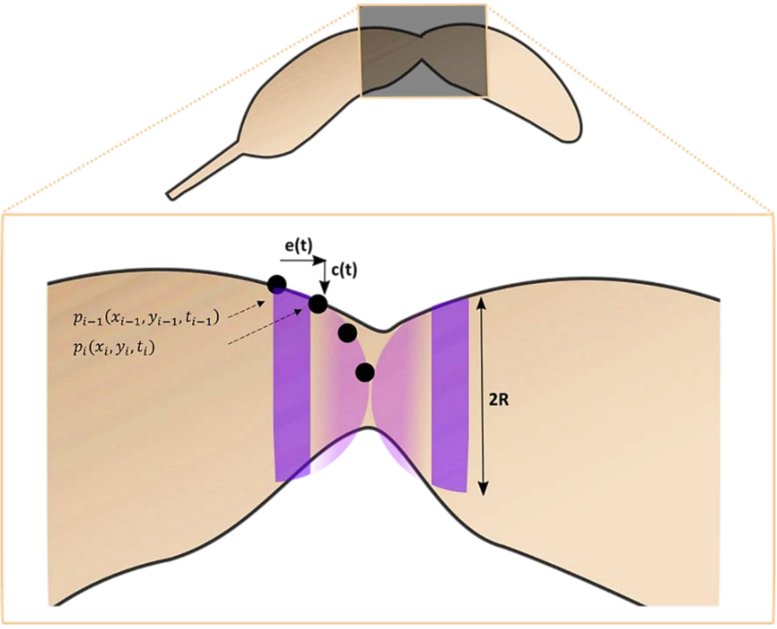

Figure 5-4 – Pole simulator model. The pole simulator translates each point at each growth iteration with two translation vectors: the elongation ***e***(t) and the constriction ***c***(t) vectors.

Thus, this simulator builds up the pole contour adding a new point that is translated from the last one using a constriction vector and an elongation vector:

- the constriction vector has a modulus depending on the derivative of the constriction function (increment) and a direction perpendicular to the bacteria length
- the elongation vector has a modulus depending on the number of points that have to be translated and on the derivative of the constriction function (increment) and it has a direction parallel to the bacteria length.

$$p_i(x_i, y_i, t_i) = p_{i-1}(x_{i-1}, y_{i-1}, t_{i-1}) + \vec{\boldsymbol{e}}(t_{i-1}) + \vec{\boldsymbol{c}}(t_{i-1}) \\ + \overrightarrow{p_{i-1}p_{i-2}} \qquad 5.1$$

$$\vec{\boldsymbol{e}}(t_i) = translational\ vector\ due\ to\ elongation$$

$$\vec{\boldsymbol{c}}(t_i) = translational\ vector\ due\ to\ contriction$$

$$\|\vec{e}(t)\| = \left\| \frac{dL(t)}{dt} \cdot \Delta t \right\| \quad [nm] \qquad 5.2$$

$$\|\vec{c}(t)\| = \left\| \frac{R_{max} dw(t)}{dt} \cdot \Delta t \right\| \quad [nm] \qquad 5.3$$

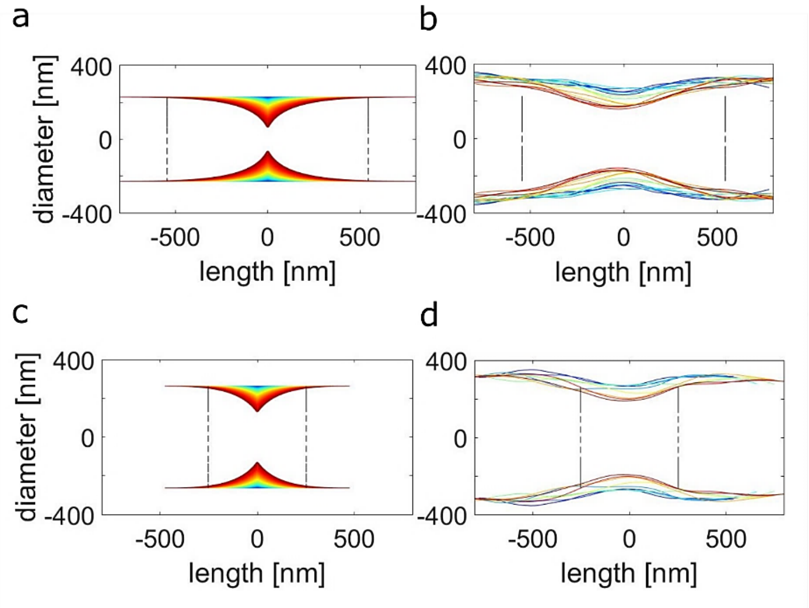

Figure 5-5 – Pole shape dynamics at the constriction site. a, and **c,** Qualitative simulation of the contour of a WT cell (**a**) and FstW**I* mutant (**c**) set by the constriction rate; **b,** and **d,** contour extracted from real SIM images of WT cell (**b**) and FstW**I* mutant (**d**); **c,** for simulated contour of a FstW**I* mutant, the pole result much blunter than the WT typical pole; the mutant and WT have different rates of constriction. This leads to difference in the duration of constriction and in the elongation during constriction. The contribution of a different duration and elongation during constriction between mutant and WT leads to a different pole shape simulated versus real data constriction contour. The color encodes the time of constriction.

As described in Chapter 3.2, the prediction of the constriction dynamics $c(t)$ can be based on Faingold approximation[147] of the diameter dynamics $w(t)$ given by equation 3.9 and thus equation 5.3 becomes:

$$\|\vec{c}(t)\| = \left\| R_{max}\left(1-\left(\frac{t-t_c}{t_g-t_c}\right)^2\right)^{-1/2} \cdot \Delta t \right\| \tag{5.4}$$

The elongation dynamics $l(t)$ has two contributions:

- the one due to the exponential growth (dominate one) (equation 3.1) and
- the one due to the "pole" elongation due to the fact that the septum surface is growing in 3D. This contribution is equal to $R_{max} - h(t)$ where R is the maximum diameter and h(t) is defined by equation 3.6.

Thus, the total elongation will be given by:

$$L(t) = R - h(t) + l(t) \tag{5.5}$$

and equation 5.2 becomes:

$$\|\vec{e}(t)\| = \left\| \left(\frac{-R}{t_g-t_c} + \lambda \cdot L_0 e^{\lambda t}\right) \cdot \Delta t \right\| \tag{5.6}$$

5.3 3D DH-PSF image reconstruction: StormChaser

In Chapter 2.3, we presented the current state-of-the art of software development for 3D DH-PSF molecule localization. However, we did not explain the historical evolution and the rational of our software development. When I initially started working on the development of a fast and easy to use DH-PSF algorithm under the guidance of Prof. S. Holden, the only open source available program was Easy-DHPSF[125]. Although, extremely friendly and easy to use, this approach was requiring about two hours for the full analysis of about 100,000 molecules on 128×128 pixels × 20,000 frames. Thus, our initial main goal was improving on the speed rather than on the localization precision. Only later, in the context of the SMLM Challenge 2016 where many efficient 3D localization approaches were developed, we tried to improve our approach through a multi-emitter solution that could account for the large DH-PSF limitation.

The speed limit in the Easy-DHPSF software performance is set by the first identification step, achieved via template matching, and the following double Gaussian fitting step. A template matching approach identifies every regions $s(x,y)$ within the input image $I(x,y)$ that looks like the dictionary of templates pattern $t_n(x,y)$. In this specific case, the template collection is a set of DH-PSF images extracted from the calibration step (Figure 5-6).

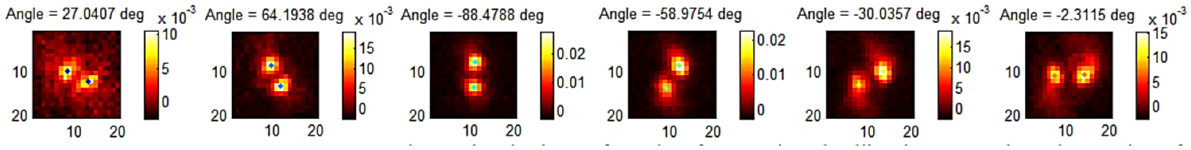

Figure 5-6 – DH-PSF template extraction. Each template is extracted from the calibration step. The lobes rotation angles encode the axial position. In this example the angle step between consecutive templates is about 30° (400 nm) and the full 180° range correspond to about 2 µm. Figure from [125].

To extract the template-image region matching position, the algorithm has to find the template position (p,q) that minimize the mean squared error – the squared sum of the difference between the image pixel signal and the template pixel signal:

$$e(p,q) = \sum_{x,y}^{N^{pix}} [(I(x,y) - t_n(x-p, y-q))]^2 \qquad 5.7$$

This operation is equivalent to compute the correlation coefficient for each pixel of the image. The phase correlation image is thus given by the convolution of the image $I(x,y)$ with every template $t_n(x,y)$:

$$r_n(p,q) = I(p,q) * t_n(-p,-q) \qquad 5.8$$

which in the Fourier space correspond to a simple multiplication:

$$r_n(x,y) = \mathfrak{F}^{-1}\left\{\mathfrak{F}\{I(x,y)\} \cdot \mathfrak{F}\left\{\overline{t_n(x,y)}\right\}\right\} \qquad 5.9$$

and can be further improved with a Gaussian spatial low pass filter:

$$r_n(x,y) = \mathfrak{F}^{-1}\left\{\mathfrak{F}\{\mathcal{G}(\mu_{x,y}, \sigma_{x,y})\} \cdot \mathfrak{F}\{I(x,y)\} \cdot \mathfrak{F}\left\{\overline{t_n(x,y)}\right\}\right\} \qquad 5.10$$

The molecule positions correspond to the correlation coefficient higher than a predefined threshold. Although, performing template matching in the Fourier space is faster than to evaluate the distance function for every pixel[172], this identification approach require many matrix convolution resulting in Easy-DHPSF-identification step as a process that is just half time faster than the more precise final fitting step.

To improve the speed, I proposed to develop a different identification step, to parallelize every possible process and to limit the free parameter space. We developed a complete pipeline (Figure 5-7) for fast multi-emitter fitting algorithm (STORMChaser) based on a double Gaussian analytical function. The software is open source and easy to use. The main pipeline stages of the software are: 1) PSF calibration; 2) fast first molecule guess and segmentation; 3) fast nearest neighbor search to group closest localization based on the *quadtree* algorithm and multi-emitter fitting; 4) post-processing molecule rejection; 5) rendering (super-resolution image, scatter plot histogram). The first molecule guess function is developed in c++ while all the other functions are implemented in Matlab with a parallel processing approach. The program takes as input a stack of raw SMLM images, a set of camera parameters (i.e. pixel size, gain, magnification factor, etc.), a set of experimental parameters (i.e. PSF size, FOV, etc.), and a set of output parameters.

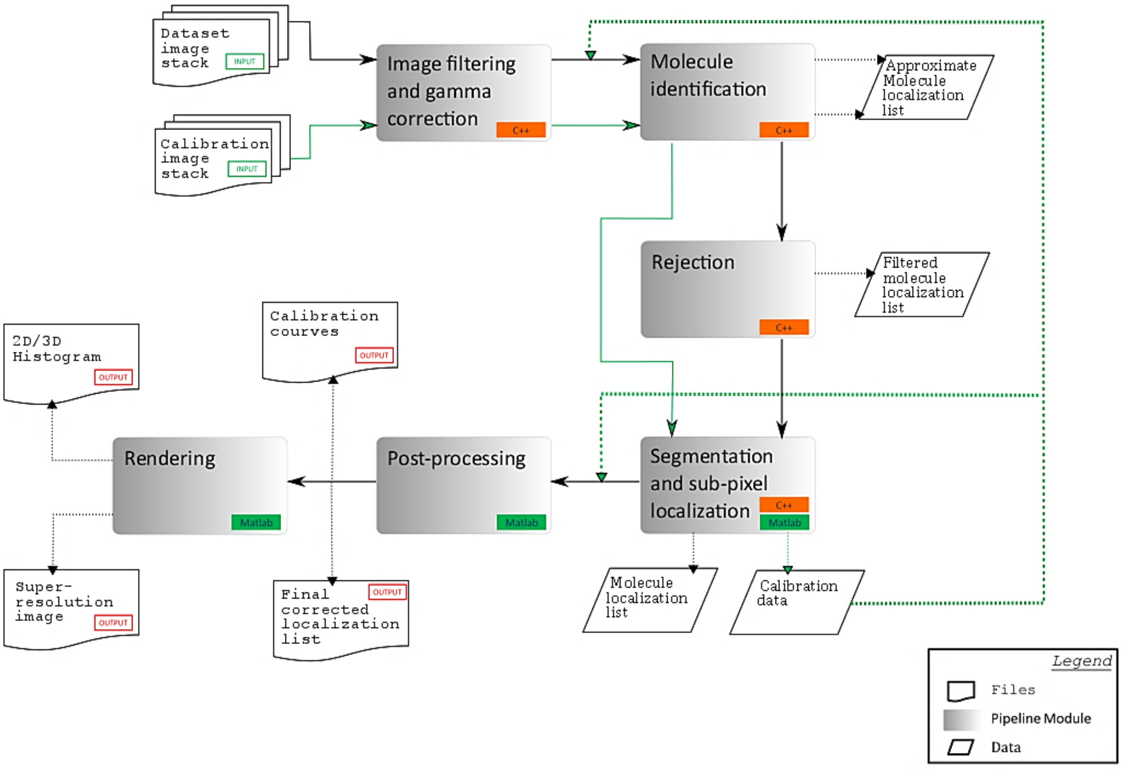
Dataset image stack
INPUT
Calibration image stack
INPUT
Image filtering and gamma correction
C++
Molecule identification
C++
Approximate Molecule localization list
Rejection
C++
Filtered molecule localization list
2D/3D Histogram
OUTPUT
Calibration courves
OUTPUT
Rendering
Matlab
Post-processing
Matlab
Segmentation and sub-pixel localization
C++
Matlab
Super-resolution image
OUTPUT
Final corrected localization list
OUTPUT
Molecule localization list
Calibration data
Legend
Files
Pipeline Module
Data

Figure 5-7 – STORMChaser program pipeline. The program performs a recursive fast identification step using different thresholds that it automatically updates using the images statistic and PSF boundary parameters extracted from the calibration step. After this initial search and rejection the segmented molecules images are ready to be accurately fitted via a multi-emitting algorithm or single emitter one depending on their positions. The final molecule list is then ready to be cleaned and prepared for the last step: the 3D rendering.

More specifically, (2) the algorithm computes a very fast first guess of the emitter positions based on a center of mass algorithm that recursively updates the search thresholds, subtracts the updated background and subtracts the pixel-clusters found to detect also the low signal molecules. The background subtraction step is essentially a temporal low pass filtering process that compute for every pixel the corresponding average background by averaging in time the pixel values that are far from the average value less than two time the variance root mean square. This molecule identification module is capable of identifying hundreds of thousands of molecules in few seconds.

The identification of each molecule lobe is based on a simple clustering algorithm. The algorithm searches for all the possible pixel seeds – the pixels that can potentially generate a cluster of pixels with specific properties (such as area range and seed intensity threshold). Then, the algorithm associates to each seed the neighbor pixels satisfying certain properties (such as distance from the seed and cluster intensity threshold) and the neighbor of the neighbor pixels until a distance condition is achieved. To avoid checking twice whether a pixel belong to the cluster, the algorithm generate a bit image matrix to associate a flag equal to one to the pixel that has been already associated to the cluster.

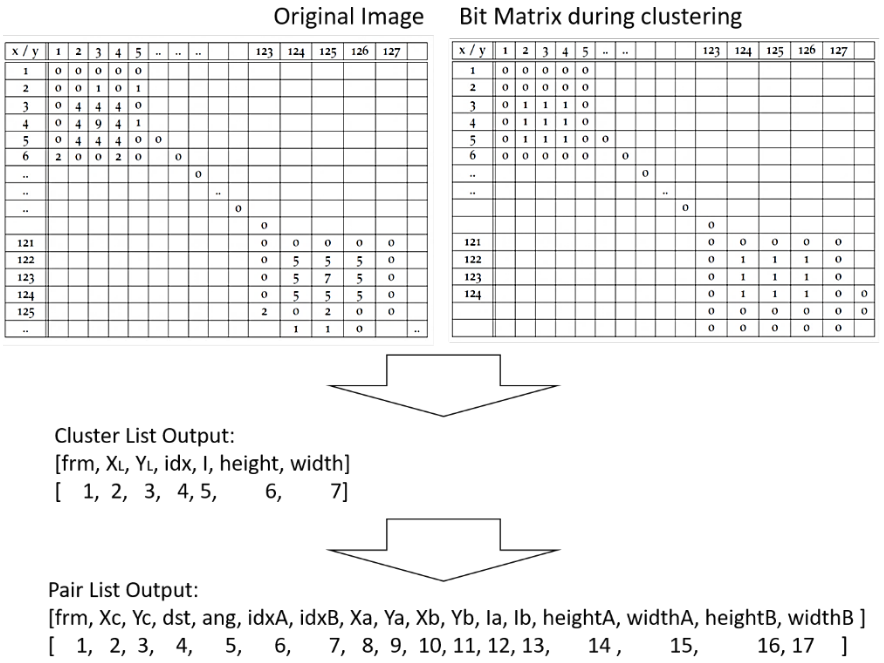

Original Image

x / y	1	2	3	4	5	..	..	..			123	124	125	126	127	
1	0	0	0	0	0											
2	0	0	1	0	1											
3	0	4	4	4	0											
4	0	4	9	4	1											
5	0	4	4	4	0	0										
6	2	0	0	2	0		0									
..								0								
..									..							
..										0						
											0					
121											0	0	0	0	0	
122											0	5	5	5	0	
123											0	5	7	5	0	
124											0	5	5	5	0	
125											2	0	2	0	0	
..												1	1	0		..

Bit Matrix during clustering

x / y	1	2	3	4	5	..	..				123	124	125	126	127	
1	0	0	0	0	0											
2	0	0	0	0	0											
3	0	1	1	1	0											
4	0	1	1	1	0											
5	0	1	1	1	0	0										
6	0	0	0	0	0		0									
..								0								
..									..							
										0						
											0					
121											0	0	0	0	0	
122											0	1	1	1	0	
123											0	1	1	1	0	
124											0	1	1	1	0	0
											0	0	0	0	0	0
											0	0	0	0	0	

Cluster List Output:
[frm, X_L, Y_L, idx, I, height, width]
[1, 2, 3, 4, 5, 6, 7]

Pair List Output:
[frm, Xc, Yc, dst, ang, idxA, idxB, Xa, Ya, Xb, Yb, Ia, Ib, heightA, widthA, heightB, widthB]
[1, 2, 3, 4, 5, 6, 7, 8, 9, 10, 11, 12, 13, 14 , 15, 16, 17]

Figure 5-8 – Molecule identification step is based on clustering algorithm. The algorithm first identifies the cluster seed and then associates to every seed the pixel belonging to the cluster. The algorithm finally output the pair of cluster corresponding to the molecule lobes first guess.

The first guess molecule list is then ready to enter the third step (3) where closest molecules are grouped and fitted together using a multi-Gaussian function that tunes the number of free parameters accordingly with the number of molecules that have to be simultaneously fitted (up to 4). Finally (4-5), the molecules with a bad fitting quality, a bad estimated localization precision (dependent on the estimated number of photons) or a bad PSF shape (out of statistic collected from the images and calibration) are rejected. The filtering is done based on statistical information retrieved in the previous step of the software code. The final list of localizations is then saved and the resulted super-resolved image is displayed by using image rendering library (DIP*image*) or via a 3D scatter plot.

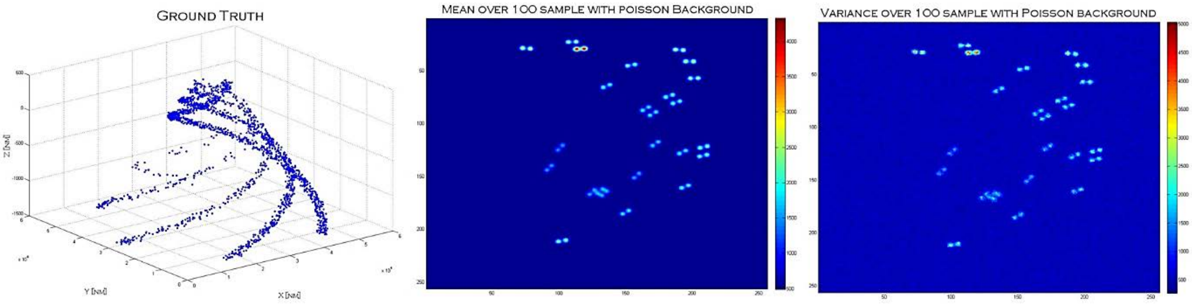

Figure 5-9 – Artificial DH-PSF dataset. The simulator associates a simulated DH-PSF to every artificial molecule position and to each pixel the corresponding Poisson noise.

To test the STORMChaser we first created a simulator of DH single molecule dataset with Poisson noise. The simulator generates DH-SPF single molecules synthetic dataset starting from the active fluorophores positions on a 3D artificial shell taken from the EPFL Collection of reference datasets[1].

The artificial dataset (Figure 5-9 – Artificial DH-PSF dataset.Figure 5-9) where generated with different average intensities for emitter and Poisson noise level. We expected a theatrical pair localization precision in x-direction from the propagation of error starting from the localization precision of each lobe [121] :

$$\sigma^2(\theta_x) = \left(\sigma_{PSF}^2 + \frac{a^2}{12}\right) \cdot \left(\frac{16}{9} + 8\pi \cdot \left(\sigma_{PSF}^2 + \frac{a^2}{12}\right) \cdot \frac{b^2}{N \cdot a^2}\right) \qquad 5.11$$

Our first preliminary result seemed promising and we decided to further test the program with more realistic artificial dataset in the context of the SMLM challenge 2016. The results are shown in Table 5-1, Figure 5-10 and Figure 5-12. The table is comparing the recall (the number of true positive molecules identified by the software divided by the total number of the actual molecules), the precision (the number of true positive divided by the total number of molecules detected by the program), the root mean squared error (RMSE) in x, y and z, and the total time necessary to detect all the molecules.

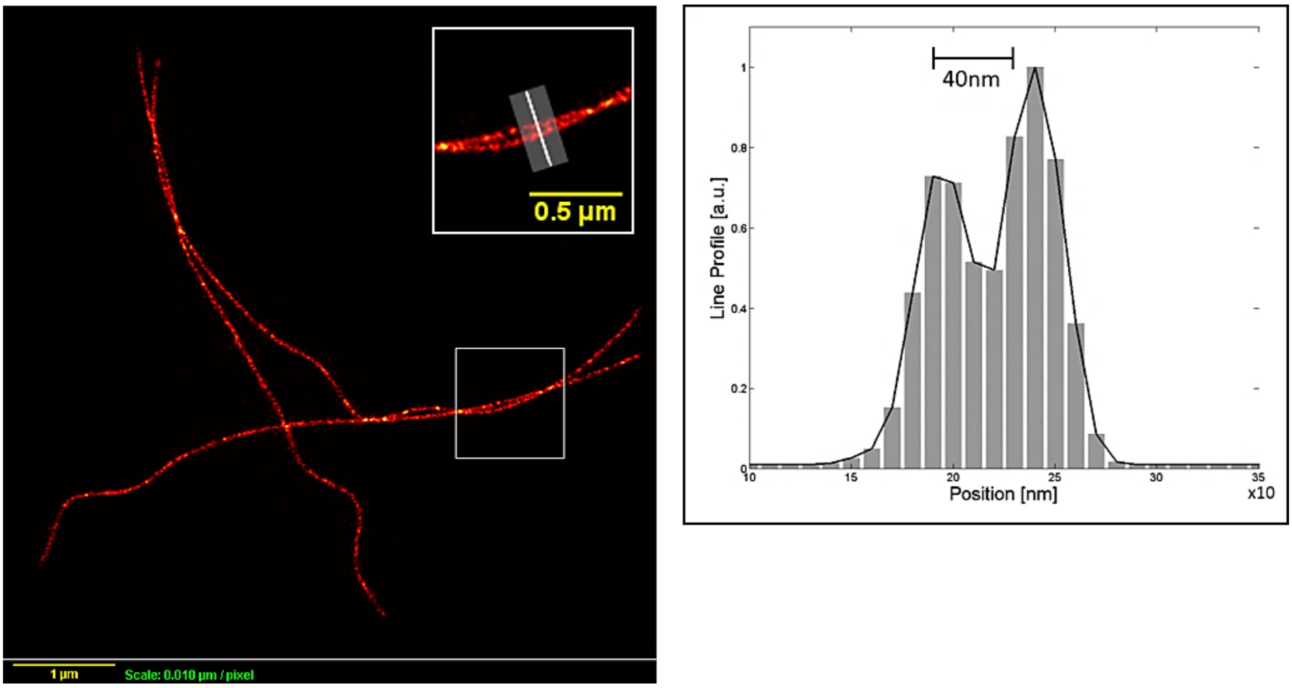

Figure 5-10 – STORMChaser rendering. The image shows the rendering of simulated data generated for the SMLM challenge 2016.

The visualization tools of the results of the 3D SMLM Challenge 2016 have been for us a useful investigation tool to identify the possible causes of our bad recall value (see Chapter 2.3 for recall index definition). Indeed, from the comparison results of STORMChaser against Easy-DHPSF and the beast in class CSpline we could observe an evident problem in the localization of the molecule located in the negative axial range (Figure 5-11). Thus, our next step should have been to deeply debug the code with molecule placed in the negative axial range. However, since during the 3D SMLM Challenge 2016, other valid approaches were developed for efficient DH-PSF dataset analysis, we were not motivated to improve further our algorithm.

---

[1] http://bigwww.epfl.ch/smlm/datasets/index.html

SOFTWARE	DATASET	RECALL: TP/TP+FN	PREC: TP/TP+FP	RMSE XY [NM]	RMSE Z [NM]	TIME [S]
Easy-DH	LD N1	0.775	0.993	33.525	26.105	1447 (24 min)
CSpline	LD N1	0.946	0.958	33.216	31.399	732
STORMC	LD N1	0.462	0.996	25.691	26.146	300

Table 5-1 3D DH-PSF software comparison at the SMLM Challenge 2016. The programs are tested by using simulated dataset generated for the SMLM challenge 2016 competition. The table shows that my software still has a low recall problem even though is fast and precise.

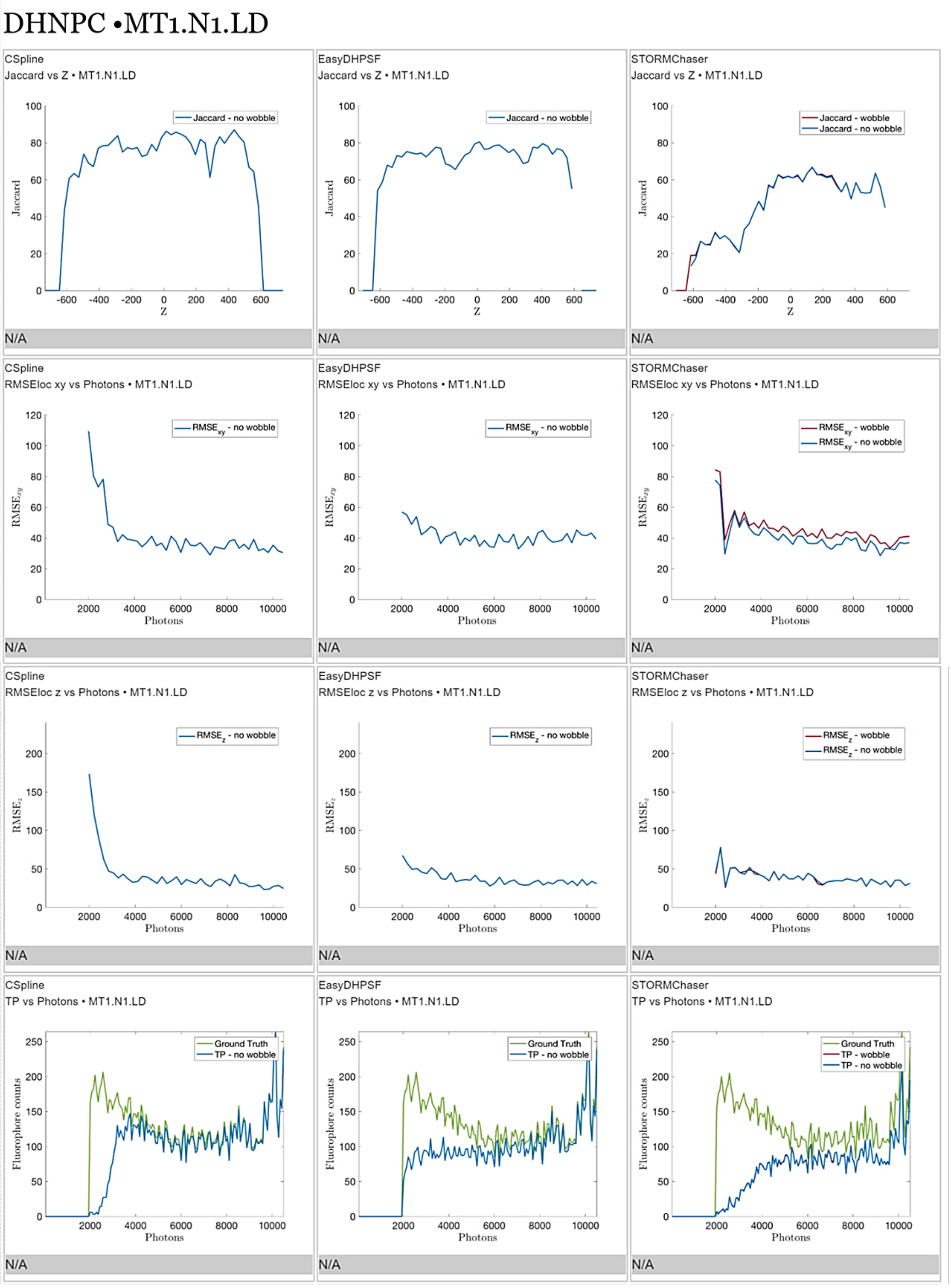

Figure 5-11 – 3D SMLM Challenge result comparison. Comparison between the best in class software (CSpline), with the first DH-PSF open source available software and STORMChaser. Comparison between Jaccard index versus axial range, RMSE in the x-y plane and in the axial direction versus molecule photons signal and number of true positive versus number of photons. STORMChaser present a problem in detecting molecules in the negative axial range that could be simply the result of an underling software bug.

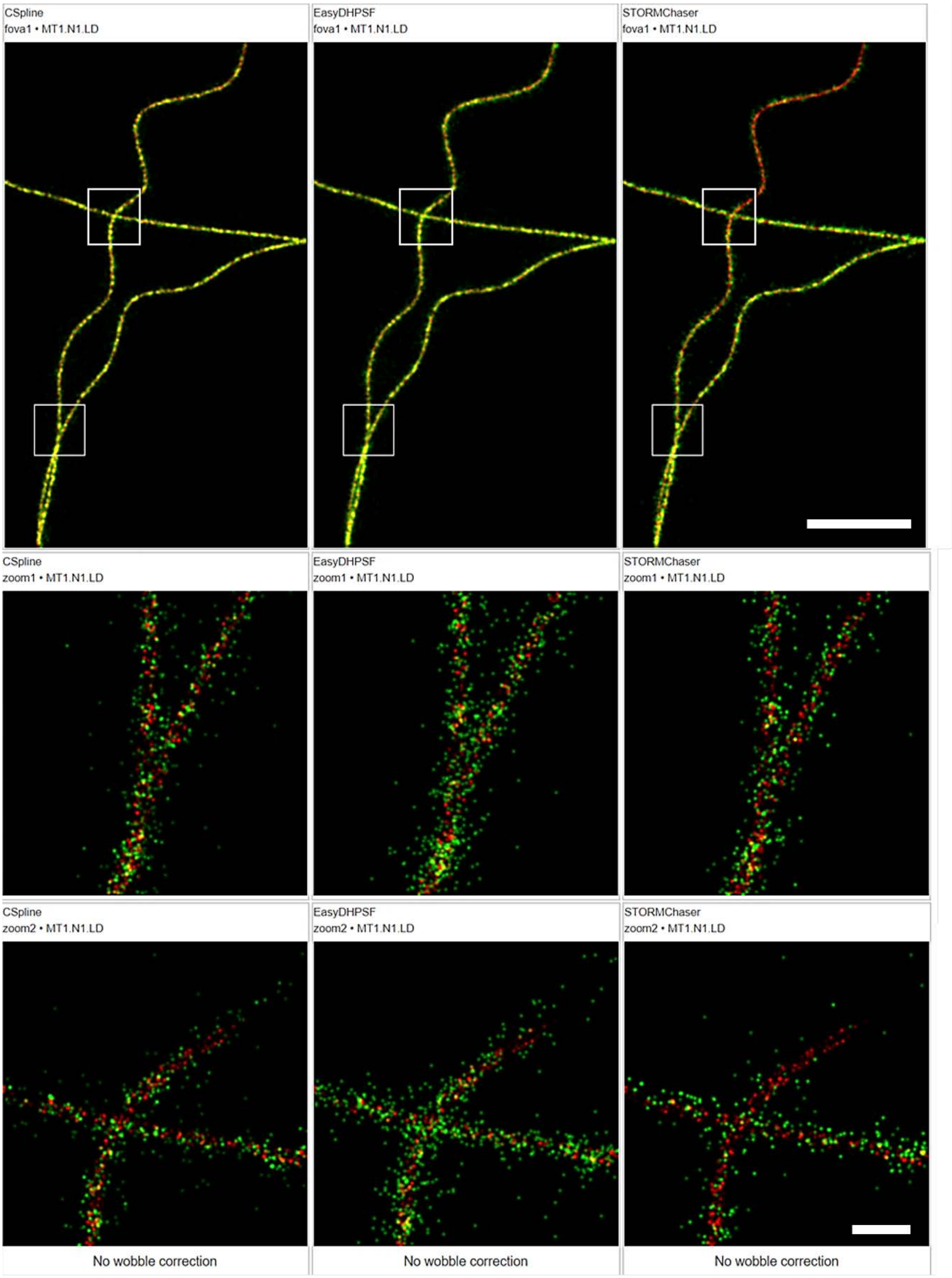

Figure 5-12 – 3D SMLM Challenge image result. Rendering comparison (first top line) between the best in class software (CSpline), the first DH-PSF open source available software and STORMChaser. Central and last rows are to the magnified view corresponding to the white rectangles. In rad the ground true. Image colors: red, ground truth; green, software results. Scale bar 500 nm.

6 Large flat field STORM

In Chapter 2.1 we investigated why the global and local uniformity in the sample illumination is critical for SMLM images quality. In this Chapter, I will first summarize how we achieved large and uniform epi-illumination[70] and later on, I will focus on my specific contributions to this project: the characterization of the CMOS camera and the test of a specific SMLM software which takes into account the camera characteristics to reconstruct the super-resolved image[173].

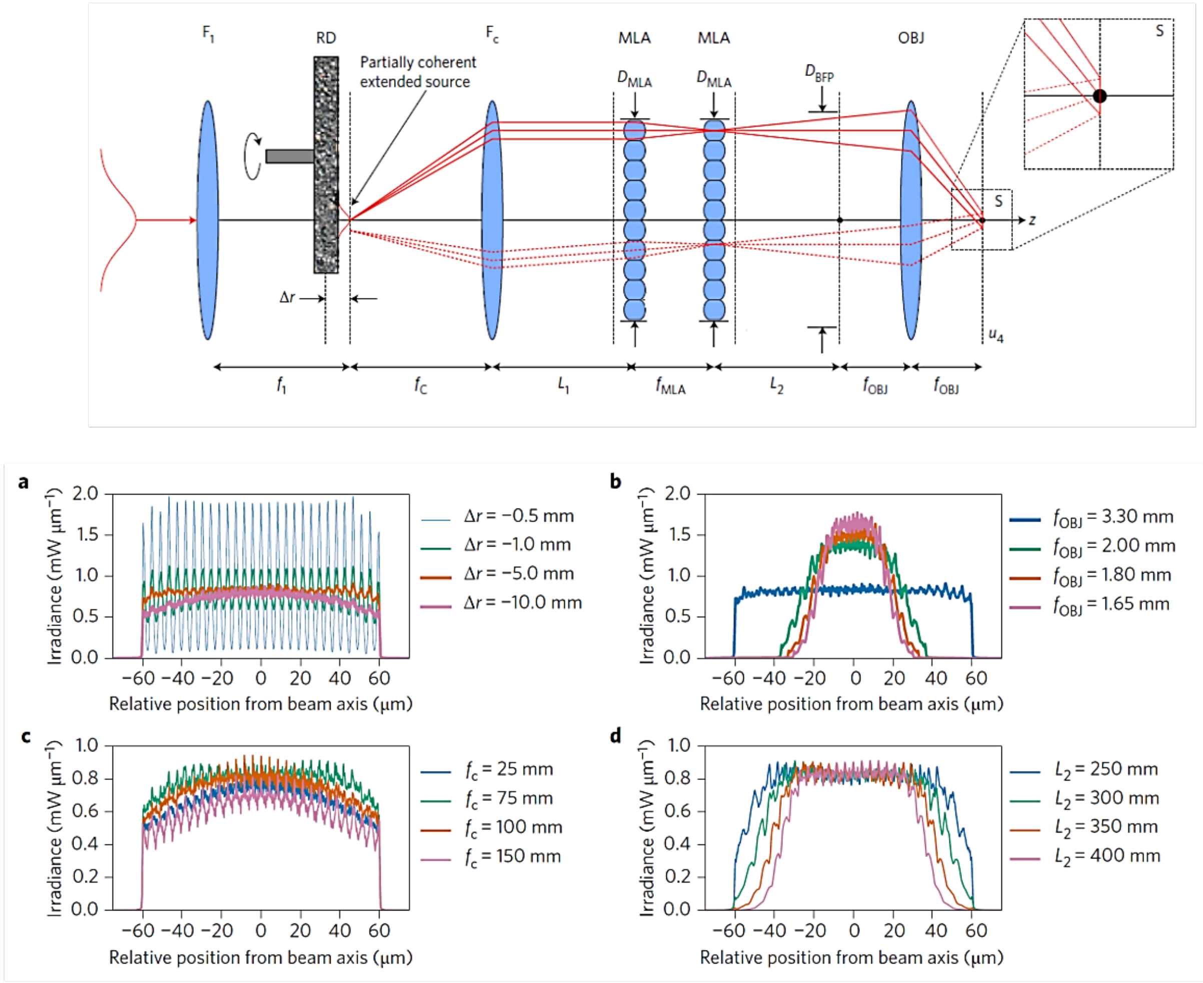

Figure 6-1 – Dependence of the illumination homogeneity on the design parameters. Simulated 1D sample plane irradiance profiles through the centre of the illuminated region. **a,** The offset of the rotating diffuser Δr has an optimum position that reduces the modulation in the grating pattern and prevents overfilling the microlens arrays (MLAs). **b,** The objective lens focal length f_{OBJ} largely determines the size of the sample plane irradiance. **c,** The focal length of the collimating lens f_c for the partially coherent source controls both the field homogeneity and the spatial coherence of the source, as evidenced by the modulation depth of the grating fringes. **d,** The distance between the second MLA and the objective (L_2) must be small to prevent overfilling of the objective. Simulation code developed by K. Douglass. Simulation performed by K. Douglass. Figure taken from [70].

To achieve high-quality wide-field super-resolution fluorescence imaging, we developed a low-cost microlens array-based system — flat illumination for field-independent imaging (FIFI) — that can efficiently and homogeneously perform simultaneous imaging of multiple cells with nanoscale resolution. Beyond imaging a larger field of view, FIFI serves as a simple, low-cost solution for fully exploiting the large sensor formats of new sCMOS cameras for SMLM.

FIFI (Figure 2-3 b) is an extension of a Köhler integrator that combines a beam-shaping modulus with a high-efficiency diffuser. Moreover, the system description provides critical and detailed hints to guide in a customizable illumination[174]. For example, the diffuser position relative to the telescope lens focal plane sets the final beam size and the spatial coherence of the source. The diffuser position as well as the objective focal length and the back focal plane (BFP) diameter are also critical for both uniformity and power of the illumination (Figure 6-1).

A more detail explanation of the Köhler integrator system can be found in Chapter 2.1.

6.1 CMOS camera noise and characterization

In Chapter 4.1 we explored which parameters of the camera sensor could be critical for the quality of the reconstructed image and why, in the SMLM field, CMOS commercial cameras have been replacing the more expensive commercial EMCCD. Indeed, several factors related to the camera characteristics, such as the sensitivity (quantum efficiency), readout speed of the camera and the number of pixels in the chip contribute to define the temporal and spatial resolutions of the final super-resolved image. For example, the pixel readout speed becomes a crucial parameter when thousands of raw images has to be collected to reconstruct one single FOV. Higher readout can affect both the frame rate and the FOV size by setting either higher number of pixels at the same frame rate or higher frame rate with the same number of pixel than a camera with lower readout.

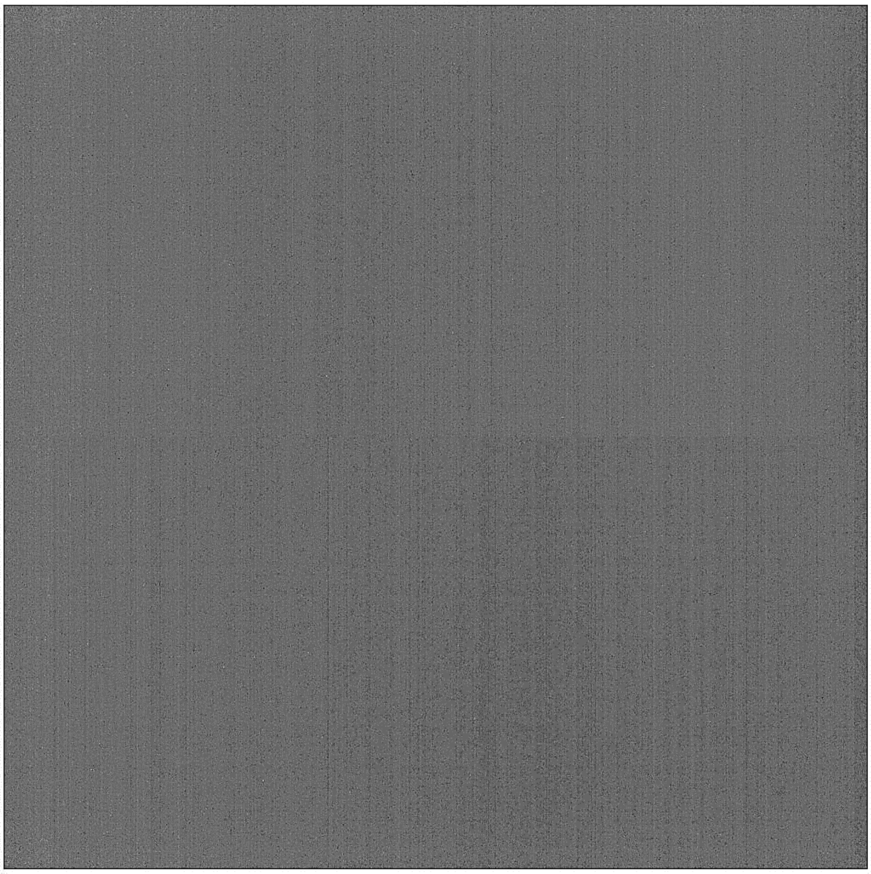

Figure 6-2 – sCMOS Zyla 4.3 Andor dark image. The image acquired in a dark condition setting show the typical "salt-and-paper" and "bar-code" effect characteristic of the CMOS camera noise.

CMOS cameras have a sensor with a generally high number of pixel (more than 5.5 Mega-pixels) camera and an extremely high readout speed (up to 560MHz [2]). However, as previously explained, CMOS camera has a pixel dependent noise and a specific gain. As a consequence the major pixel figures (such as pixel gains) related to the noise have to be characterized.

From previous CMOS characterization works[66], we expected a large number of tailing pixels in the noise distribution of the CMOS-pixels which results in a randomly distributed bright and dark pixels on the image: the characteristic CMOS "salt-and-pepper noise". Moreover, we expected a further "bar-code effect" across the image – different levels of dark gray intensity at random spacing[175] – corresponding to the variability from ADC column to column convertor (Figure 6-2).

Finally, we expected to identify a fixed pattern noise, a map of pixels that appear as bright pixels in both presence and absence of photons (in a dark acquisition setting)[176]. These extremely bright pixels corresponds to malfunctioning pixels: the "hot pixels".

To characterize the sCMOS camera, under the guidance of Dr. K. M. Douglass, I developed a MATLAB routine that recursively loads and reads dark images and stacks of images at different intensities, computes the gain solving the minimization problem explained in Chapter 4.1 and extract the noise for each pixel of the camera (Figure 6-3).

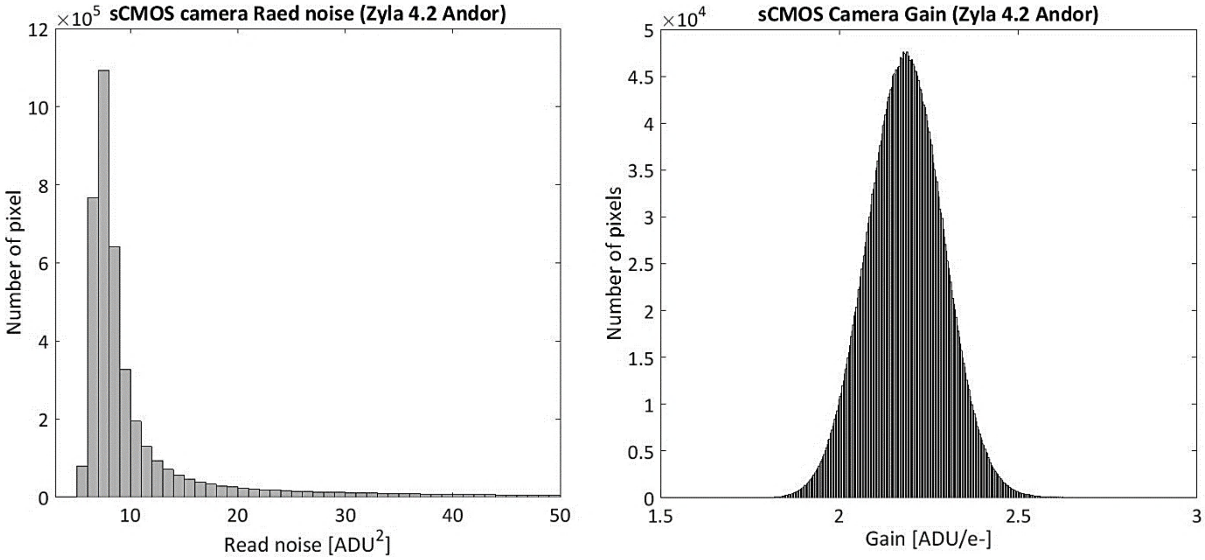

Figure 6-3 – sCMOS Zyla 4.3 Andor read noise and gain distribution. The read noise map present the characteristic CMOS not Gaussian distribution with a long tail. The Gain distribution is centered around a mean value of 2.2 [ADU/e-] with a variance root square of 0.3 [ADU/e-].

Interestingly, we found a straightforward way to extract the hot-pixel map by forcing the gain computation for all the camera pixels. Indeed, the pixel gain distribution exhibits a double Gaussian distribution: the first most populated Gaussian distribution is centered on the expected mean gain value and the second one, much less populated, is offset from the mean value. The hot pixels are exactly the pixels lying in this second Gaussian distribution offset from the central one (Figure 6-4).

After having compute the read noise and the gain for each pixel, we measured the mean value for the main parameters which characterize our sCMOS camera. The values found (Table 6-1) are in agreement with the one reported in the specifications[3]. The mean read noise reported is 1.1 $[e^-]$ and we estimated:

---

[2] http://www.andor.com/scientific-cameras/neo-and-zyla-scmos-cameras/zyla-42-plus-scmos

$$\sigma_R[e^-] = \frac{read\ noise\ [ADU]}{gain} \sim \frac{\sqrt{8}}{2.2} \sim 1.3[e^-]$$

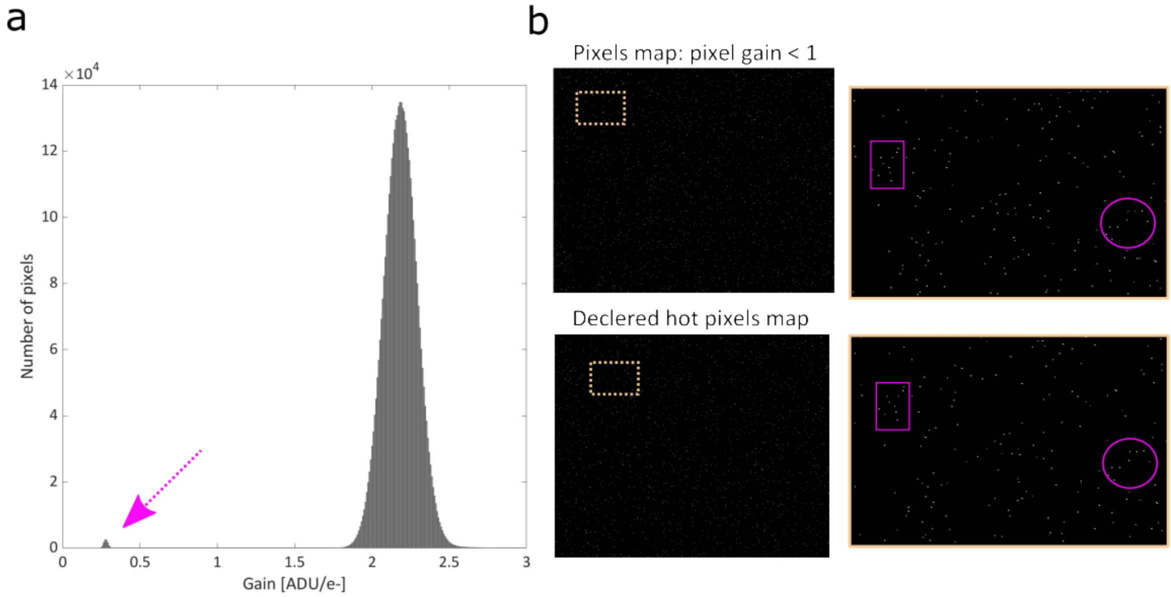

Figure 6-4 – Hot pixels identification process. **a,** The gain distribution presents a second Gaussian distributions offset from the most populated one. The non-meaningful gain distribution, with mean value less than one, corresponds to the hot-pixel distribution. **b,** The pixel with a gain less than one correspond to the hot pixels declared by the vendor.

Measured camera characteristics

$\overline{o(x,y)}$ = *<Offset>*	$\sigma_R^2 = E[\sigma_o^2]$	$\overline{g(x,y)}$ = *<Gain>*	$\sqrt{\sigma_g^2}$
~100 [ADU]	~8 $[ADU^2]$ (peak)	~2.2 [ADU/e-]	~0.3 [ADU^2/e-^{2}]

@ 50ms integration time, 560 MHz readout clock

Table 6-1 sCMOS Zyla 4.3 Andor characterization. Average offest, read-noise and gain values.

---

[3] http://www.andor.com/scientific-cameras/neo-and-zyla-scmos-cameras/zyla-42-plus-scmos

6.2 Maximum Likelihood Localization Estimation (MLE)

In Chapter 2.3 we defined the MLE in the context of SMLM. We also investigated why the identification of the possible sources of noise (such as signal shot noise and camera noise) is critical for a proper construction of the likelihood function and thus for the molecules accurate localization.

Camera noise is particularly problematic when imaging with CMOS camera (Chapter 4.1) and in the presence of low signal. In this context, the Poisson shot-noise is not anymore the sole dominant factor. Indeed, at low signal (of the order of hundreds of photons), the Gaussian readout noise of a CMOS camera competes with shot noise[177]. Moreover, CMOS read-noise and gain contributes differently across different pixels making their treatment even more relevant for a precise sub-pixel molecule localization.

Thus, for our flat-field epi-illumination CMOS-based STORM system[70], we considered adopting a CMOS-specific SMLM program based on a MLE algorithm [173]. The software takes as input the raw images together with the specific camera noise and gain pixel matrix. A MLE-sCMOS-specific routine is then launched in a highly parallelized graphical processor unit (GPU) environment using Compute Unified Device Architecture (CUDA):

Knowing that the probability distribution of the sum of two independent random variables is given by the convolution of their individual distributions, then a likelihood-sCMOS-specific function is given by the convolution of the Poisson-distributed photon shot noise with the pixel-dependent Gaussian noise distribution:

$$\mathcal{L}(\boldsymbol{\theta}, \mathbb{D}) = \prod_{x,y \in \mathbb{D}} \sum_{x,y \in \mathbb{D}} \frac{PSF(x,y \mid \boldsymbol{\theta})^{I} e^{-PSF(x,y \mid \boldsymbol{\theta})}}{I!} \frac{1}{\sqrt{2\pi\sigma_R^2}} e^{-\frac{(I_{ADU} - I \cdot g - o)^2}{2\sigma_R^2}} \tag{6.1}$$

where $\sigma_R^2(x,y)$ is the expected value of the variance of the offset, $o(x,y)$ is the mean offset, $g(x,y)$ is the pixel gain, $I(x,y)$ is the detected image intensity and $PSF(x,y \mid \boldsymbol{\theta})$ the PSF model (see equation 2.25).

However, to limit the computational cost of performing such a convolution for each pixel during every fitting iteration, the authors of [66] developed an analytical approximation that greatly simplified the calculation while providing optimal accuracy and precision at the theoretical limit[66]:

$$\mathcal{L}(\boldsymbol{\theta}, \mathbb{D}) = \prod_{x,y \in \mathbb{D}} \frac{\left(PSF(x,y \mid \boldsymbol{\theta}) + \frac{\sigma_R^2}{g^2}\right)^{\tilde{I}} e^{-PSF(x,y \mid \boldsymbol{\theta}) + \frac{\sigma_R^2}{g^2}}}{\Gamma(\tilde{I} + 1)} \tag{6.2}$$

where Γ is the Gamma function and

$$\tilde{I}(x,y) = \frac{I_{ADU}(x,y) - o(x,y)}{g(x,y)} + \frac{\sigma_R^2(x,y)}{g^2(x,y)} \tag{6.3}$$

Thus, from the likelihood function $\mathcal{L}(\boldsymbol{\theta}, \mathbb{D})$ we can then extract the parameter estimate $\widehat{\boldsymbol{\theta}}$:

$$\widehat{\boldsymbol{\theta}} = \arg\max_{\boldsymbol{\theta}} [\ln \mathcal{L}(\boldsymbol{\theta}, \mathbb{D})] \tag{6.4}$$

$$\widehat{\boldsymbol{\theta}} = \arg\min_{\boldsymbol{\theta}}\left[-\ln \prod_{x,y\,\in\,\mathbb{D}} \frac{\left(PSF(x,y\mid\boldsymbol{\theta})+\frac{\sigma_R^2}{g^2}\right)^{\tilde{I}} e^{-PSF(x,y\mid\boldsymbol{\theta})+\frac{\sigma_R^2}{g^2}}}{\Gamma(\tilde{I}+1)}\right] \qquad 6.5$$

Any parameter of molecule signal distribution, such as the molecule position (θ_x, θ_y), maximum amplitude θ_N, variance ${\theta_\sigma}^2$, background θ_b, can be then estimated with a maximum precision up to[66,120]:

$$\Delta\theta \geq \sigma_{CRLB}^{CMOS} = 1/I(\theta_i) = 1/\sum_{p=1}^{PixN} \frac{1}{N_p + \frac{\sigma_{N_p}^2}{g_p}} N_p''(\theta_i) \qquad 6.6$$

where N_p , $\sigma_{N_p}^2$ and g_p are the expected photon number, variance anche gain in the pixel *p*.

To test the CMOS specific algorithm, I used ThunderSTORM [178] to generate many ground-truths and corresponding 2D SM dataset with the different numbers of photons per emitter. Finally, I compared the performance of the sCMOS specific software with the result achieved with a non-specific CMOS algorithm (rapidSTORM[179]) using the artificial dataset and known ground-truth. We found, as expected, a localization precision of about 10nm with about 1000 photons/emitter (Figure 6-5).

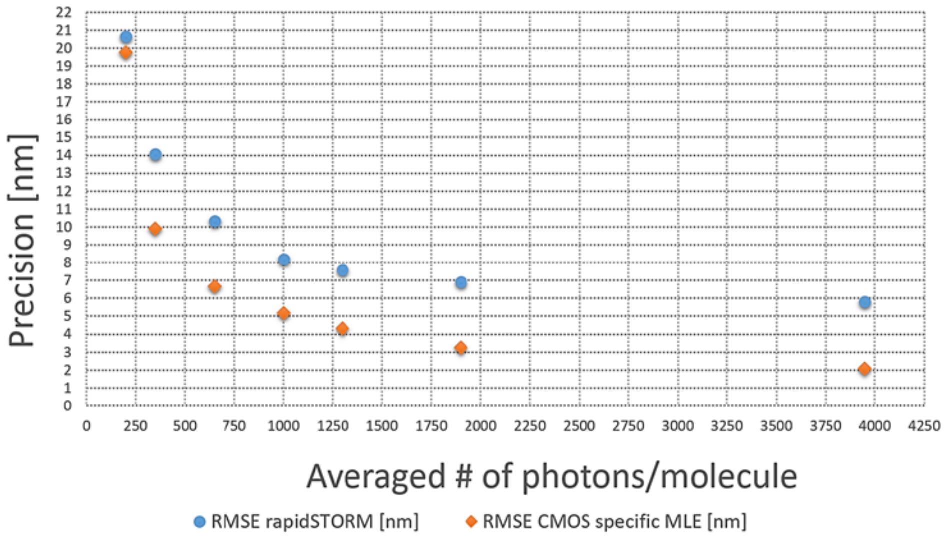

Figure 6-5 – CMOS-specific-MLE algorithm and rapidSTORM software comparison. Artificial datasets were generated adding the CMOS camera noise to simulated data via ThunderSTORM to test and confirm the best results achieved with an algorithm accounting for the pixel-dependent noise and gain.

The throughput large and uniform FIFI-based microscope combined with the high frame rates of sCMOS cameras, is capable of performing STORM on multiple eukaryotic cells (1–3 COS-7 cells – Figure 6-6).

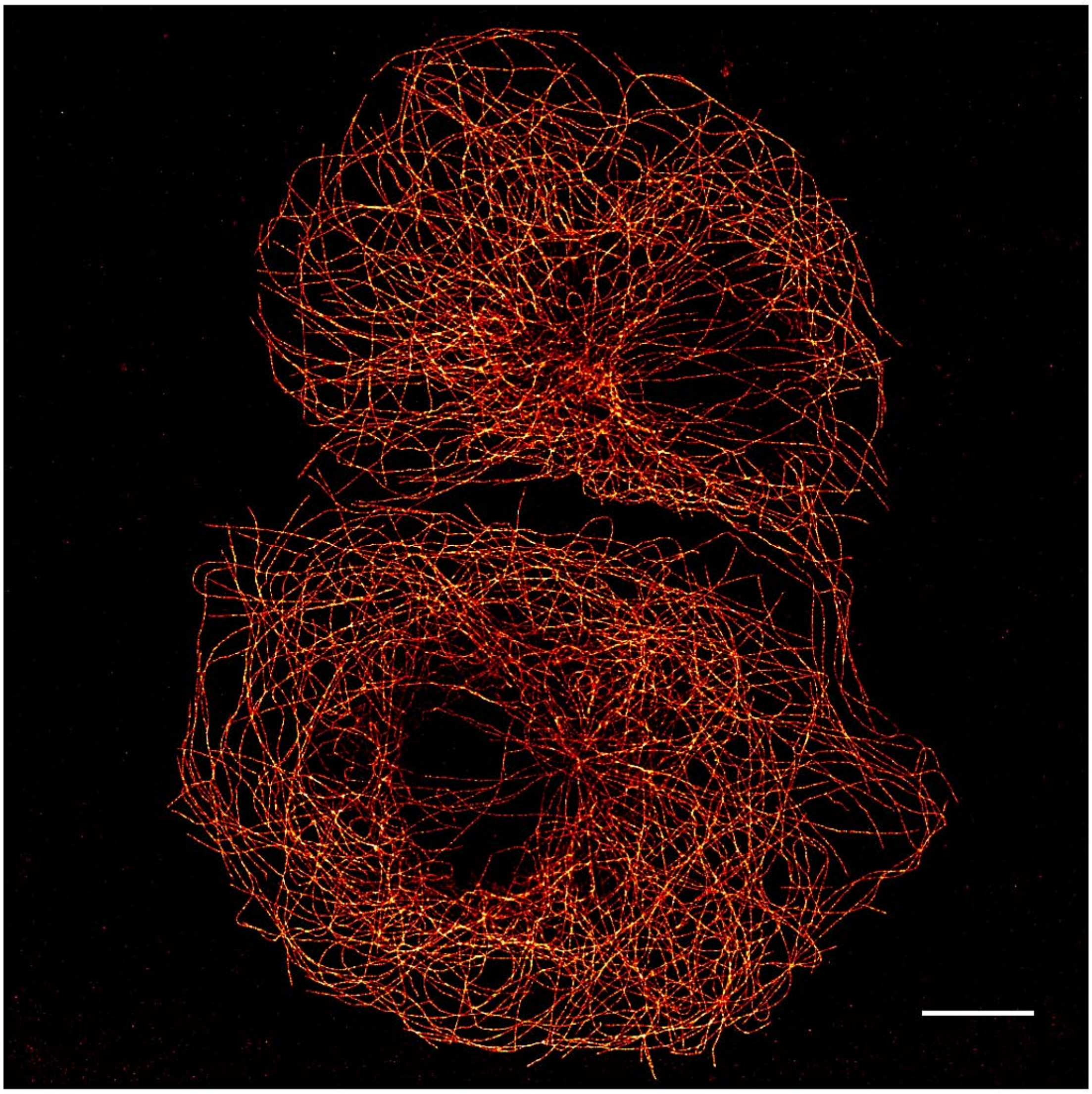

Figure 6-6 – Large FOV STORM imaging of multiple eukaryotic cells. STORM image of microtubules in COS7 cells. Cells were labelled with antibodies against α-tubulin and secondary antibodies conjugated with AlexaFluor 647. Scale bar 10 µm. Experiment, imaging and image processing performed by C. Sieben. Figure taken from [70].

7 Large flat field waveguide-PAINT

In Chapter 1.1.3, we presented the working principle of DNA-PAINT and we explained why such approach among all SMLM approaches is one of most promising for combining high resolution and multiplexing. We also presented the drawbacks (the background signal generated by the fluorophores in solution and the long acquisition time necessary to acquire enough binding-unbinding events) of this method and how they could be addressed by developing a platform for large and uniform optical sectioning illumination.

Afterwards, we investigated (Chapter 2.2) the existing strategies to achieve optical sectioning illumination. Moreover, we described why a waveguide-TIRF approach is a good candidate to excite multiple targets close to the surface of the sample support. A waveguide-based evanescent field is generated by the light guided in a thin layer (waveguide core) with a refractive index higher than the aqueous solution and the bottom cladding layer. The light undergoes total internal reflection at the interface between the core and cladding producing an optical sectioning illumination of the DNA-PAINT-target that lies on the waveguide core surface. The WG-based TIRF illumination will excite only the dye-labeled oligonucleotides (imager strands) close to the target (tagged with docking strands) avoiding the production of strong background from the unbounded imager strands.

Here we present the main challenges concerning the waveguide chip development, the chip holder design and their integration in a custom made microscope. Finally, we will present the results achieved with our waveguide-PAINT system.

7.1 Waveguide Chip design

The waveguide design involves first the choice of the waveguide core and cladding, second the definition of the waveguide core and cladding geometry and finally the choice of the proper waveguide input shape.

As mentioned in Chapter 2.2.1, previous demonstrations of waveguide-TIRF platforms were made with either low or high refractive index contrast waveguides (LIC or HIC). Low refractive index contrast waveguides were realized with a PMMA core[57] and a cladding material index-matched to the sample solution - an amorphous perfluorinated optical polymer (Cytop). High-index waveguide cores were instead fabricated from either tantalum pentoxide (Ta_2O_5)[56,94] or silicon nitride (Si_3N_4)[60,95]. Low refractive index contrast waveguides can potentially produce a sample excitation at higher depth. On the other hand HIC waveguides strongly confine the propagating electric field (the waveguide mode), which can reduce propagation losses. However, the increased mode interaction at the core-cladding interface results in enhanced losses due to scattering where surface roughness is present[96,97]. Moreover, HIC waveguides can suffer from high coupling losses, mainly due to back-reflections, mismatches between the electrical field properties of the input source and the waveguide mode, and excitation of modes which are not confined to the waveguide core (the radiation modes)[98–100]. Nevertheless, we fabricated our waveguide chip using Si_3N_4 processing due to the maturity of the process and the know-how readily available within the Photonics Integrated Circuit (PIC) field, where low propagation losses have become a central requirements for on-chip waveguides[101–106]. In defining the waveguide fabrication process, we tried to limit the possible sources of scattering and absorption losses (limiting the core and cladding roughness, input facet roughness and depositing a protective top cladding). Moreover, we optimized the waveguide input for efficient coupling. Finally, we designed the waveguide geometry to have uniform field distribution on a wide (inherently multimode) waveguide essential for achieving large FOV illumination.

We fabricated channel waveguides in the EPFL Center of Micro-Nanotechnology (CMi). The waveguides were realized with a rectangular cross-section using Si_3N_4 as the core and SiO_2 as the cladding material (Figure 7-1 a). The 2 µm SiO_2 cladding layer of refractive index $n_1 \sim 1.47$ at λ=647nm was grown by thermal oxidation of the silicon (Si) substrate followed by the 150 nm thick Si_3N_4 core layer ($n_1 \sim 2.04$ at λ=647nm) high stress low-pressure chemical vapor deposition (LPCVD). Our observations showed that cores formed from stoichiometric silicon nitride with high internal stress give much higher coupling and transmission efficiency in comparison to non-stoichiometric low-stress silicon nitride, likely due to absorption and scattering on impurities and defects in its structure, which are significantly more numerous in the case of non-stoichiometric SiN_x films.

Since losses are strongly affected by the surface roughness produced during etching steps, we adopted a two-step lithography and dry reactive ion etching process designed to minimize damage to the input facet[180] by spatially disjoining the SiO_2/Si_3N_4 from the Si trench deep-etching. It resulted in a significantly smoother surface, as confirmed by electron micrographs (Figure 7-1 b).

To further reduce transmission losses in the waveguide core, we covered its surface with a protective layer of SiO_2 (top cladding). The top cladding covers the input and expansion taper, leaving only a selected area exposed by etching, where the sample is placed and imaging is performed (imaging well, Figure 7-1 a). The final 2 µm silicon oxide top cladding was deposited by plasma enhanced chemical vapor deposition (PECVD).

To achieve an efficient coupling, we adopted a so-called inverted taper coupler (~150 nm wide tip) at the entrance to each waveguide that reduces the mismatch between the properties of the input and the waveguide electrical field (such as the mode size and the effective index; see Supplementary Information of the published work[181]). Specifically, by decreasing the waveguide core size, the evanescent field decay length increases, leading to a larger waveguide mode profile that better overlaps with the input beam source profile. A higher overlap between the shape of the input and the waveguide fields leads to a higher coupling efficiency. Moreover, in the case of HIC waveguides, a narrower tip width will produce a waveguide effective index closer to that of the input source, reducing back-reflections originating from mode mismatch. This is evident even in the simplified simulations I performed with custom Matlab functions based on a waveguide 2D slab approximation (see Appendix A).

We realized in collaboration with Aleksandra Radenovic group (specifically with Evgenii Glushkov) our nanotaper and waveguide using electron-beam lithography followed by dry reactive ion etching (RIE) – see Appendix C for the intermediate fabrication steps. To speed up this expensive lithographic step and to create as smooth as possible waveguide edges, I proposed to adopt a two-step exposure where only two frame-areas around the desired waveguide were exposed to the e-beam with different resolutions instead of to expose the area around the waveguide with a compromised resolution.

We next optimized the waveguide geometry to have a uniform evanescent field over a large area. We obtained a uniform excitation area for large FOV microscopy by adiabatically expanding the fundamental mode. Using a taper with a slow expansion rate of $\alpha = (w_T - w_S)/2L = 0.006$ (where L is the total taper length, equal to 1.5 cm in our design), similar to [59] (Figure 7-1 a), we were able to expand from a ~150 nm entrance-tip width (w_S) to a 100 µm final width (w_T). This expansion rate set the minimum chip length to about 2 cm, while the chip width can vary depending on the number of imaging waveguides and the distance between them. Since the footprint of the optimized waveguide chip is only 1 x 2 cm, we were able to reduce the cost per chip by producing multiple chips on a single wafer (up to 24 chips on a 100 mm wafer), each of which can be reused for different experiments (up to ~20 times).

The mode propagation after the expansion taper was investigated by simulations and by imaging the light scattered from the top surface of the waveguide. In the absence of a taper, strong fluctuations in intensity are evidence of multimode behavior, whereas with our adiabatic taper, scattering intensity from a rectangular waveguide of identical dimensions appears highly uniform (Figure 7-1 c and d). We also characterized the uniformity of the TIRF penetration depth by imaging fluorescently-coated beads of a known size[87,182,183]. Assuming a spherical geometry, the distance of points on a bead from the waveguide surface is known, so intensity profiles of individual beads encode the decay length of the evanescent field.

The detailed fabrication process flow is described in Appendix C. The fabrication steps were verified with widefield microscopy after every lithographic step and scanning electron microscopy after the waveguide etching.

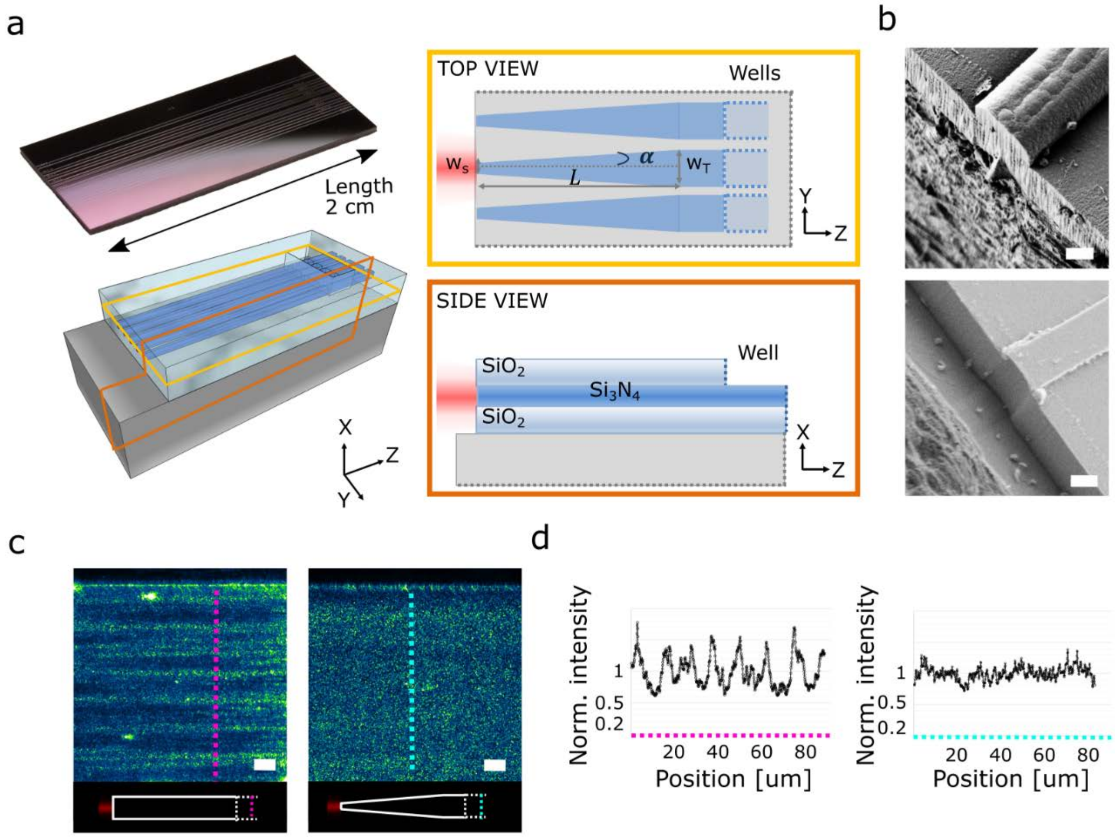

Figure 7-1 – Optimized waveguide design enables a uniform and large TIRF illumination. a, The chip design includes an inverted nanotaper with a 150 nm input width w_s, a 15 mm length L, and an expansion rate $\alpha = 0.006$ (yellow box). The waveguide input facet is offset from the substrate etching site (orange box). The waveguide structures appear as light-grey strips on top of the chip surface photograph - top left panel. **b,** Scan electron microscopy cross-section of the input facet shows that deep-etching the silicon (Si) substrate after the Si_3N_4/SiO_2 layer without the two-step-etching leads to a rough facet (c top). Si deep-etching after further lithographic steps – to offset the two etching sites - provides smooth Si_3N_4/SiO_2 facet and thus a more efficient coupling (c bottom). **c,** Scattered light from the top waveguide surface for a waveguide without a taper (left) is less uniform than that with a nanotaper with expansion angle alpha (right). **d** Line profiles (magenta, without taper; cyan, with taper) show modulation depth >20% and <12%, respectively. Panel taken from[181].

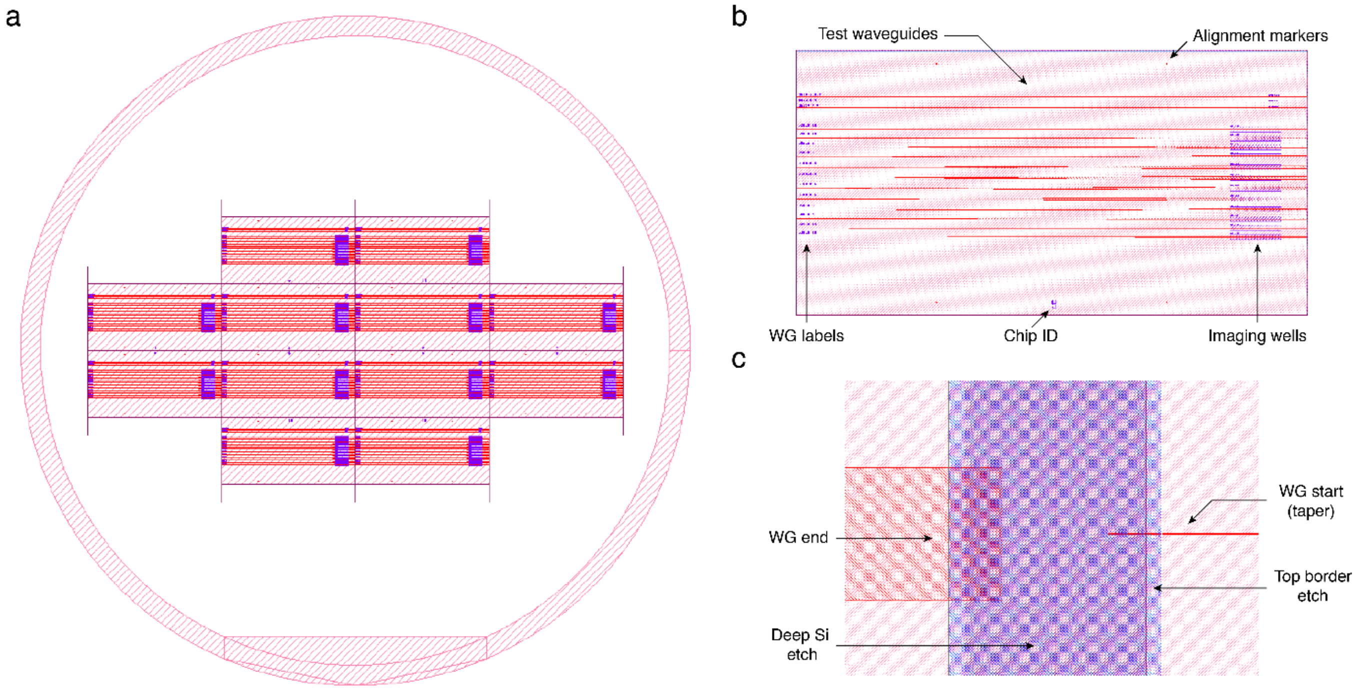
a
b
Test waveguides
Alignment markers
WG labels
Chip ID
Imaging wells
c
WG end
WG start
(taper)
Top border
etch
Deep Si
etch

Figure 7-2 – Layout of the waveguide chips for cleanroom fabrication. **a**, 12 chips, each containing 12 imaging waveguides, on the standard 4 inch (100 mm) wafer. **b**, Closer look at one of twelve chips showing additional design features such as the imaging wells (on the right side), the waveguide labels at the input nanotaper tips and the chip identification number (ID). **c**, Zoom-in on the border between two chips and the etching areas for the two-step lithography and etching process. Figure taken from[181].

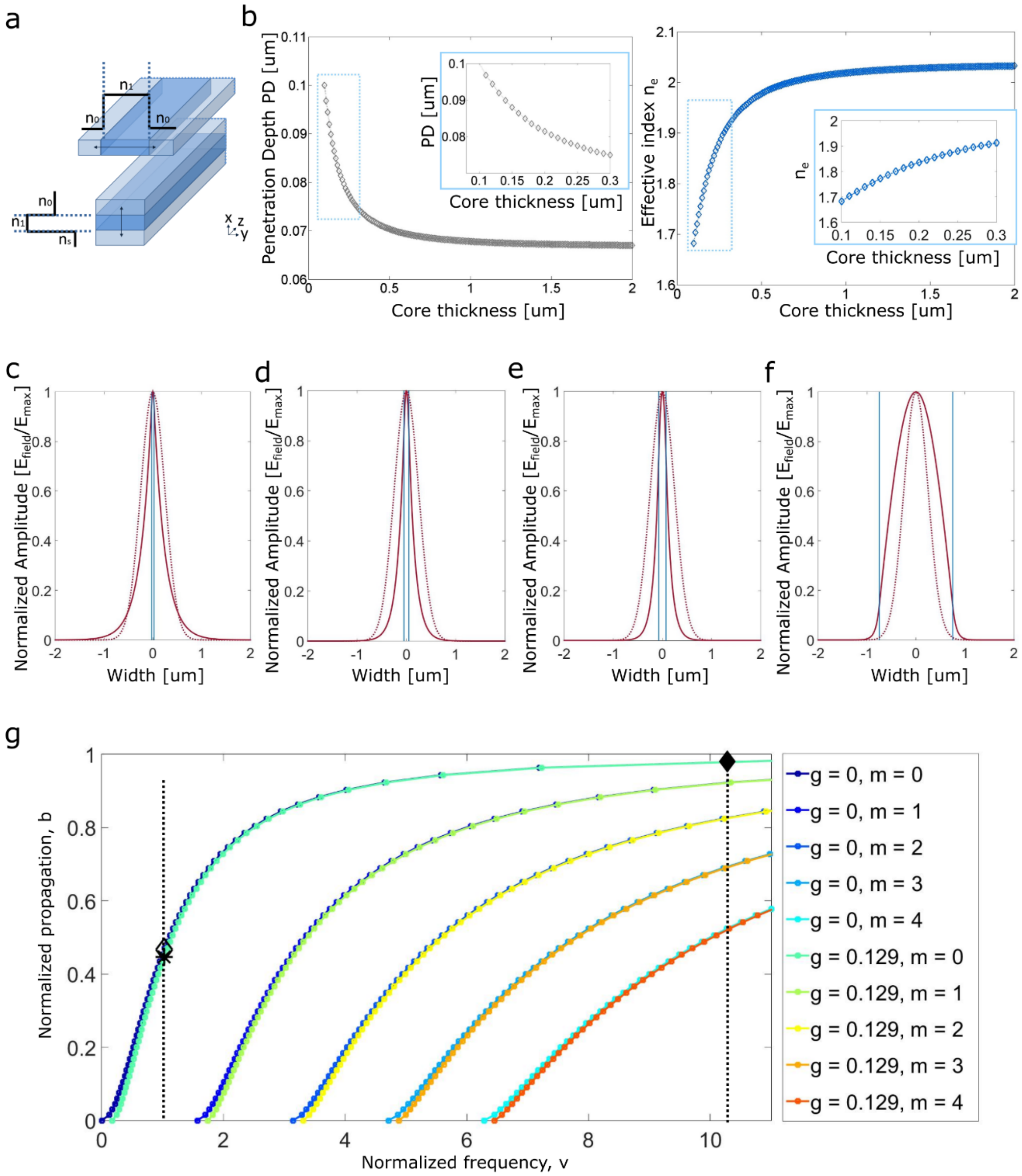

Figure 7-3 – Waveguide penetration depth and 1D TE0 waveguide mode simulations. a, The simulations were performed using a slab-waveguide approximation in *X* and *Y* directions (**a**). In the *X* direction the top cladding corresponds to the sample media with a refractive index of $n_0 = 1.38$. In the *Y* direction the lateral cladding is SiO_2 with a refractive index of $n_0 = 1.47$. All simulations were performed with a light wavelength of 647 nm and with a waveguide core with a refractive index of $n_1 = 2.04$. **b,** Penetration depth simulation as a function of the waveguide core thickness shows that the expected penetration depth is roughly 90nm for a 150 nm Si_3N_4 core waveguide excited with 647 nm light wavelength. Grey and blue diamond symbols represent the simulated penetration depth and effective index respectively. Simulations **c-f** show that decreasing (from **f** to **c**) the input taper width leads to a better overlap between fundamental mode excitation and beam field. Red dashed and continuous lines correspond to the simulated beam input and mode profile respectively. Blue vertical lines correspond to the waveguide core-cladding interface positions. **c,** Taper input width 50nm. **d,** Taper input width 100 nm. **e,** Taper input width 200 nm. **f,** Taper input width 1.5 µm. **g,** The simulated dispersion curves for both the two direction *X* (with a asymmetry coefficient gamma = 0.1287) and *Y* (gamma = 0), show that for the both directions (black start indicates the result for the *X* direction where the core width is 150 nm, $v = 1.028$, $b = 0.447$, $ne = 1.74$; black-no fill-diamond indicate the result for the *Y* direction where the input taper width is 150nm, $v = 1.028$, $b = 0.466$ and $ne = 1,76$) the single mode excitation is ensured. While for *Y* direction where the input taper width is 1500nm (black fill diamond), $v = 1.028$, $b = 0.466$ and $ne = 1,76$) the single mode excitation is not ensured. The input beam size is estimated based on [112].

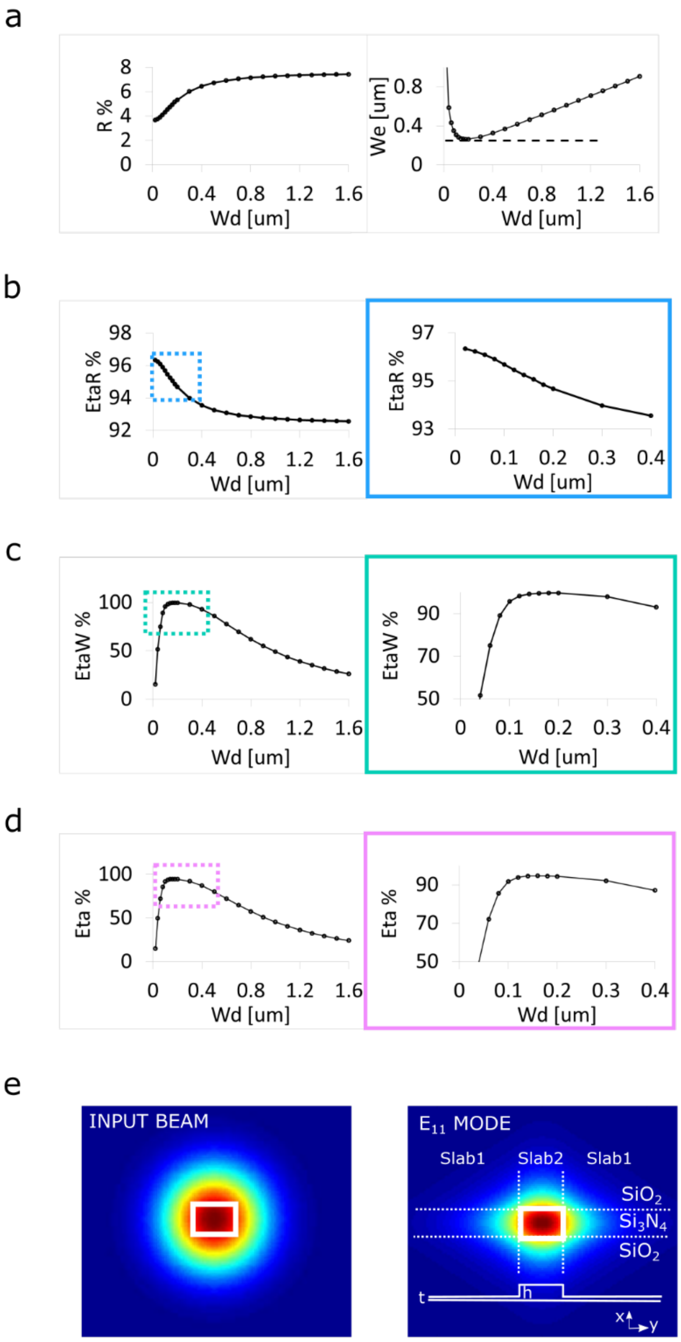

Figure 7-4 – Approximated coupling efficiency estimation and E11 waveguide mode profile at the input taper tip. A 150 nm thick Si_3N_4 waveguide core (refractive index of n_1 = 2.038 at 647 nm) is surrounded by SiO_2 (refractive index n_0 = 1.47 at 647 nm). **a,** The two main contributions to coupling losses are due to Fresnel reflection (Left) and the waveguide field mode and input beam field distribution mismatch (Right). **b,** Transmission efficiency η_R. **c,** Field distribution efficiency, η_W. **d**, The final coupling efficiency η is the product of the transmission (η_R) and mode overlap efficiency (η_W). The effective index of the waveguide (fundamental to compute the main waveguide properties such as the effective mode width and the reflection) has been computed using the effective index approximation method (**e**). Figure taken from[181].

7.2 Chip holder and Microscope design

To become an efficient tool, a wide field waveguide-based TIRF DNA-PAINT microscope needs an effective way to quickly and firmly position the waveguide chip and align it to the laser line, a support to hold and exchange the liquid on top of the waveguide chip, and a shield limiting the input scatter light. In the previously proposed waveguide platform[60] the chip was secured with a vacuum holder (Waveguide Mount HWV001 Thorlabs) which is more prone to vibration and devoid of the aforementioned features.

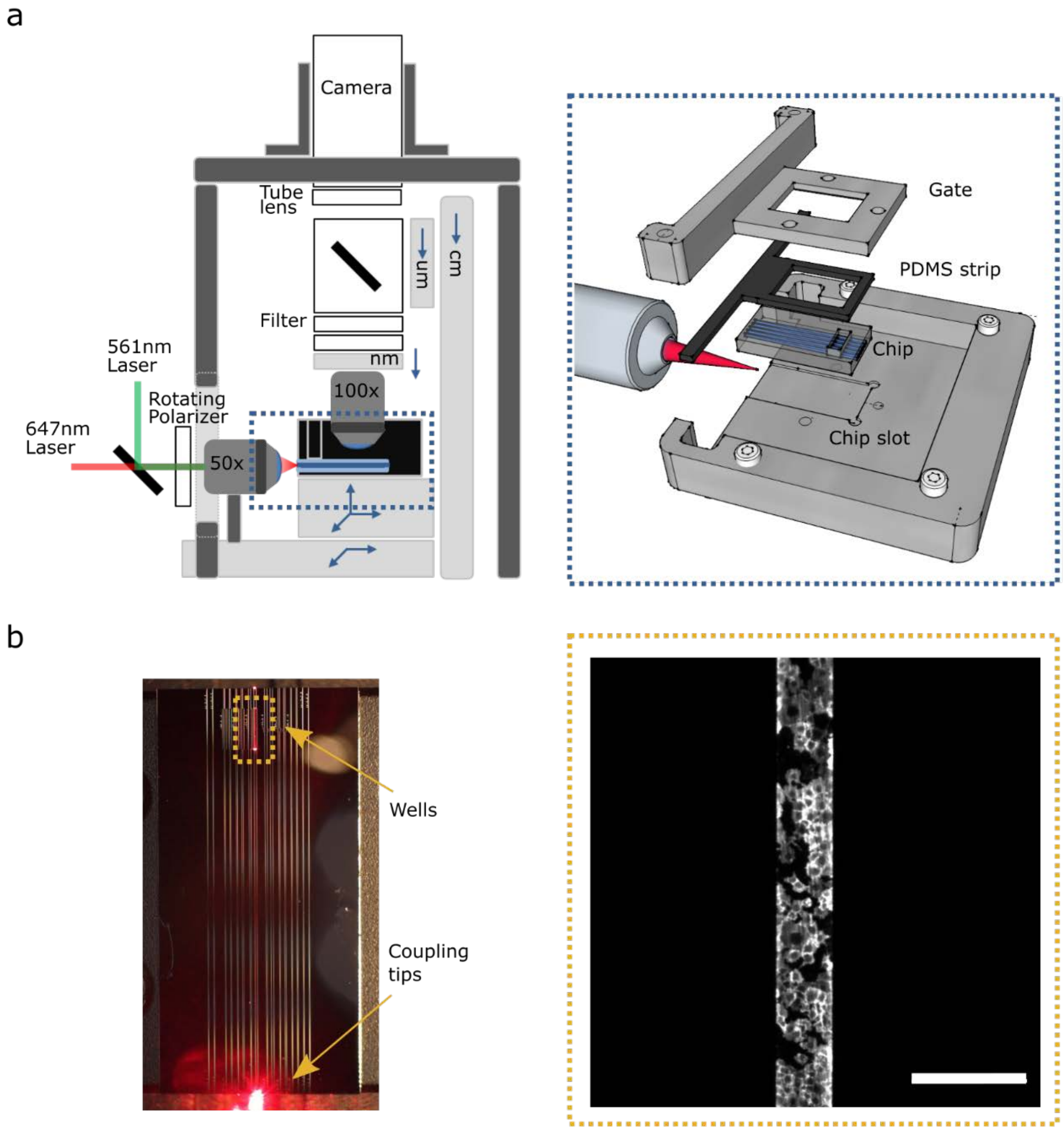

Figure 7-5 – Waveguide-PAINT platform: waveguide-chip integration in a custom upright microscope. a, The proposed DNA-PAINT microscope is designed with two independent arbors: one axle (dark-gray) holds the most heavy components that does not need Z adjustments while a three-gauges system (light gray) provides large (centimeter range), micrometric and nanometric positioning. The waveguide holder (dashed blue line) enables a free space coupling through a *X-Y-Z* nanometric stage placed on top of the *X-Y* stage for FOV adjustments. The holder design presents a precision slot to position and orient the waveguide chip properly with respect to the laser line, and a sealing gate to hold the imaging buffer and to shield scattered light. **b,** Efficient coupling is established when the light scattered from the well is maximized. The magnified view (low magnification 4x) TIRF imaging show about 50 COS7 cells labelled with cholera toxin B conjugated to Alexa 647. Scale bars: 500 µm.

To fulfill all these requirements I designed a proprietary chip holder, shown in Figure 7-5 a. The holder sports a removable gate to easily install and lock the chip in a dedicated slot aligned with the input beam. The gate is designed to shield the scatter light without interfering with the imaging objective, even while working at the shortest focal distances. The imaging buffer (aqueous solution) sealing is ensured by a PDMS strip at the gate-chip interface. To reduce transmission of light scattered at the entrance window, I realized a black PDMS strip by mixing the based and curing agent with toner from a printer cartridge with the help of Wojciech Chomicki in Giovanni Dietler's laboratory. Finally, I designed the shape of the reservoir to minimize its volume, while ensuring that the imaging dipping objective could still fully access the sample area.

Although our waveguides could be imaged on an existing upright microscope, with the simple addition of a coupling objective to introduce excitation light, we designed and built a simple and cost-effective upright microscope with off-the-shelf optomechanical components. The sample holder is supported by a three-axis piezo stage, used for fine adjustment in aligning the entrance window with the coupling objective. In turn, both this stage and the coupling objective are mounted on an *X-Y* platform for imaging different regions of the sample. A mechanically rigid vertical structure suspends the camera and tube lens, while a separate axle with a three-gauge *Z*-adjustment system provides coarse (centimeter range), and fine (micrometric and nanometric) positioning (Figure 7-5 a). To better transmit our findings, we shared the designs for this microscope as well as a precise workflow pipeline in our published work[181], which includes details on key steps such as waveguide excitation coupling and imaging. We found that an effective coupling could be easily established by maximizing the light scattered from the top surface of the waveguide (Figure 7-5 b).

The chip holder designed greatly benefited from the supportive and active discussion with Pinard Alain (head of Mechanical Engineering Workshop).

7.3 Waveguide DNA-PAINT imaging of cells and DNA origami

To validate our platform, we adopted two strategies. First, we imaged a structure inside the cell with shape and dimensions well characterized: the microtubules with their hollow cylindrical shape. The microtubule circumference, labeled with primary and secondary antibodies, is projected by the SMLM system on a discrete plane with pixel size roughly a quarter of the overall microtubules diameter (about 40 nm). The result is a clear double Gaussian distribution where the distance of the peaks corresponds to the microtubules edges. Microtubules labeled with primary and secondary antibodies have roughly an effective dimeter of about 40 nm. Thus, the resolution of our system will be demonstrated by resolving microtubule profiles with double peaks spaced by 40 nm. Second, we imaged nano-shape created with DNA strands: DNA-origami grids made by 3 by 4 target-sites equally separated by 20 nm. All the imaging and platform validation has been done under the guidance of Dr. C. Sieben.

7.3.1 *Sample preparation*

Our waveguides were wide enough to accommodate multiple cells within one imaging well area (100 µm x 2000 µm). Four whole cells could fit within a single field-of-view. We imaged cells with waveguide-PAINT that were pre-extracted then antibody-stained against tubulin, and observed a continuous network of microtubules within each cell, only depleted below the cell nucleus (Figure 7-7, Figure 7-9a and Figure 7-10). We measured microtubule diameter consistent with the expected value ~40 nm (Figure 7-9b).

COS-7 cells were maintained in DMEM (Life Technologies) supplemented with 10% fetal calf serum (HyClone) and passaged every 3 days. The waveguide chips were cleaned with Hellmanex III (Sigma, 2% in water) at 50 °C for 10’, rinsed in water and UV sterilized for 15 min before seeding the cell. The chip were then incubated with 1% poly-L-lysine (vol/vol) (Sigma) in water for 15 min. After 24 h, the cells were washed in pre-warmed PBS, pre-extracted with 0.5% (vol/vol) Triton X100 (Sigma) in BRB80 buffer (80 mM Pipes, 1 mM MgCl2, 1 mM EGTA) for 15 sec, then fixed with ice-cold methanol for 10 min. The cells were washed in PBS and blocked for 30 min using 5% bovine serum albumin in PBS. Microtubules were labelled for 2 h at room temperature with primary antibodies against α-tubulin (B512, monoclonal produced on mouse, Sigma T6074) diluted 1:100 in PBS supplemented with 0.2% (vol/vol) Triton X100 (PBST). Unbound antibodies were removed in three washing steps with PBST for 10 min each. The samples were incubated with secondary antibodies in PBST for 1 h followed by three washes in PBST. Cells were prepared to perform both DNA-PAINT and wide field microscopy. The second channel served as reference channel to select the desired FOV and to identify the proper focus. Thus, we used a combination of DNA-labelled (goat-anti mouse I1, Ultivue Duplex Kit (discontinued), 1:100) and Alexa555-labelled (goat-anti mouse, Life Technologies (A21422), 1:5000) secondary antibodies. Finally, the cells were fixed again in Methanol and stored at 4 °C until further use. For cell membrane imaging, cells were chemically fixed with 4% paraformaldehyde (Alfa Aesar) in PBS for 10 min and then labelled with A647- conjugated cholera toxin B (Life Technologies). Cell growth and seeding was performed by Dr. H. Perreten. Immunostaining was performed by Dr. C. Sieben.

As previously mentioned, we next used DNA-origami grids to further validate the performance of waveguide-PAINT. In principle, if their deposition was controlled, a single field of view could fit up to hundreds of thousands of individual structures. In practice, origami were randomly deposited and sometimes sticking together, limiting the suitable imaging areas. Moreover, most structures were incomplete, which is consistent with reported folding efficiencies[184]. However, by aligning and overlaying PAINT reconstructions of multiple origami, we recovered both the expected 4 × 3 structure (Figure 7-9d) as well as the grid spacing (Figure 7-9e).

Custom microtubule-like DNA-Origami (Figure 7-6) were purchased from Gattaquant, the 20 nm DNA origami grid was kindly provided by Ralf Jungmann. DNA origami imaging samples were prepared using buffers A (10mM Tris-HCl and 100mM NaCl at pH 8.0), A+ (10 mM Tris-HCl, 100mM NaCl and 0.05% (vol/vol) Tween 20 at pH 8.0) and B+ (5mM Tris-HCl, 10mM MgCl2, 1mM EDTA and 0.05% (vol/vol) Tween 20 at pH 8.0).Briefly, cleaned waveguides were incubated with BSA-biotin (1mg/ml in buffer A) for 2min, then rinsed in buffer A+ and incubated with streptavidin solution (0.5 mg/ml in buffer A). The waveguides were washed sequentially in buffer A+ and B+ before incubation with DNA origamis diluted in buffer B+ for 2 min. Samples were washed again in buffer B+ and stored at 4 °C until further use.

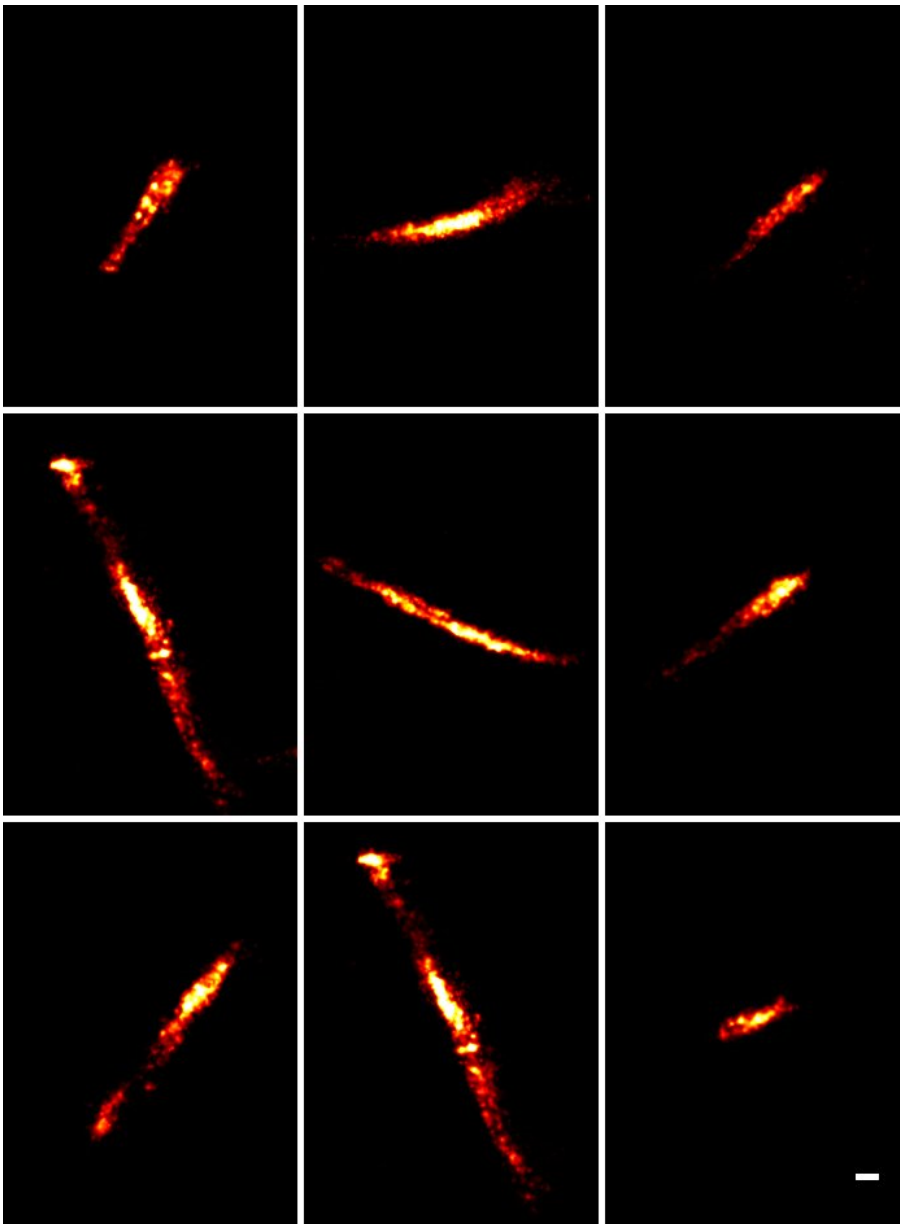

Figure 7-6 – Waveguide-PAINT imaging of DNA-origami microtubules. Every panel is the image reconstruction of 15000 raw images of microtubules imaged with 500pM of imager strand. This experiment was a preliminary experiment to test the resolution of the platform. However, the origami structures appeared to be fragmented and damaged: the structure that should be a 2D rectangular layer folded in rectangular parallelepiped appear an open 2D surface that tend to twist. The double peak measured along the tube length is about 40 nm. Scale bar 100 nm.

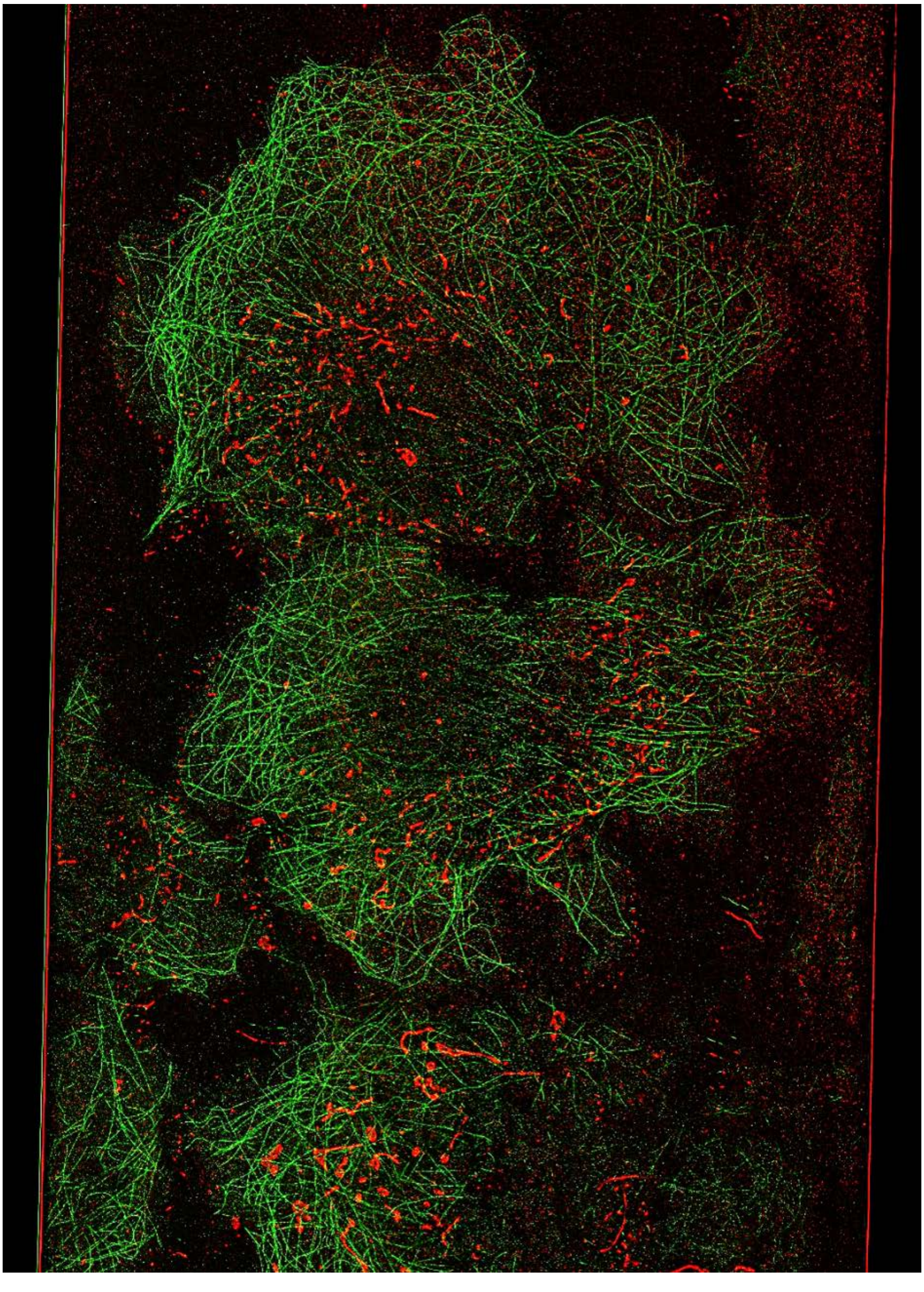

Figure 7-7 – Waveguide-PAINT imaging of COS-7 cells. Image reconstruction of 8000 raw images of microtubules and mitochondria labeled with antibodies against α-tubulin and Tom-20.
Imaging performed using a 200 pM concentration of imager strands 650-I1 and 650-I2 (imager and docking strands provided by R. Jungmann group).

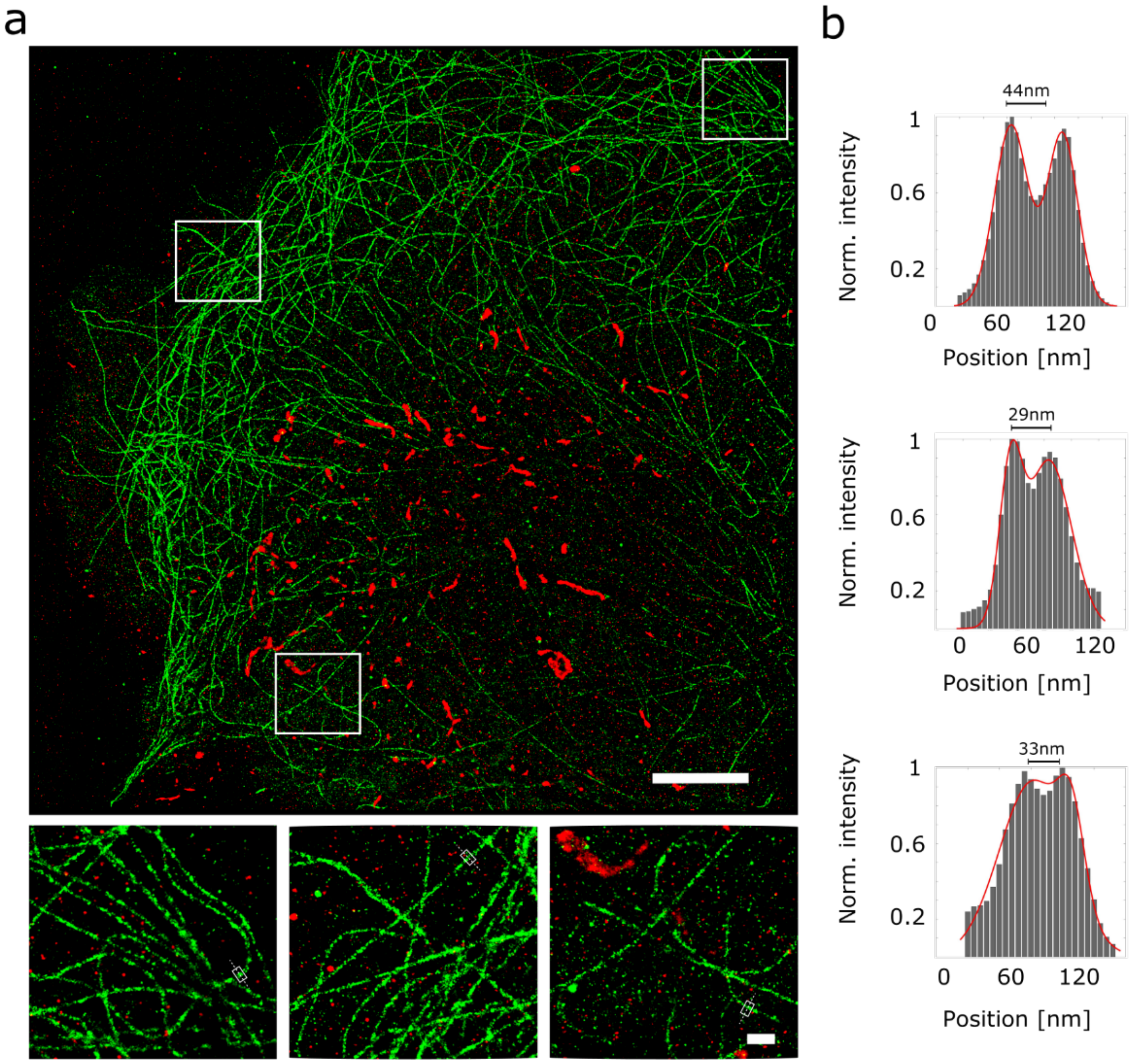
a
b
44nm
29nm
33nm
Norm. intensity
1
0.6
0.2
0
60
120
Position [nm]

Figure 7-8 – Waveguide-PAINT imaging of COS-7 cells. Image reconstruction of 12000 raw images of microtubules and mitochondria labeled with antibodies against α-tubulin and Tom-20. The FOV is a cropped FOV from the previous figure thus the sample preparation and imaging condition are exactly is the same.)

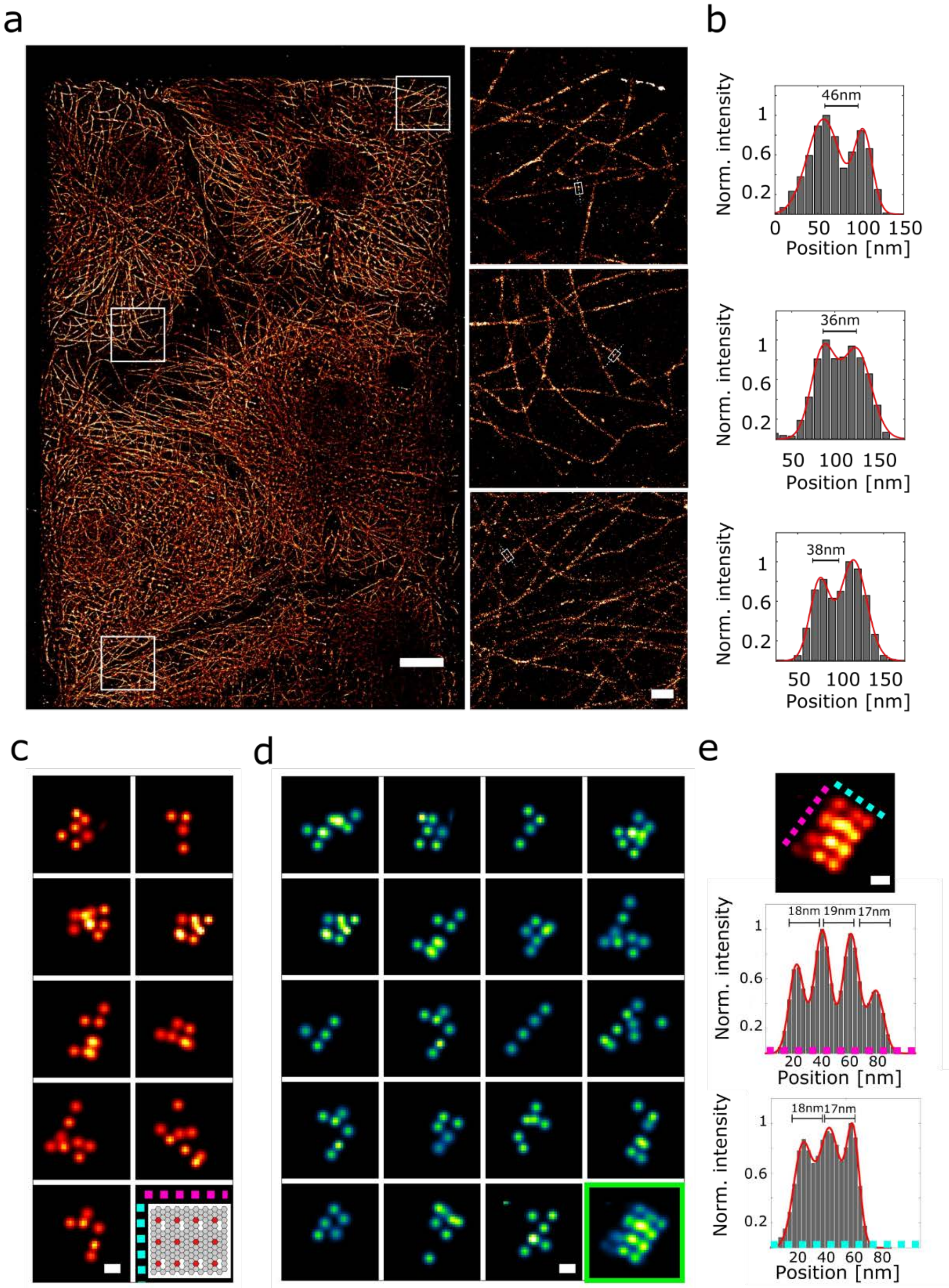

Figure 7-9 – Demonstration of waveguide-PAINT. a, Single field of view DNA-PAINT reconstruction of COS7 cells cultured on a waveguide, labeled with antibodies against α-tubulin and imaged using a 500 pM concentration of imager strand (I1-655, Ultivue Duplex Kit) (left panel). Magnified views of the boxed regions (left panel, from top to bottom) show microtubules well-resolved across the field of view (a, right panel). **b,** Intensity profiles across individual microtubules (as defined in **a**, right panel) reveal two peaks that can be described with the sum of two Gaussian functions (b, red line). **c,** Magnified views from a single field of view DNA-PAINT reconstructions of a 20-nm-grid DNA origami imaged with Cy5-conjugated imager strands (500 pM). **d,** Average image of about 20 DNA origamis reveal the 4x3 grid arrangement as well as the respective grid spacing. **e,** Intensity profiles along colored axes in (**d**). Scale bars: 10 µm (a), 0.5 µm (a, right panel) and 20 nm (c and d).

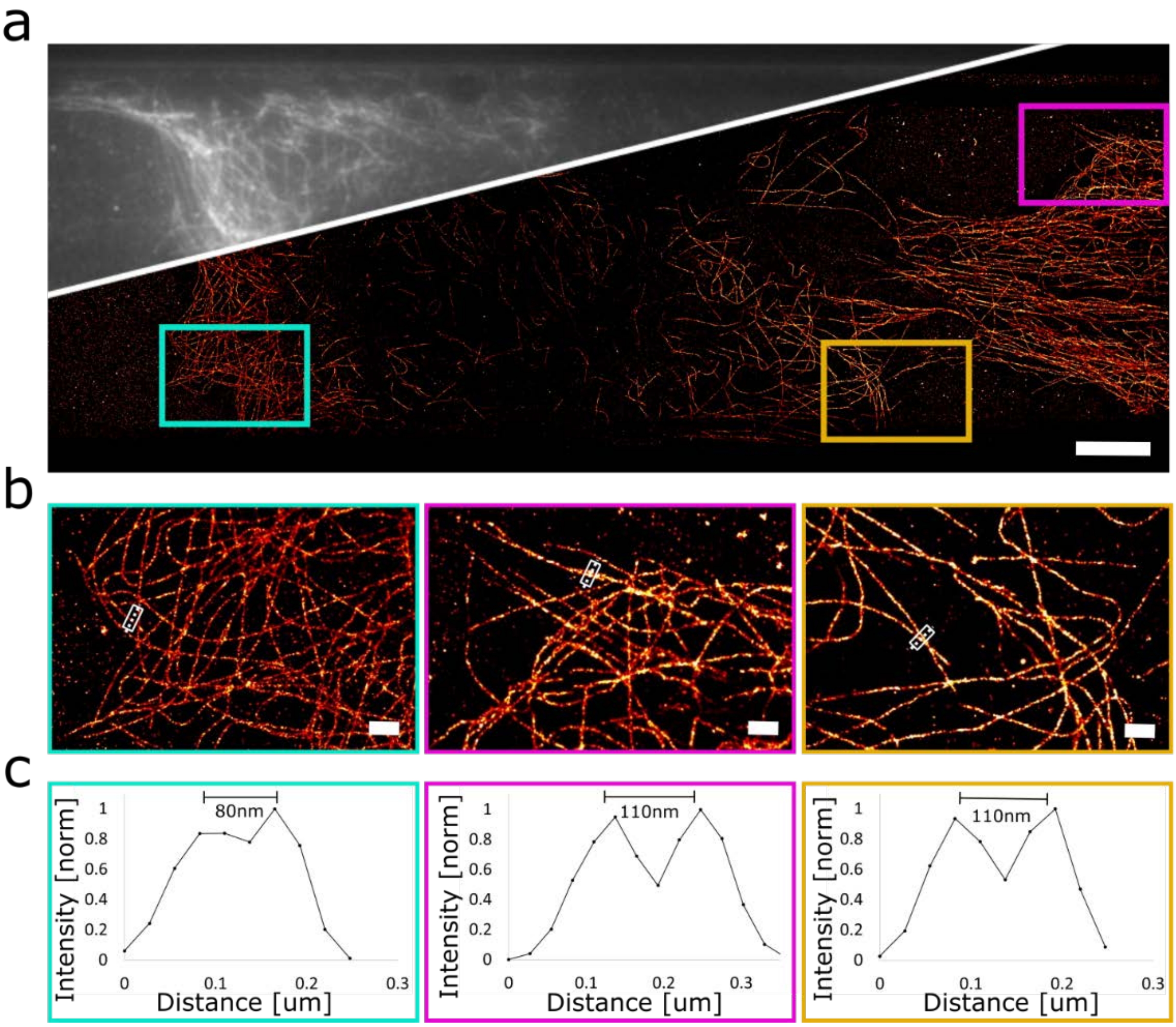
a
b
c
80nm
110nm
110nm
Intensity [norm]
1
0.8
0.6
0.4
0.2
0
0
0.1
0.2
0.3
Distance [um]

Figure 7-10 – Diffraction limited and DNA-PAINT. a, Single field of view DNA-PAINT reconstruction of COS7 cells labeled with antibodies against α-tubulin and imaged using 500 pM imager strand (I1-560, Ultivue Duplex Kit). Green channel. **b,** Magnified views of the boxed regions show microtubules well-resolved across the field of view. **c**, Intensity profiles across two microtubules reveal two peaks corresponding to the two crossing microtubule. Scale bar 20 µm (**a**), 1 µm (**b**).

7.3.2 *Imaging and data analysis*

We performed the DNA-PAINT experiments using different imager strands: I1-655 (Ultivue Duplex Kit), P3-Atto655: GTAATGAAGA- Atto65528 and Atto655-imager strand (Gattaquant). PAINT imager strands were diluted in buffer B+ to a final concentration between 0.1–0.5 nM. The waveguide chip prepared with the sample was placed into the custom holder and ensured under the microscope. Finally, the diluted imager (~2 ml) was added. The holder position was adjusted until the laser coupling was satisfying. The microscope and all components were controlled with µManager[185]. The 642 nm laser output power was set to 5 mW and the sample was moved into focus using the coarse and fine focusing screws. A single waveguide well was centered on the camera and the exposure time was adjusted to maximize signal to noise without creating overlapping localizations (typically around 150 ms). For microtubules (Figure 7-9a), we acquired 25000 frames at 150 ms continuous exposure and 100mW laser output power. DNA origami-grid structures in Figure 7-9d were imaged for 10000 frames at 300 ms.
Finally, the first DNA origami imaging test were performed on DNA origami microtubules acquiring 15000 frames at 150 ms.
Single-molecules were localized using ThunderStorm[186] or a recent GPU-based fitting algorithm[126]. Localizations were drift corrected using redundant cross correlation[187], filtered and visualized using a Gaussian-blurred (1xsigma) 2D histogram.

Sample/ Figure	**Exposure time [ms]**	**Imager concentration [nM]**	**Laser λ [nm]**	**Laser power [mW]**	**Number of Frames**	**Loc. precision [nm]**	**Photons per loc.**	**Analysis Algorithm**
Figure 7-9 b	150	0.5	647	100	25000	6 ± 2	6250±3770	Spline, with experimental PSF[126], and TunderStorm
Figure 7-9 c	300	0.5	647	100	10000	4 ± 1	9420± 5600	LS, multi-emitter, ThunderStorm[186]
Figure 7-10	100	0.5	565	55	10000	13 ± 5	2050 ± 1500	LS, multi-emitter, ThunderStorm[186]
Figure 7-8 (microtubules channel)	150	0.2	641	100	12000	7.5 ± 3	3750 ± 3060	LS, multi-emitter, ThunderStorm[186]

Table 7-1 Waveguide-PAINT experimental conditions and results. The table presents a summary of the laser and camera acquisition parameters and the localization results such as the localization precision and the average number of photon per molecule.

PART VI

DISCUSSION AND CONCLUSIONS

Large flat field waveguide-PAINT

8 Conclusions and final remarks

8.1 Cell shape image analysis automation

Cell morphology is a large-scale expression of processes concerting within the cell and emerging in the cell-to-cell phenotypic variability critical for cellular function, behavior and survival in a specific environment. It is thus no surprise that morphology is used as qualitative or quantitative measure of the outcome of various assays and to quantify global cell states. Developments towards high-throughput cell shape analysis make it an even more powerful tool for cell biology.

Thus, computational tools are fundamentally necessary to extract the main cell shape parameters from large datasets, to achieve an unbiased quantification and statistical validation of the relationship between cell shape parameters and experimental conditions.

When we were finalizing our cell shape analysis study and thus our sDaDA software pipeline, an open source software (Oufti) for quantitative cell shape analysis was published[188]. This tool presents multi-threading capabilities to process large cell image datasets, to perform cell tracking and sub-pixel edge detection. Oufti provides a solution accessible to scientists with no formal computational experience and all its modules have been integrated in a single package with a user-friendly GUI. Moreover, it does not requires any MATLAB license. Nevertheless, our sDaDa tool still provides an effective solution to extract information on the C.*Crescentus* cell septum diameter up to the last stages of division thanks to its accurate septum edge detection described in Chapter 5.1.

Molecular machineries regulating the cell-cycle progression have a direct impact on the cell shape regulation and homeostasis. Thus, to understand the link between these molecular players and the cell shape eventually achieved requires the measurements and study of the dynamics of cell shape parameters throughout the cell cycle. Cell shape dynamics studies are usually done through time-lapse microscopy to track individual cells over the full cell cycle. However, this approach suffers by limited temporal accuracy and requires perturbations.

Infer cell-cycle state from large fixed cell population represents a powerful alternative to access cell shape parameters without any intrinsic temporal resolution limit[189] and also without the need of a homogenous growth conditions[190].

I think that before moving into powerful algorithms to extract continuous temporal and spatial trajectories of cell shape parameters starting from unsynchronized cell population, it is fundamental to further investigate single cell shape dynamics. Specifically, the sources of cell- to-cell variability at different stages over the cell cycle, their mechanistic link and impact on the following cell cycle steps, have to be identified for every cell type and condition to enable their proper deconvolution during the cell-cycle trajectory extraction from a fixed population analysis.

For *C.Crescentus*, our first study could provide the basis towards the identification of the possible sources of cell-to-cell variability across the cell cycle. We observed that cells that elongate less during the constriction do elongate more before constriction and we hypothesized that this compensation could be regulated by the constriction rate and its PG precursor excess (the higher the excess, the shorter the constriction duration). Is there a possible robust link between PG precursor, septum width and cell length during constriction to account for cell to cell variability in cell length during constriction?

8.2 Flat-field illumination platform: prospective

Beyond imaging a larger FOV, a flat and uniform sample illumination improves image quality by substantially reducing the position-dependent photophysics, thereby greatly advancing quantitative fluorescence imaging. We previously described different optical solutions capable of leveraging the sensor size of commercially available CMOS cameras. However, to fully exploit their advantages in the context of SMLM, the CMOS camera must be characterized and its main pixel dependent parameters included in the localization algorithm. Although, CMOS-specific MLE has been proposed, most SMLM users still adopt CMOS cameras without correcting for their pixel dependent characteristic. This is probably due to the lack of straightforward, easy-to-use and open-source tools for camera characterization. Current efforts in the field aim to develop a user-friendly Fiji plugin that performs a characterization of the camera simply based on stacks of dark frames at different exposures times to characterize the camera.

Today, routinely performance of quantitative imaging sets the urgent need of robust pipelines to save, process and share big dataset. To address this need our laboratory could not find specific guideline. I personally took care of designing a workstations networks with Kessous Michel (former EPFL technician) to efficiently perform image acquisition, analysis and sharing among different members and in parallel. In the future, it will be useful to have an interactive interface that allows one to try different building block and quickly visualize the speed and spatial limitations of the network.

In my opinion, the current developments in large-flat field SMLM, require an even stronger focus on interdisciplinary context to address relevant biological questions that can on the same time leverage the technique.

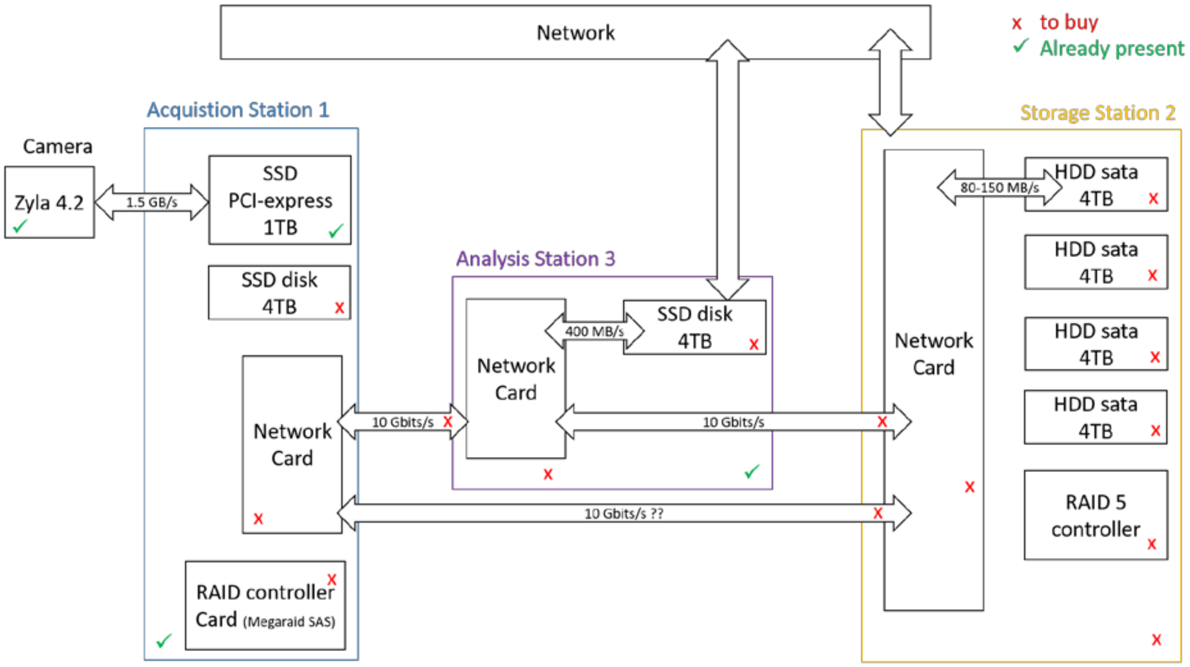
Network
x to buy
✓ Already present
Acquistion Station 1
Storage Station 2
Camera
Zyla 4.2 ✓
1.5 GB/s
SSD PCI-express 1TB ✓
SSD disk 4TB x
Analysis Station 3
Network Card
400 MB/s
SSD disk 4TB x
10 Gbits/s x
10 Gbits/s x
x ✓
Network Card x
10 Gbits/s ?? x
RAID controller x Card (Megaraid SAS)
✓
Network Card x
80-150 MB/s
HDD sata 4TB x
HDD sata 4TB x
HDD sata 4TB x
HDD sata 4TB x
RAID 5 controller x
x

Figure 8-1 – Workstation network for big-data acquisition and analysis. Example of one possible workstation configuration we could adopt in our laboratory.

8.3 Waveguide-TIRF: prospective

Many efforts have focused on tuning the penetration depth to extract axial information with high resolution. Specifically 3D-multi-angle-TIRF (based on dependence of the penetration depth on the illumination angle) has been demonstrated on microtubules[88,191], secretory granules[192] and cell membrane as well as multi-angle-TIRF combined with photobleaching[193] with axial resolution up to 10 nm. Thus, such 3D-objective-TIRF approach combines very high axial resolution with simple setup modification and optical sectioning. In the future, it will be natural to exploit the potentiality of such 3D-TIRF in a waveguide-TIRF platform.

A further development of our waveguide-TIRF platform could involve advantages from other modalities[194] by performing correlative microscopy. One advantage of our waveguide design for correlative imaging is the presence of specific markers that provide a natural reference frame for aligning different measurements – e.g for correlative light and scanning electron microscopy[195]. Moreover, the low surface roughness of the etched wells makes them suitable for atomic force microscopy and correlative PAINT-AFM measurements.

Finally, a multi-well waveguide chip as shown in Figure 8-2, could be used combined with a micro-manipulator as a screening platform for the parallel high-throughput imaging of different conditions. More specifically, a DNA-origami nanostructure[43] could be placed in a validation-calibration well independent from the sample well to perform quantitative DNA-PAINT (qPAINT) in a single step.

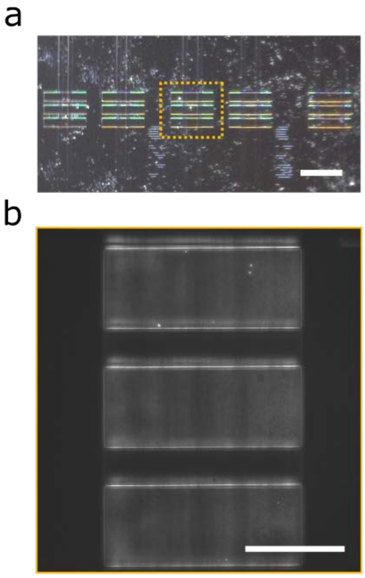

Figure 8-2 – Multi-well waveguide chip fabrication. The presence of 3 wells within the same field of view provide a high-throughput platform for screening of different sample conditions. **a,** Low magnification imaging of multiple waveguides with multiple wells. **b,** Multiple wells imaged with the waveguide chip and chip holder setup. Scale bar 2 mm (**a**) and 50 µm (**b**).

APPENDIX

A. Waveguide parameters study

I performed some basic waveguide parameters analysis to extract first guess on:

- waveguide effective index range
- penetration depth as a function of the waveguide core thickness
- effective mode width range
- normalized propagation constant (b) and normalized frequency (v) numbers

All this analysis is described in the Supplementary Note 1 of the Supplementary Information of the published work[181]. The corresponding MATLAB code to perform 2D simulations is available on the GitHub repository https://github.com/LEB-EPFL/WGmode.

B. Chip holder cad design

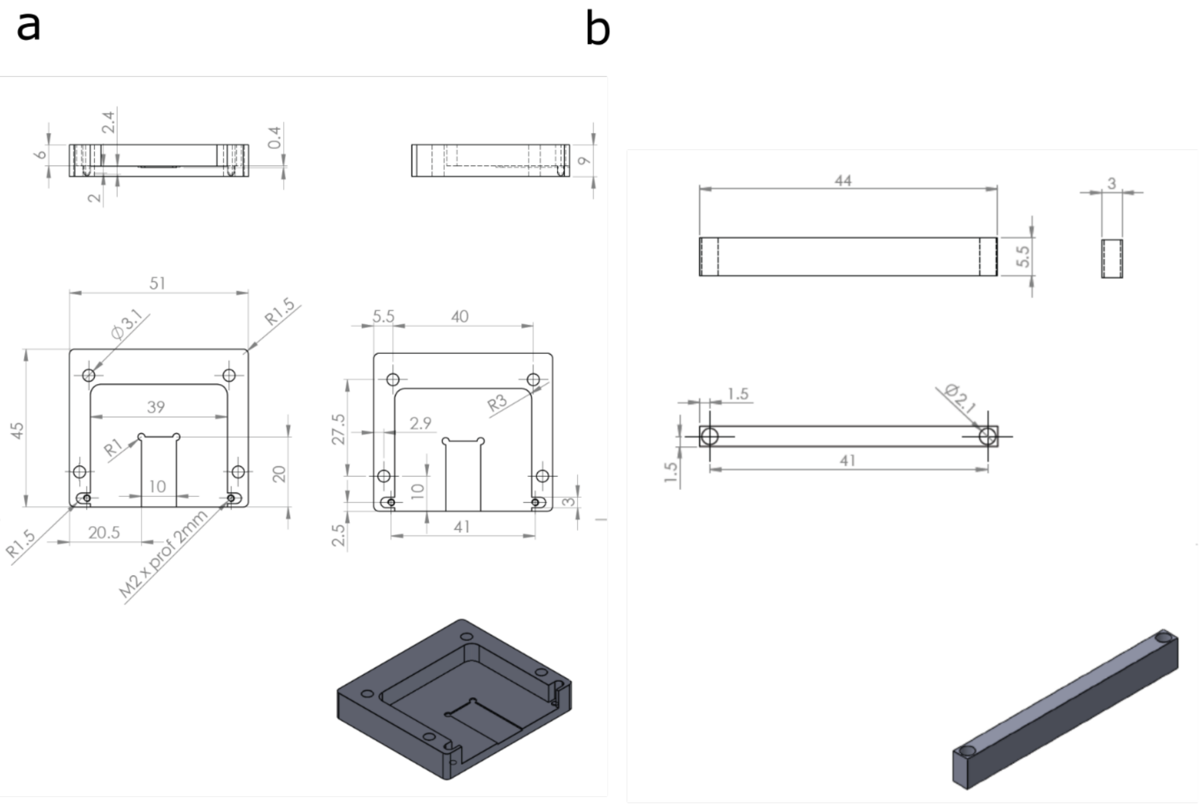
a
b
2.4
6
0.4
2
6
51
Ø3.1
R1.5
39
45
R1
20
10
R1.5
20.5
M2 x prof 2mm
5.5
40
R3
27.5
2.9
10
3
2.5
41
44
3
5.5
1.5
Ø2.1
41
1.5

Figure C-1 – Chip Holder – mechanical design. The technical drawing conveys the main dimensions and tolerances necessary to reproduced the waveguide chip holder. **a,** The chip holder base can be directly screw in a standar matric breadboard with M2 screws. **b,** The holder gate ensure prevent scatter waveguide coupling light to create background inside the chamber.

C. Chip fabrication

Step	Process description	
01	Si3N4 150 nm high-stress LPCVD deposition (Waveguide core layer)	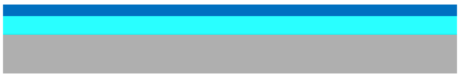
02	E-beam lithography (Waveguides & alignment markers) (ZEP, 300 nm; dose: 180 uC/cm^2 @ 100 kV)	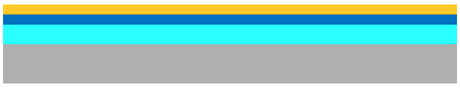
03	Si_3N_4 RIE (waveguide realization) (SPTS APS, CHF_3/SF_6 chemistry; etch time: 60 s)	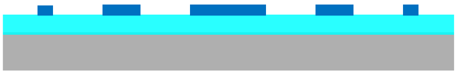
04	SiO_2 2 µm LPCVD deposition (top cladding layer) (Centrotherm furnace, Low Temperature Oxide, SiH4 @ 450°C)	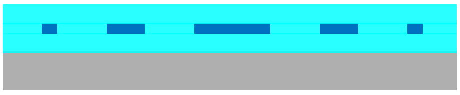
05	Photolithography (Imaging well & top borders) (Heidelberg MLA150; AZ ECI, 1.5 µm; dose: 170 mJ/cm^2 @ 405 nm)	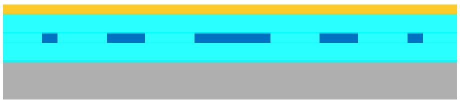
06	SiO_2 RIE (Imaging well and top cladding border etching) (SPTS APS, He/C_4F_8 chemistry; etch time: 4 min 51 s)	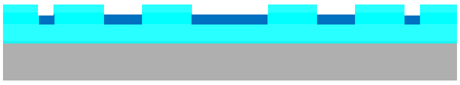
07	Photolithography (Borders & top facets) (Heidelberg MLA150; AZ ECI, 1.5 µm; dose: 170 mJ/cm^2 @ 405 nm)	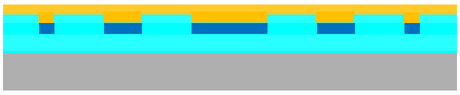
08	SiO_2/ Si_3N_4 RIE (Core and bottom cladding etching) (SPTS APS, He/C_4F_8 chemistry; etch time: 10 min)	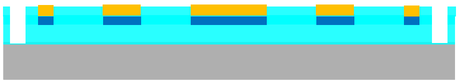
09	Photolithography (Chip borders for deep etching) (Heidelberg MLA150; AZ 9260, 5.5 µm; dose: 255 mJ/cm^2 @ 405 nm)	
10	Si deep-etching (Deep etching of chip borders) (Adixen AMS200, Bosch process, etch time: 75 min; etch depth: 300 µm)	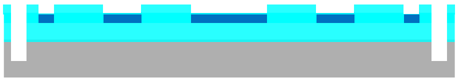
11	Si backside grinding (Splitting the chips) (DAG810 automatic surface grinder)	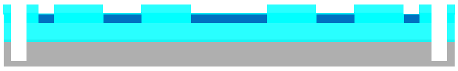

Table D-1 Waveguide fabrication process flow. The table presents a summary of the main litographic and etching steps

.

Bibliography

1. Bates, M., Huang, B. & Zhuang, X. Super-resolution microscopy by nanoscale localization of photo-switchable fluorescent probes. *Curr. Opin. Chem. Biol.* **12,** 505–14 (2008).
2. Rust, M. J., Bates, M. & Zhuang, X. Sub-diffraction-limit imaging by stochastic optical reconstruction microscopy (STORM). *Nat. Methods* **3,** 793–5 (2006).
3. Jungmann, R. *et al.* Multiplexed 3D cellular super-resolution imaging with DNA-PAINT and Exchange-PAINT. *Nat. Methods* **11,** 313–318 (2014).
4. Gustafsson MG. Surpassing the lateral resolution limit by a factor of two using structured illumination microscopy. *J. Microsc.* **198,** 82–7 (2000).
5. Hess, S. T., Girirajan, T. P. K. & Mason, M. D. Ultra-high resolution imaging by fluorescence photoactivation localization microscopy. *Biophys. J.* **91,** 4258–4272 (2006).
6. Betzig, E. *et al.* Imaging intracellular fluorescent proteins at nanometer resolution. *Science* **313,** 1642–5 (2006).
7. Bates, M., Huang, B., Dempsey, G. T. & Zhuang, X. Multicolor super-resolution imaging with photo-switchable fluorescent probes. *Science* **317,** 1749–53 (2007).
8. Schermelleh, L., Heintzmann, R. & Leonhardt, H. A guide to super-resolution fluorescence microscopy. *J. Cell Biol.* **190,** 165–175 (2010).
9. Schermelleh, L. *et al.* Super-resolution microscopy demystified. *Nat. Cell Biol.* **21,** 72–84 (2019).
10. van de Linde, S. *et al.* Direct stochastic optical reconstruction microscopy with standard fluorescent probes. *Nat. Protoc.* **6,** 991–1009 (2011).
11. Thompson, R. E., Larson, D. R. & Webb, W. W. Precise Nanometer Localization Analysis for Individual Fluorescent Probes. *Biophys. J.* **82,** 2775–2783 (2002).
12. Quan, T., Zeng, S. & Huang, Z.-L. Localization capability and limitation of electron-multiplying charge-coupled , scientific complementary metal-oxide semiconductor , and charge-coupled devices for superresolution imaging. *J. Biomed. Opt.* **15,** 1–6 (2010).
13. Magidson, V. & Khodjakov, A. Circumventing photodamage in live-cell microscopy. *Methods Cell Biol.* **114,** 545–560 (2013).
14. Epe, B. Genotoxicity of singlet oxygen. *Chem. Biol. Interact.* **80,** 239–260 (1991).
15. Krinsky, N. I. Singlet oxygen in biological systems. *Trends Biochem. Sci.* **2,** 35–38 (1977).
16. Sung, H. J. *et al.* Mitochondrial respiration protects against oxygen-associated DNA damage. *Nat. Commun.* **1,** 1–8 (2010).
17. Bononi, A. *et al.* Mitochondria-Ros Crosstalk in the Control of Cell Death and Aging. *J. Signal Transduct.* **2012,** 1–17 (2011).
18. Nieuwenhuizen, R. P. J. *et al.* Measuring image resolution in optical nanoscopy. *Nat. Methods* **10,** 557–562 (2013).
19. Shroff, H., Galbraith, C. G., Galbraith, J. A. & Betzig, E. Live-cell photoactivated localization microscopy of nanoscale adhesion dynamics. *Nat. Methods* **5,** 417–423 (2008).
20. Wyner, A. D. & Shamai, S. Introduction To 'Communication In The Presence Of Noise'. *Proc. IEEE* **86,** 442–446 (1998).
21. Jones, S. A., Shim, S., He, J. & Zhuang, X. Fast , three-dimensional super-resolution imaging of live cells. *Nat. Methods* **8,** 499- (2011).
22. Fitzgerald, J. E., Lu, J. & Schnitzer, M. J. Estimation Theoretic Measure of Resolution for

Stochastic Localization Microscopy. *Phys. Rev. Lett.* **048102,** 1–5 (2012).

23. Pengo, T., Olivier, N. & Manley, S. Away from resolution , assessing the information content of super- resolution images. *arXiv* 1–22 (2015).
24. Grimm, J. B. *et al.* A general method to improve fluorophores for live-cell and single-molecule microscopy. *Nat. Methods* **12,** 244–250 (2015).
25. Olivier, N., Keller, D., Gönczy, P. & Manley, S. Resolution Doubling in 3D-STORM Imaging through Improved Buffers. *PLoS One* **8,** 1–9 (2013).
26. Dempsey, G. T. *et al.* Photoswitching Mechanism of Cyanine Dyes. *J. Am. Chem. Soc.* **131,** 18192–18193 (2009).
27. Schermelleh, L. *et al.* Subdiffraction Multicolor Imaging of the Nuclear Periphery with 3D Structured Illumination Microscopy. *Microscopy* **320,** 1332–1336 (2010).
28. Bo Huang, Mark Bates, and X. Z. Super resolution fluorescence microscopy. *Natl. Institutes Heal.* **78,** 993–1016 (2009).
29. Huang, B., Wang, W., Bates, M. & Zhuang, X. Three-Dimensional Super-Resolution Imaging by Stochastic Optical Reconstruction Microscopy. *Science (80-.).* 810–814 (2008).
30. Pavani, S. R. P. *et al.* Three-dimensional, single-molecule fluorescence imaging beyond the diffraction limit by using a double-helix point spread function. *Proc. Natl. Acad. Sci.* **106,** 2995–2999 (2009).
31. Shtengel, G. *et al.* Interferometric fluorescent super-resolution microscopy resolves 3D cellular ultrastructure. *Proc. Natl. Acad. Sci. U. S. A.* **106,** 3125–3130 (2009).
32. Juette, M. F. *et al.* Three-dimensional sub – 100 nm resolution fluorescence microscopy of thick samples. *Nat. Methods* **5,** 527–529 (2008).
33. Quirin, S., Pavani, S. R. P. & Piestun, R. Optimal 3D single-molecule localization for superresolution microscopy with aberrations and engineered point spread functions. *Proc. Natl. Acad. Sci.* **109,** 675–679 (2012).
34. Bo Huang, Wenqin Wang, Mark Bates, and X. Z. Three-dimensional Super-resolution Imaging by Stochastic Optical Reconstruction Microscopy. *Science (80-.).* **319,** 810–813 (2009).
35. Backlund, M. *et al.* The double-helix point spread function enables precise and accurate measurement of 3D single-molecule localization and orientation. *Proc. SPIE* **8590,** 85900L–1–85900L–11 (2013).
36. Thompson, M. a, Lew, M. D. & Moerner, W. E. Extending microscopic resolution with single-molecule imaging and active control. *Annu. Rev. Biophys.* **41,** 321–42 (2012).
37. Pavani, S. R. P. & Piestun, R. Three dimensional tracking of fluorescent microparticles using a photon-limited double-helix response system. *Opt. Express* **16,** 22048–22057 (2008).
38. Grover, G., Quirin, S., Fiedler, C. & Piestun, R. Photon efficient double-helix PSF microscopy with application to 3D photo-activation localization imaging. *Biomed. Opt. Express* **2,** 3010 (2011).
39. Daniel Sage*+1, Thanh-An Pham+1, Hazen Babcock2, Tomas Lukes3, Thomas Pengo4, Ramraj Velmurugan5, Alex 4 Herbert6, Anurag Agrawal7, Silvia Colabrese1, 8, Ann Wheeler9, Anna Archetti10, Bernd Rieger11, Raimund Ober5, 5 Guy M. Hagen12, Jean-Baptiste Sibarit, S. H. Super-resolution fight club : A broad assessment of 2D & 3D single-molecule localization microscopy software. *bioRxiv* (2018).
40. Sharonov, A. & Hochstrasser, R. M. Wide-field subdiffraction imaging by accumulated binding of diffusing probes. *Proc. Natl. Acad. Sci.* **103,** 18911–18916 (2006).

41. Jungmann, R. *et al.* Single-molecule kinetics and super-resolution microscopy by fluorescence imaging of transient binding on DNA origami. *Nano Lett.* **10,** 4756–4761 (2010).
42. Schmied, J. J. *et al.* DNA origami nanopillars as standards for three-dimensional superresolution microscopy. *Nano Lett.* **13,** 781–785 (2013).
43. Schmied, J. J. *et al.* DNA origami-based standards for quantitative fluorescence microscopy. *Nat. Protoc.* **9,** 1367–1391 (2014).
44. Schnitzbauer, J., Strauss, M. T., Schlichthaerle, T., Schueder, F. & Jungmann, R. Super-resolution microscopy with DNA-PAINT. *Nat. Protoc.* **12,** 1198–1228 (2017).
45. Kiuchi, T., Higuchi, M., Takamura, A., Maruoka, M. & Watanabe, N. Multitarget super-resolution microscopy with high-density labeling by exchangeable probes. *Nat. Methods* **12,** 743–746 (2015).
46. Rothemund, P. W. K. Folding DNA to create nanoscale shapes and patterns. *Nature* **440,** 297–302 (2006).
47. Douglas, S. M. *et al.* Self-assembly of DNA into nanoscale three-dimensional shapes. *Nature* **459,** 414–418 (2009).
48. Jayasinghe, I. *et al.* True Molecular Scale Visualization of Variable Clustering Properties of Ryanodine Receptors. *Cell Rep.* **22,** 557–567 (2018).
49. Legant, W. R. *et al.* High-density three-dimensional localization microscopy across large volumes. *Nat. Methods* **13,** 359–365 (2016).
50. Jungmann, R. *et al.* Quantitative super-resolution imaging with qPAINT. *Nat. Methods* **13,** 439–442 (2016).
51. Lutz, T. *et al.* Versatile multiplexed super-resolution imaging of nanostructures by Quencher-Exchange-PAINT. *Nano Res.* (2018). doi:10.1007/s12274-018-1971-6
52. Lee, J., Park, S., Kang, W. & Hohng, S. Accelerated super-resolution imaging with FRET-PAINT. *Mol. Brain* **10,** 1–9 (2017).
53. Auer, A., Strauss, M. T., Schlichthaerle, T. & Jungmann, R. Fast, Background-Free DNA-PAINT Imaging Using FRET-Based Probes. *Nano Lett.* **17,** 6428–6434 (2017).
54. Piston, D. W. & Kremers, G. J. Fluorescent protein FRET: the good, the bad and the ugly. *Trends Biochem. Sci.* **32,** 407–414 (2007).
55. Leavesley, S. J. & Rich, T. C. Overcoming limitations of FRET measurements. *Cytom. Part A* **89,** 325–327 (2016).
56. Grandin, H. M., Städler, B., Textor, M. & Vörös, J. Waveguide excitation fluorescence microscopy: A new tool for sensing and imaging the biointerface. *Biosens. Bioelectron.* **21,** 1476–1482 (2006).
57. Agnarsson, B., Ingthorsson, S., Gudjonsson, T. & Leosson, K. Evanescent-wave fluorescence microscopy using symmetric planar waveguides. *Opt. Express* **17,** 5075 (2009).
58. Agnarsson, B., Jonsdottir, A., Arnfinnsdottir, N. & Leosson, K. On-chip modulation of evanescent illumination and live-cell imaging with polymer waveguides. *Opt. Express* **19,** 22929–22935 (2011).
59. Tinguely, J.-C., Helle, Ø. I. & Ahluwalia, B. S. Silicon nitride waveguide platform for fluorescence microscopy of living cells. *Opt. Express* **25,** 27678 (2017).
60. Diekmann, R. *et al.* Chip-based wide field-of-view nanoscopy. *Nat. Photonics* 1–9 (2017). doi:10.1038/nphoton.2017.55
61. Gustafsson, M. G. L. *et al.* Three-dimensional resolution doubling in wide-field fluorescence microscopy by structured illumination. *Biophys. J.* **94,** 4957–4970 (2008).

62. Gustafsson, M. G. L. Nonlinear structured-illumination microscopy: wide-field fluorescence imaging with theoretically unlimited resolution. *Proc. Natl. Acad. Sci. U. S. A.* **102,** 13081–13086 (2005).
63. Rego, E. H. *et al.* PNAS Plus: Nonlinear structured-illumination microscopy with a photoswitchable protein reveals cellular structures at 50-nm resolution. *Proc. Natl. Acad. Sci.* **109,** E135–E143 (2012).
64. Patterson, G., Davidson, M., Manley, S. & Lippincott-schwartz, J. Superresolution Imaging using. *Annu. Rev. Biophys.* 345–67 (2010). doi:10.1146/annurev.physchem.012809.103444
65. Dempsey, G. T., Vaughan, J. C., Chen, K. H., Bates, M. & Zhuang, X. Evaluation of fluorophores for optimal performance in localization-based super-resolution imaging. *Nat. Methods* **8,** 1027–36 (2011).
66. Huang, F. *et al.* Video-rate nanoscopy using sCMOS camera-specific single-molecule localization algorithms. *Nat. Methods* **10,** 653–8 (2013).
67. Burgert, A., Letschert, S., Doose, S. & Sauer, M. Artifacts in single-molecule localization microscopy. *Histochem. Cell Biol.* **144,** 123–131 (2015).
68. Voelkel, R. & Weible, K. J. Laser beam homogenizing: limitations and constraints. in *SPIE* (eds. Duparré, A. & Geyl, R.) 71020J (2008). doi:10.1117/12.799400
69. Voelkel, R. *et al.* Advanced mask aligner lithography: new illumination system. *Opt. Express* **18,** 20968 (2010).
70. Douglass, K. M., Sieben, C., Archetti, A., Lambert, A. & Manley, S. Super-resolution imaging of multiple cells by optimized flat-field epi-illumination. *Nat. Photonics* **10,** 705–708 (2016).
71. Streibl, N., Nolscher, U., Jahns, J. & Walker, S. Array generation with lenslet arrays. *Appl. Opt.* **30,** 2739–2742 (1991).
72. Iukaitis, G. R. A. Č., Ius, E. S. Č., Ys, P. G. E. Č. & Gedvilas, M. Laser Processing by Using Diffractive Optical Laser Beam Shaping Technique. *J. Laser Micro/Nanoengineering* **6,** (2011).
73. Rowlands, C. J., Ströhl, F., Ramirez, P. P. V., Scherer, K. M. & Kaminski, C. F. Flat-Field Super-Resolution Localization Microscopy with a Low-Cost Refractive Beam-Shaping Element. *Sci. Rep.* **8,** 1–8 (2018).
74. Khaw, I. *et al.* Flat-field illumination for quantitative fluorescence imaging. *Opt. Express* **26,** 15276 (2018).
75. Georgiades, P., Allan, V. J., Dickinson, M. & Waigh, T. A. Reduction of coherent artefacts in super-resolution fluorescence localisation microscopy. *J. Microsc.* **264,** 375–383 (2016).
76. Mattheyses, A. L., Shaw, K. & Axelrod, D. Effective Elimination of Laser Interference Fringing in Fluorescence Microscopy by Spinning Azimuthal Incidence Angle. *Microsc. Res. Tech.* **69,** 642–647 (2006).
77. Deschamps, J., Rowald, A. & Ries, J. Efficient homogeneous illumination and optical sectioning for quantitative single-molecule localization microscopy. *Opt. Express* **24,** 28080 (2016).
78. Ichie, K. *et al.* Centrifuge polarizing microscope. I. Rationale, design and instrument performance. *J. Microsc.* **201,** 341–356 (2003).
79. Zhao, Z., Xin, B., Li, L. & Huang, Z.-L. High-power homogeneous illumination for super-resolution localization microscopy with large field-of-view. *Opt. Express* **25,** 13382 (2017).

80. Roorda, R. & Toomre, D. AN OPTICAL SYSTEM FOR ILLUMINATION OF AN EVANESCENTFIELD. *Patent* 050743 A2 (2007).
81. Lei, M. *et al.* Long-Distance Axial Trapping with Focused Annular Laser Beams. **8,** 3–8 (2013).
82. Schreiber, B., Elsayad, K. & Heize, K. G. Axicon-based Bessel beams for flat-field illumination in total internal reflection fluorescence microscopy. *Opt. Lett.* **42,** 3880–3883 (2017).
83. Hu, Y. S., Zimmerley, M., Li, Y., Watters, R. & Cang, H. Single-molecule super-resolution light-sheet microscopy. *ChemPhysChem* **15,** 577–586 (2014).
84. Tokunaga, M., Imamoto, N. & Sakata-sogawa, K. Highly inclined thin illumination enables clear single-molecule imaging in cells. **5,** 159–161 (2008).
85. Schueder, F. *et al.* Multiplexed 3D super-resolution imaging of whole cells using spinning disk confocal microscopy and DNA-PAINT. *Nat. Commun.* **8,** 2090 (2017).
86. Mattheyses, A. L., Simon, S. M. & Rappoport, J. Z. Imaging with total internal reflection fluorescence microscopy for the cell biologist. *J. Cell Sci.* **123,** 3621–3628 (2010).
87. Mattheyses, A. L. & Axelrod, D. Direct measurement of the evanescent field profile produced by objective-based total internal reflection fluorescence. *J. Biomed. Opt.* **11,** 014006 (2006).
88. Yang, Q., Karpikov, A., Toomre, D. & Duncan, J. S. 3-D reconstruction of microtubules from multi-angle total internal reflection fluorescence microscopy using bayesian framework. *IEEE Trans. Image Process.* **20,** 2248–2259 (2011).
89. Kwakwa, K. *et al.* easySTORM : a robust , lower-cost approach to localisation and TIRF microscopy. **957,** 948–957 (2016).
90. Axelrod, D. Total internal reflection fluorescence microscopy in cell biology. *Traffic* **2,** 764–774 (2001).
91. Funatsu, T., Harada, Y., Tokunaga, M., Saito, K. & Yanagida, T. Imaging of single fluorescent molecules and individual ATP turnovers by single myosin molecules in aqueous solution. *Nature* **375,** 555–559 (1995).
92. Ambrose, E. J. A surface contact microscope for the study of cell movements. *Nature* (1956).
93. Fish, K. N. Total Internal Reflection Fluorescence (TIRF) Microscopy. *Curr Protoc Cytom* 1–21 (2009). doi:10.1002/0471142956.cy1218s50.Total
94. Schmitt, K., Oehse, K., Sulz, G. & Hoffmann, C. Evanescent field Sensors Based on Tantalum Pentoxide Waveguides – A Review. *Sensors* **8,** 711–738 (2008).
95. Coucheron, D. A., Helle, Ø. I., Øie, C. I., Dullo, F. T. & Ahluwalia, B. S. Chip-based nanoscopy: towards integration and high-throughput imaging. *Nanoimaging Nanospectroscopy V* 31 (2017). doi:10.1117/12.2273902
96. Rahim, A. *et al.* Expanding the Silicon Photonics Portfolio with Silicon Nitride Photonic Integrated Circuits. *J. Light. Technol.* **35,** 639–649 (2017).
97. Pfeiffer, M. H. P. *et al.* Ultra-smooth silicon nitride waveguides based on the Damascene reflow process: fabrication and loss origins. *Optica* **5,** 884–892 (2018).
98. Wongcharoen, T., Rahman, B. M. A., Rajarajan, M. & Grattan, K. T. V. Spot-size conversion using uniform waveguide sections for efficient laser-fiber coupling. *J. Light. Technol.* **19,** 708–716 (2001).
99. Hauffe, R. *et al.* Methods for passive fiber chip coupling of integrated optical devices. *IEEE Trans. Adv. Packag.* **24,** 450–455 (2001).
100. Almeida, V. R., Panepucci, R. R. & Lipson, M. Nanotaper for compact mode conversion.

Opt. Lett. **28,** 1302 (2003).

101. Ning, T. *et al.* Strong second-harmonic generation in silicon nitride films. *Appl. Phys. Lett.* **100,** (2012).
102. Moss, D. J., Morandotti, R., Gaeta, A. L. & Lipson, M. New CMOS-compatible platforms based on silicon nitride and Hydex for nonlinear optics. *Nat. Photonics* **7,** 597–607 (2013).
103. Johnson, A. R. *et al.* Octave-spanning coherent supercontinuum generation in a silicon nitride waveguide. *Opt. Lett.* **40,** 5117 (2015).
104. Muellner, P. *et al.* CMOS-compatible Si3N4 waveguides for optical biosensing. *Procedia Eng.* **120,** 578–581 (2015).
105. Kordts, A., Pfeiffer, M. H. P., Guo, H., Brasch, V. & Kippenberg, T. J. Higher order mode suppression in high-Q anomalous dispersion SiN microresonators for temporal dissipative Kerr soliton formation. *Opt. Lett.* **41,** 452 (2016).
106. Wang, L. *et al.* Nonlinear silicon nitride waveguides based on PECVD deposition platform. *Opt. Express* **26,** 9645 (2018).
107. Rory, M. P. & Huisken, J. A guide to light-sheet fluorescence microscopy for multiscale imaging. *Nat. Methods* **14,** 360–373 (2017).
108. Wu, Y. *et al.* Inverted selective plane illumination microscopy (i SPIM) enables coupled cell identity lineaging and neurodevelopmental imaging in Caenorhabditis elegans. *Proc. Natl. Acad. Sci.* **108,** 17708–13 (2011).
109. Zanacchi, F. C. *et al.* Live-cell 3D super- resolution imaging in thick biological samples. *Nat. Methods* **8,** 1047–1050 (2011).
110. Gebhardt, J. C. M. *et al.* Single-molecule imaging of transcription factor binding to DNA in live mammalian cells. *Nat. Methods* **10,** 421–426 (2013).
111. Hu, Y. S. *et al.* Light-sheet Bayesian microscopy enables deep- cell super-resolution imaging of heterochromatin in live human embryonic stem cells. *Opt. Nanoscopy* **2,** 1–12 (2013).
112. Verdeyen, J. T., Thomas, J. & Verdeyen, J. T. *Laser Electronics*. (1989).
113. Galbraith, C. G. *et al.* Rapid three-dimensional isotropic imaging of living cells using Bessel beam plane illumination. *Nat. Methods* **8,** 417–423 (2011).
114. Vettenburg, T. *et al.* Light-sheet microscopy using an Airy beam. *Nat. Methods* **11,** (2014).
115. Dean, K. M. & Fiolka, R. Uniform and scalable light-sheets generated by extended focusing. *Opt. Express* **22,** 499–505 (2014).
116. Olarte, O. E., Andilla, J., Gualda, E. J. & Loza-Alvarez, P. Light-sheet microscopy : a tutorial. *Adv. Opt. Photonics* **10,** 111–179 (2018).
117. Sage, D. *et al.* Quantitative evaluation of software packages for single-molecule localization microscopy. *Nat. Methods* **12,** 1–12 (2015).
118. Markham, J. Dimensional Fluorescence Microscopy. *J. Opt. Soc. Am.* **18,** 1062–1071 (2001).
119. Verveer, P. J. & Jovin, T. M. Efficient superresolution restoration algorithms using maximum a posteriori estimations with application to fluorescence microscopy. *J. Opt. Soc. Am.* **14,** 1696 (2008).
120. Kay, S. M. *Fundamentals of Statistical Signal Processing : Estimation Theory*. (Prentice Hall PTR, 1993).
121. Mortensen, K. I., Churchman, L. S., Spudich, J. a & Flyvbjerg, H. Optimized localization analysis for single-molecule tracking and super-resolution microscopy. *Nat. Methods* **7,**

377–381 (2010).
122. Ober, R. J., Ram, S. & Ward, E. S. Localization Accuracy in Single-Molecule Microscopy. *Biophys. J.* **86,** 1185–1200 (2004).
123. Robbins, M. S. & Hadwen, B. J. The noise performance of electron multiplying charge-coupled devices. *IEEE Trans. Electron Devices* **50,** 1227–1232 (2003).
124. Smith, C. S., Joseph, N., Rieger, B. & Lidke, K. A. Fast, single-molecule localization that achieves theoretically minimum uncertainty. *Nat. Methods* **7,** 373–375 (2010).
125. Lew, M. D., von Diezmann, A. R. S. & Moerner, W. E. Easy-DHPSF open-source software for three-dimensional localization of single molecules with precision beyond the optical diffraction limit. *Protoc. Exch.* **2013,** 1–18 (2013).
126. Li, Y. *et al.* Real-time 3D single-molecule localization using experimental point spread functions. *Nat. Methods* **15,** 367–369 (2018).
127. Babcock, H. P. & Zhuang, X. Analyzing Single Molecule Localization Microscopy Data Using Cubic Splines. *Sci. Rep.* **7,** 552 (2017).
128. Aristov, A., Lelandais, B., Rensen, E. & Zimmer, C. ZOLA-3D allows flexible 3D localization microscopy over an adjustable axial range. *Nat. Commun.* **9,** 2409 (2018).
129. Zelger, P. *et al.* Three-dimensional localization microscopy using deep learning. *Opt. Express* **26,** 33166 (2018).
130. Zhang, P. *et al.* Analyzing complex single-molecule emission patterns with deep learning. *Nat. Methods* **15,** 913–916 (2018).
131. Babcock, H. P. & Zhuang, X. Analyzing Single Molecule Localization Microscopy Data Using Cubic Splines. (2016). doi:10.1101/083402
132. Annibale, P., Vanni, S., Scarselli, M., Rothlisberger, U. & Radenovic, A. Quantitative Photo Activated Localization Microscopy: Unraveling the effects of photoblinking. *PLoS One* **6,** (2011).
133. Durisic, N., Laparra-cuervo, L., Sandoval-álvarez, Á., Borbely, J. S. & Lakadamyali, M. Single-molecule evaluation of fluorescent protein photoactivation efficiency using an in vivo nanotemplate. *Nat. Methods* **11,** 156–164 (2014).
134. Basden, G., Haniff, C. A. & Mackay, C. D. Photon counting strategies with low light level CCDs. *arXiv* **7,** 1–7 (2003).
135. Chao, J. *et al.* Localization accuracy in single molecule microscopy using electron-multiplying charge-coupled device cameras. *Proc. SPIE* (2012). doi:10.1117/12.908951
136. Chao, J., Ward, E. S. & Ober, R. J. Fisher information theory for parameter estimation in single molecule microscopy : tutorial. *J. Opt. Soc. Am.* **33,** 36–57 (2016).
137. Lambert, A. *et al.* Constriction Rate Modulation Can Drive Cell Size Control and Homeostasis in C.crescentus. *iScience* 180–189 (2018). doi:10.1016/j.isci
138. Donachie, W. D. & Begg, K. J. Cell length, nucleoid separation, and cell division of rod-shaped and spherical cells of Escherichia coli. *J. Bacteriol.* **171,** 4633–4639 (1989).
139. Schulz, H. N. & Barker, B. BIG BACTERIA. *Annu. Rev. Microbiol.* (2001).
140. Silhavy, T. J., Kahne, D. & Walker, S. The Bacterial Cell Envelope. *Cold Spring Harb. Prospect. Biol.* 1–16 (2010).
141. Chang, F. & Huang, K. C. How and why cells grow as rods. *BMC Biol.* **12,** 54 (2014).
142. Zaritsky, A. Cell-shape homeostasis in Escherichia coli is driven by growth, division, and nucleoid complexity. *Biophys. J.* **109,** 178–81 (2015).
143. Grover, N. B. & Woldringh, C. L. Dimensional regulation of cell-cycle events in Escherichia coli during steady-state growth. *Microbiology* **147,** 171–181 (2001).
144. Höltje, J. V. Growth of the stress-bearing and shape-maintaining murein sacculus of

Escherichia coli. *Microbiol. Mol. Biol. Rev.* **62,** 181–203 (1998).

145. Monteiro, J. M. *et al.* Cell shape dynamics during the staphylococcal cell cycle. *Nat. Commun.* In press (2015). doi:10.1038/ncomms9055
146. den Blaauwen, T., Hamoen, L. W. & Levin, P. A. The divisome at 25: the road ahead. *Curr. Opin. Microbiol.* **36,** 85–94 (2017).
147. Reshes, G., Vanounou, S., Fishov, I. & Feingold, M. Timing the start of division in E. coli: a single-cell study. *Phys. Biol.* **5,** 046001 (2008).
148. Laub, M. T., McAdams, H. H., Feldblyum, T., Fraser, C. M. & Shapiro, L. Global Analysis of the Genetic Network Controlling a Bacterial Cell Cycle. *Science (80-.).* **290,** 2144–2148 (2000).
149. Schrader, J. M. & Shapiro, L. Synchronization of Caulobacter crescentus for investigation of the bacterial cell cycle. *J. Vis. Exp.* e52633 (2015). doi:10.3791/52633
150. Gustafsson, M. G. L. Surpassing the lateral resolution limit by a factor of two using structured illumination microscopy. *J. Microsc.* **198,** 82–87 (2000).
151. Szeto, T. H., Rowland, S. L., Habrukowich, C. L. & King, G. F. The MinD membrane targeting sequence is a transplantable lipid-binding helix. *J. Biol. Chem.* **278,** 40050–40056 (2003).
152. Schaechter, M., Williamson, J. P., Hood, J. R. & Koch, A. L. Growth, Cell and Nuclear Divisions in some Bacteria. *J. Gen. Microbiol.* **29,** 421–434 (2009).
153. Bryan, A. K. *et al.* Using buoyant mass to measure the growth of single cells. *Nat. Methods* **7,** 387–390 (2010).
154. Wientjes, F. B., Woldringh, C. L. & Nanninga, N. Amount of Peptidoglycan in Cell Walls of Gram-Negative Bacteria sacculu . Frceichal dtoerminoatio do. *J. Bacteriol.* **173,** 7684–7691 (1991).
155. Jones, L. J. F., Carballido-Lopez, R. & Errington, J. Control of Cell Shape in Bacteria: Helical, Actin-like Filaments in Bacillus subtilis. *Cell Press* **104,** 913–922 (2001).
156. Mercer, eri L. & Weiss, D. S. The Escherichia coli Cell Division Protein FtsW Is Required To Recruit Its Cognate Transpeptidase, FtsI (PBP3), to the Division Site. *J. Bacteriol.* **184,** 904–912 (2002).
157. VanWagner, L. B. *et al.* Nonalcoholic fatty liver disease and measures of early brain health in middle-aged adults: The CARDIA study. *Obesity* **25,** 642–651 (2017).
158. Modell, J. W., Kambara, T. K., Perchuk, B. S. & Laub, M. T. A DNA Damage-Induced, SOS-Independent Checkpoint Regulates Cell Division in Caulobacter crescentus. *PLoS Biol.* **12,** (2014).
159. Reshes, G., Vanounou, S., Fishov, I. & Feingold, M. Cell shape dynamics in Escherichia coli. *Biophys. J.* **94,** 251–64 (2008).
160. Schaechter, M., MaalOe, O. & Kjeldgaard, N. O. Dependency on Medium and Temperature of Cell Size and Chemical Composition during Balanced Growth of Salmonella typhimurium. *J. Gen. Microbiol.* **19,** 592–606 (2009).
161. Perlman, Z. E. *et al.* Multidimensional drug profiling by automated microscopy. *Science (80-.).* **306,** 1194–1198 (2004).
162. Sliusarenko, O., Heinritz, J., Emonet, T. & Jacobs-Wagner, C. High-throughput, subpixel precision analysis of bacterial morphogenesis and intracellular spatio-temporal dynamics. *Mol. Microbiol.* **80,** 612–627 (2011).
163. Holden, S. J. *et al.* High throughput 3D super-resolution microscopy reveals Caulobacter crescentus in vivo Z-ring organization. *Proc. Natl. Acad. Sci.* **111,** 4566–4571 (2014).
164. Almada, P., Culley, S. & Henriques, R. PALM and STORM: Into large fields and high-

throughput microscopy with sCMOS detectors. *Methods* **88,** 109–121 (2015).
165. Sieben, C., Banterle, N., Douglass, K. M., Gönczy, P. & Manley, S. Multicolor single-particle reconstruction of protein complexes. *Nat. Methods* **15,** 777–780 (2018).
166. Saurabh, S., Maji, S. & Bruchez, M. P. Evaluation of sCMOS cameras for detection and localization of single Cy5 molecules. *Opt. Express* **20,** 7338–49 (2012).
167. Bigas, M., Cabruja, E., Forest, J. & Salvi, J. Review of CMOS image sensors. *Microelectronics* **37,** 433–451 (2006).
168. Yadidpecht, O., Mansoorian, B., Fossum, E. R. & Pain, B. Optimization of Noise and Responsivity in CMOS Active Pixel Sensors for Detection of Ultra Low Light Levels. *Proc. SPIE* **3019,** 125–136 (1997).
169. Huang, Z.-L. *et al.* Localization-based super-resolution microscopy with an sCMOS camera. *Opt. Express* **19,** 19156–68 (2011).
170. Sliusarenko, O., Heinritz, J., Emonet, T. & Jacobs-Wagner, C. High-throughput, subpixel precision analysis of bacterial morphogenesis and intracellular spatio-temporal dynamics. *Mol. Microbiol.* **80,** 612–627 (2011).
171. Otsu, N. A Threshold Selection Method from Gray-Level Histograms. *IEEE transations Syst. man Cybern.* **SMC-9,** 62–66 (1979).
172. Brunelli, R. *Template Matching Techniques in Computer Vision*. (2008).
173. Huang, F. *et al.* Video-rate nanoscopy using sCMOS camera-specific single-molecule localization algorithms. *Nat. Methods* **10,** 653–8 (2013).
174. Douglass, K. M., Sieben, C., Archetti, A., Lambert, A. & Manley, S. Super-resolution imaging of multiple cells by optimized flat-field epi-illumination. *Nat. Photonics* **10,** 705–708 (2016).
175. Joubert, J., Sabharwal, Y. & Sharma, D. Digital Camera Technologies for Scientific Bio-Imaging . Part 3 : Noise and Signal-to-NoiseRatios. 1–4 (2011).
176. Sukumar, V., Tanner, J., Sarwari, A. & Hess, H. L. Algorithms for Masking Pixel Defects at Low Exposure Conditions for CMOS Image Sensors. *Engineering* **02,** 220–227 (2010).
177. Long, F., Zeng, S. & Huang, Z. Localization-based super-resolution microscopy with an sCMOS camera Part II : Experimental methodology for comparing sCMOS with EMCCD cameras. *Opt. Express* **20,** 17741–17759 (2012).
178. Ovesny, M., Krizek, P., Borkovec, J., Svindrych, Z. & Hagen, G. M. ThunderSTORM: A comprehensive ImageJ plug-in for PALM and STORM data analysis and super-resolution imaging. *Bioinformatics* **30,** 2389–2390 (2014).
179. Wolter, S. *et al.* rapidSTORM: accurate, fast open-source software for localization microscopy. *Nat. Methods* **9,** 1040–1 (2012).
180. Yap, K. P. *et al.* Fabrication of lithographically defined optical coupling facets for silicon-on-insulator waveguides by inductively coupled plasma etching. *J. Vac. Sci. Technol. A Vacuum, Surfaces, Film.* **24,** 812–816 (2006).
181. Archetti, A. *et al.* Waveguide-PAINT offers an open platform for large field-of-view super-resolution imaging. *Nat. Commun.* **10,** 1–9 (2019).
182. Wang, L. *et al.* Highly confined surface imaging by solid immersion total internal reflection fluorescence microscopy. *Opt. Express* **20,** 3311 (2012).
183. Stabley, D. R., Oh, T., Simon, S. M., Mattheyses, A. L. & Salaita, K. Real-time fluorescence imaging with 20 nm axial resolution. *Nat. Commun.* **6,** 1–7 (2015).
184. Schnitzbauer, J., Strauss, M. T., Schlichthaerle, T., Schueder, F. & Jungmann, R. Super-resolution microscopy with DNA-PAINT- Supp. *Nat. Protoc.* **12,** 1198–1228 (2017).
185. Edelstein, A., Amodaj, N., Hoover, K., Vale, R. & Stuurman, N. Computer control of

microscopes using manager. *Curr. Protoc. Mol. Biol.* 1–17 (2010). doi:10.1002/0471142727.mb1420s92

186. Ovesny, M., Krizek, P., Borkovec, J., Svindrych, Z. & Hagen, G. M. ThunderSTORM: a comprehensive ImageJ plug-in for PALM and STORM data analysis and super-resolution imaging. *Bioinformatics* **30,** 2389–2390 (2014).
187. Wang, Y. *et al.* Localization events-based sample drift correction for localization microscopy with redundant cross-correlation algorithm. *Opt. Express* **22,** 15982–15991 (2014).
188. Paintdakhi, A. *et al.* Oufti: An integrated software package for high-accuracy, high-throughput quantitative microscopy analysis. *Mol. Microbiol.* **99,** 767–777 (2016).
189. Kafri, R. *et al.* Dynamics extracted from fixed cells reveal feedback linking cell growth to cell cycle. *Nature* **494,** 480–483 (2013).
190. Gut, G., Tadmor, M. D., Pe’er, D., Pelkmans, L. & Liberali, P. Trajectories of cell-cycle progression from fixed cell populations. *Nat. Methods* **12,** 951–954 (2015).
191. Sun, W., Marehuk, K., Wang, G. & Fang, N. Autocalibrated scanning-angle prism-type total internal reflection fluorescence microscopy for nanometer-precision axial position determination. *Anal. Chem.* **82,** 2441–2447 (2010).
192. Rohrbach, A. Observing secretory granules with a multiangle evanescent wave microscope. *Biophys. J.* **78,** 2641–2654 (2000).
193. Fu, Y. *et al.* Axial superresolution via multiangle TIRF microscopy with sequential imaging and photobleaching. *Proc. Natl. Acad. Sci.* **113,** 4368–4373 (2016).
194. Odermatt, P. D. *et al.* High-Resolution Correlative Microscopy: Bridging the Gap between Single Molecule Localization Microscopy and Atomic Force Microscopy. *Nano Lett.* **15,** 4896–4904 (2015).
195. Kopek, B. G., Shtengel, G., Grimm, J. B., Clayton, D. A. & Hess, H. F. Correlative Photoactivated Localization and Scanning Electron Microscopy. *PLoS One* **8,** (2013).

Curriculum Vitae

Personal information

First Name/Surname	Anna Archetti
e-mail	anna.archetti@gmail.com
Nationality	Italian

Work Experience

Feb. 2015 - Present	**PhD**, Doctoral Program in Photonics
Principal subjects/skills covered	• Fluorescence and SEM microscopy • Micro-nano fabrication of HIC waveguides • Design and commissioning of a waveguide-based superresolution fluorescence microscope • Waveguide mode simulation. 3D-single molecule dataset simulation • Development of algorithms for processing of high throughput biological microscopy images; realization of a full pipeline for 3D image reconstruction from single molecule images • Single molecule data analysis. Cell shape parameters analysis • DNA-PAINT experiments and imaging
Employer and Supervisor	EPFL (École polytechnique fédérale de Lausanne) – Institute of Physics, LEB (Laboratory of Experimental Biophysics) of Prof. Suliana Manley
Feb. 2016 - Feb. 2017	**Committee Member** - SMLM Challenge 2016 http://bigwww.epfl.ch/smlm/challenge2016/index.html
Principal subjects	Evaluation of existing 3D localization algorithms and generation of robust simulated datasets
Aug. 2014 - Jan. 2015	**Intership**
Principal subjects	CMOS camera characterization and CMOS specific reconstruction algorithm development for single molecule superresolution microscopy (STORM).
Employer	EPFL (École polytechnique fédérale de Lausanne) – Institute of Physics, LEB (Laboratory of Experimental Biophysics) of Prof. Suliana Manley
May 2014 – Jun. 2014	**High School Teacher**
Principal subjects	Teacher of mathematics
Employer	Istituto Tecnico per il Turismo "Francesco Da Collo", Conegliano (TV),IT

Feb. 2014 – Mar. 2014	**High School Teacher**
Principal subjects	Teacher of mathematics and Information Technology
Employer	Istituto Einaudi/Cavalli, Vittorio Veneto (TV), Italy

Apr. 2013 – Dec. 2013	**Internship**
Principal subjects	Characterization of SPAD arrays for time-resolved fluorescence measurements
Employer	FBK (Fondazione Bruno Kessler), Trento, Italy

Oct. 2011 – Dec. 2013	**Work to support my studies**
Principal subjects	Restaurant reception and hall manager, customer reception, waitress
Employer	Ristorante Pedavena – Trento, Italy

Education

Master degree in Physics	2011 – 2013
Thesis Title	SPAD based sensor for FLIM and spectroscopy of human skin
Principal subjects/skills covered	• Development of an optical spectrograph • MATLAB and C++ programming • TCSPC (Time-Correlated Single-Photon Counting) measurements
Relevant Courses	Bioimaging, Optoelectronics, Nuclear Physics applied to Biomedicine, Electronics (VHDL - FPGA), Molecular and cellular Biophysics
Organisation providing education	Università degli Studi di Trento, Trento, Italy in collaboration with FBK (Fondazione Bruno Kessler), Trento, Italy
Thesis supervisor and Co-Supervisor	Albrecht Haase and Lucio Panchieri (UniTrento)

Bachelor degree in Physics	2005 – 2010
Thesis Title	Neutron flux effects on SiPM detectors
Principal subjects	SiPM characterization
Organisation providing education	Università degli Studi di Padova, Padova, Italy
Supervisor and Co-Supervisor	Roberto Stroili and Flavio Dal Corso (UniPD)

Skills

Optical systems	• To build a super-resolution fluorescence microscope (STORM, DNA-PAINT microscopes).

- To realize mechanical holder compatible with imaging system.
- To perform imaging experiment with STORM, DNA-PAINT and SEM microscope.
- To analyze raw SMLM images and to reconstruct high-quality super-resolved images.

Device Characterization	SiPM, SPAD array, CMOS camera, Waveguide
Micro-Nano fabrication	Photolitography, e-beam lithography, LPCVD deposition, RIE etching
Programming languages	C++, VHDL, Matlab,
Software	Mathematica, SketchUp, KLayout, Inkscape, ImageJ, Micro-Manager
Teaching	High School Teaching and Undergraduate Student Tutoring

Interests

Classical Musics	I studied transverse flute and piano getting a licence in theory and solfeggio, a licence in music history and the low degree in piano at the State conservatories of music.
Sport	Basket, Running, Road Biking
Social no-profit organization	Scout

Publications

Douglass, K. M., Sieben, C., Archetti, A., Lambert, A. & Manley, S. Super-resolution imaging of multiple cells by optimized flat-field epi-illumination. *Nat. Photonics* **10**, 705–708 (2016).

Lambert, A., Vanhecke, A., Archetti, A., Holden, S., Schaber, F., Pincus, Z., Laub, M.T., Goley, E. and Manley, S. Constriction Rate Modulation Can Drive Cell Size Control and Homeostasis in C.crescentus. *IScience* **4**, 180–189 (2018).

Sage, D. *et al.* Super-resolution fight club: A broad assessment of 2D & 3D single-molecule localization microscopy software. *Nat. Methods* (2019)

Archetti, A., Glushkov E., Sieben C., Stroganov A., Radenovic A., and Manley S. An open platform for large field-of-view waveguide-PAINT. *Nat. Comms.* 1-9 (2019)

Prizes, selections and oral presentations

Selected for the “Modeling Cellular Processes in Space and Time” EMBL course
Teaching award for outstanding tutorial assistant, EPFL, 2017
Short presentation – EMBL Modelling cellular processes in space and time course
Flash presentation in 180'' - Photonics Day December 2017 and 2018
Oral presentation (20') – Focus on Microscopy (FOM) 2019

Ce document a été imprimé au Centre d’impression EPFL,
imprimerie climatiquement neutre, certifiée myClimate.